UNIVERSITÉ DE SHERBROOKE
Faculté de génie
Département de génie mécanique

APPROCHE NUMÉRIQUE DU CONTRÔLE DU BRUIT TONAL DES VENTILATEURS PAR OBSTRUCTION DE L'ÉCOULEMENT

NUMERICAL INVESTIGATION OF TONAL NOISE CONTROL OF LOW-SPEED FANS WITH FLOW OBSTRUCTION

Thèse de doctorat
Specialité : génie mécanique

Stéphan MAGNE

Jury: Stéphane AUBERT
Alain BERRY (co-directeur)
Thomas CAROLUS
Jessica GULLBRAND
Thomas MAS
Patrice MASSON (rapporteur)
Stéphane MOREAU (directeur)
Michel ROGER

Sherbrooke (Québec) Canada Automne 2015

RÉSUMÉ

La réduction du bruit tonal des ventilateurs basse vitesse est un défi très important pour l'industrie. Lorsqu'il émerge du bruit large bande, ce rayonnement est la source de gênes auprès de la population, que ce soit pour de petits ventilateurs d'ordinateurs ou de gros ventilateur miniers. Afin de contrôler le bruit tonal, de nombreuses techniques ont été développées au fil de ces dernières décennies. Une méthode alliant simplicité et efficacité se démarque néanmoins : le contrôle par obstruction de l'écoulement. Malgré les études menées jusqu'alors, les mécanismes aéroacoustiques de réduction du bruit associés à cette méthode restent mal compris. Pour répondre à cette problématique, ce projet de Doctorat s'intéresse à l'étude de l'intéraction entre l'obstruction et le ventilateur au moyen de simulations aéro-acoustiques. De plus, une méthodologie numérique de design de l'obstruction est proposée afin de réduire les coûts associés aux multiples test expérimentaux.

Mots-clés : Aéro-acoustique, ventilateur, bruit tonal, contrôle, obstruction, simulation numérique.

ABSTRACT

TONAL noise radiated by low-speed fans is a prime challenge for many industries. When this component emerges from the broadband noise, the acoustic radiation is particularly harsh for the human ear, whether it comes from a small computer cooling fan or from a large mine ventilation fan. Several methods have been developed over the last decades to control tonal noise. Nevertheless, one simple and efficient technique stands out: the adaptive passive control with flow obstruction. Despite all the research conducted on this method, the aeroacoustic mechanisms responsible for the noise reduction are not fully understood. Therefore, the present thesis aims at investing the obstruction-fan interaction using aeroacoustic simulations. Moreover, a numerical design methodology is proposed to reduce the cost induced by extensive experimental tests.

Keywords: Aeroacoustics, fan, tonal noise, control, obstruction, numerical simulation.

ACKNOWLEDGEMENTS

FIRSTLY, I would like to thank my supervisors, Stéphane MOREAU and Alain BERRY, for welcoming me at the Université de Sherbrooke. I am forever grateful for their support and guidance throughout my Ph.D. project!

My sincere thanks go to my thesis committee: Stéphane AUBERT, Thomas CAROLUS, Jessica GULLBRAND, Thomas MAS, Patrice MASSON, Michel ROGER, for their insightful comments and encouragement.

I express my thanks to Alstom Transport and Intel Corporation for their funding and the stimulating discussions on industrial applications of my research. I sincerely thank Manuel HENNER and Bruno DEMORY from Valeo for their valued help with the experimental and numerical setups.

I am also very grateful to all the persons who helped me with the numerical codes: Lionel GAMET and Pascal FERRAND from Fluorem, as well as Frank PÉROT and Dave FREED from Exa Corporation.

I warmly thank everybody from the aeroacoustic group: Marlène, Hélène, Jérôme, Pablo, Arnaud, Dominic, Laurent, Aurélien, Thomas G., Michaël, Yann. Your friendship and helpful discussions played a large part in the success of this thesis.

I am very grateful to Thomas P., Olivier D., Nicolas, Olivier R., Anthony, and Philippe-Aubert. Your combined interests in acoustics and bubbly drinks have always triggered some passionate debates.

I would also like to thank the student associations – G3 and REMDUS – for giving me the opportunity to help the graduate student community.

Last but not least, my deepest thanks go to my family; my parents for their support, and to my wife, Viktoria, for going through this adventure with love, patience and understanding, but also for her fantastic ability to keep me motivated during the toughest moments.

TABLE OF CONTENTS

LIST OF FIGURES

LIST OF TABLES

CHAPTER 1

INTRODUCTION

1.1 Context

Noise reduction is a very hot topic nowadays. For instance, the European Union adopted in 2002 a directive to assess and reduce environmental noise, which led to several research programs involving public laboratories, but also private companies [European Parliament and Council, 2002]. One of these programs stated that 3 % of myocardial infarctions in Germany are due to road traffic noise [European Union, 2008]. Whether it is to improve customer comfort, to meet standards, or to be used as a selling point, a lot of companies invest in research and development programs to improve noise control methods. Several business sectors across the globe follow the trend, to reduce fan noise in particular.

Fans are everywhere in everyday life: in cars, metros, trains, planes, in computers and electronic components, and in building ventilation units. Although the use of a fan may be avoided in some cases, such as in electronic components, fan noise is often found to be the dominant noise in numerous applications.

The acoustic radiation from low-speed fans can be divided into two contributions: tonal noise and broadband noise. Broadband noise is associated with the turbulent flow field, which creates an acoustic radiation distributed throughout the whole frequency spectrum. Tonal noise is generated by the periodic components of the blade load and is characterized by high peaks in the frequency spectrum. Both types of noise contribute significantly to the overall acoustic radiation, but from a psychoacoustic point of view, tonal noise is often perceived as more annoying. Moreover, in low-subsonic rotating machines, tonal noise has a dominant contribution in the lower end of the spectrum. As a result, the efficiency of control methods is reduced and noise propagates longer distances.

Tonal noise reduction methods can be divided into three categories. The first one, called passive control, adds material or modify permanently the geometry to act on the sound generation or propagation. The noise reduction associated with this method is often limited, particularly at low frequencies as in the case of low-speed fans. Active control constitutes the second category. Developed to mitigate noise in configurations where passive control is inefficient, this technique is based on the superposition of two acoustic waves – one from the

noisy system and another one of the same amplitude but opposite phase. Although active control can yield large noise reductions, this approach is complex to implement, expensive, and requires an additional energy supply. For these reasons, active control is rarely used by low-speed fan manufacturers. Adaptive passive control, the last category, modifies the fan installation in order to create a second source which cancels the primary noise. Among the few techniques which fall in this category, the use of flow obstruction appears to be a cheap yet efficient way to reduce tonal noise. However, the aeroacoustic mechanisms responsible for the noise reduction are not well understood. Additionally, the iterative optimization process requires physical prototypes and extensive acoustic measurements, which is expensive and time-consuming for fan manufacturers.

1.2 Research project and objectives

In the context presented above, Computational AeroAcoustics (CAA) appears to be an excellent tool to further investigate the obstruction-fan interaction and identify the acoustic sources. Unlike measurements, numerical simulations are able to highlight the modifications of the flow induced by the obstruction and analyze – in the frequency domain – the pressure fluctuations on the solid surfaces. Furthermore, the development of a numerical optimization of the obstruction shape and position could be very profitable in an industrial context.

This research is part of an I2I grant funded by the Natural Sciences and Engineering Research Council of Canada (NSERC), Alstom Transport SA, and Intel Corporation. While other parts of the grant were dedicated to the development of existing Alstom products – on which post-doctoral fellows worked –, the present thesis focuses on a more fundamental and deeper understanding of the tonal noise reduction using flow obstruction and evaluates the possibility to numerically design an optimal obstruction prior to experiments.

The objectives of the present study are:

- Select the numerical methods and solvers to perform aeroacoustic computations;
- Characterize the acoustic signature of the chosen fan in order to evaluate its controllability with flow obstruction;
- Perform a complete aeroacoustic simulation of the obstruction-fan interaction;
- Determine the noise radiated by the obstruction itself;
- Highlight the aeroacoustic mechanisms responsible for the noise reduction;
- Develop an industrially-applicable numerical methodology to optimize the obstruction shape and position;
- Experimentally validate the results.

The "H380EC01" automotive cooling fan designed by Valeo is chosen for the present study. Since this axial fan has been a test case for almost 15 years, a lot of experimental and numerical data are found in the literature. Moreover, the fan dimensions fall in between the small computer cooling fans and the large ventilation units.

1.3 Thesis structure

Chapter 2 presents the state of the art. The aeroacoustic mechanisms responsible for low-speed fan noise are listed, and the different sources are illustrated on a typical axial cooling fan. An exhaustive literature review of tonal reduction methods are categorized in three sections: passive control, active control, and adaptive passive control.

In Chapter 3, computational aeroacoustic methods are introduced. The aerodynamic simulation methods and acoustic propagation analogies are presented in the context of tonal fan noise predictions. The chosen methods are then validated on the sound radiation from the flow past a cylinder.

The acoustic signature of an isolated automotive rotor in a uniform inlet flow is characterized in Chapter 4. Several operating points are studied using a hybrid aeroacoustic method based on unsteady RANS simulations coupled with an acoustic analogy. Results are compared with experimental and numerical investigations available in the literature. This chapter is in most part based on an article accepted for publication in the Journal of the Acoustical Society of America and entitled *Subharmonic tonal noise from backflow vortices radiated by a low-speed ring fan in uniform inlet flow* [Magne *et al.*, 2015].

Since the noise radiated by the rotor alone cannot be controlled with static obstructions, Chapter 5 introduces a rotor-stator configuration designed to enhance the tonal noise. Numerical predictions are obtained using unsteady RANS and Lattice-Boltzmann methods. The performance and precision of the solvers are evaluated, and the acoustic results are compared with microphone measurements acquired in an anechoic room.

Chapter 6 presents the results with flow obstruction. A design methodology is first developed to get an optimal obstruction design from a minimal number of numerical simulations. Complete aeroacoustic simulations of the obstruction-fan interaction are then performed to investigate the aeroacoustics mechanisms and applied the methodology. The same methodology is also applied to experiments in order to validate the numerical results.

Finally, conclusions and perspectives are presented in Chapter 7.

CHAPTER 2

STATE OF THE ART

Low-speed fans are very widely used in modern societies. From computer cooling systems to building ventilation units, the dimension of the fans varies greatly but the aeroacoustic mechanisms responsible for the noise remain the same. In order to better understand these phenomena and the way to control them, this chapter is divided into two sections. The first one describes the acoustic sources radiated by low-speed fans, and the second one presents the methods to control the predominant source.

2.1 Low-speed fan noise

A fan is a system transferring mechanic energy to a fluid. This energy creates a pressure rise across the fan which results in an air flow. Because of their design, the centrifugal fans are mostly dedicated to create a large pressure rise, whereas the axial fans create a larger flow rate and a smaller pressure rise [Dixon and Hall, 2010, Chap. 2].

To better understand the sound generation mechanisms, it is important to introduce the three types of acoustic sources which are radiated [Caro and Moreau, 2000; Neise, 1992; Wright, 1938]:

Monopolar component This radiation, also called thickness noise, is due to the fluid displacement in the vicinity of the fan which is created by the blade rotation. The acoustic source resulting from this mechanism has the characteristics of a monopole – a point source which radiates sound equally in all the directions.

Dipolar component The unsteady forces acting on a surface create wall-pressure fluctuations. The resulting acoustic sources are similar to a dipole – a point source equivalent to two monopoles of equal source strength, but opposite phase, and separated by a small distance.

Quadrupolar component In a turbulent flow, the collision and distortion of turbulent eddies generate volumic acoustic sources which are associated with quadrupoles – point sources equivalent to two dipoles of equal source strength, but opposite phase, and separated by a small distance.

The quadrupolar component becomes efficient when the tip blade velocity reaches a Mach number $M = 0.8$ [Morfey, 1971]. Additionally, for low-speed applications, the pressure

fluctuations due to the fluid displacement have an azimuthal phase velocity which is negligible in comparison with the speed of sound c_0 [Neise, 1992]. Therefore, the dipolar sources dominate the noise radiated by low-speed fans.

Several aeroacoustic phenomena are responsible for the dipolar sources. Depending on their frequency contribution to the acoustic spectrum, these phenomena fall into two categories: broadband noise and tonal noise. The numbers in the following two sections refer to the source locations illustrated for an automotive axial fan in Figure 2.1.

2.1.1 Broadband noise

Broadband noise has a contribution over a large frequency range. It is induced by chaotic turbulent structures impacting the fan solid surfaces. It is divided in several contributions depending on which aeroacoustic mechanism creates the noise [Carolus *et al.*, 2007]:

Leading edge The noise created by turbulent structures impacting a sharp solid edge is associated with the leading edge noise. This interaction may happen at the inlet of a heat exchanger (1), at the rotor leading edge (2), or at the stator leading edge (3).

Trailing edge In a turbulent regime, the boundary layer developed on an airfoil/plate interacts with the trailing edge and radiates a broadband noise. This may be observed at the outlet of a heat exchanger (5), at the rotor trailing edge (6), or at the stator trailing edge (7).

Tip clearance recirculation The pressure rise induced by the fan generates a backflow in the tip clearance which impacts the blades and creates an additional source of broadband noise (4).

2.1.2 Tonal noise

Tonal noise is characterized by sharp tones in the frequency spectrum. This radiation is the consequence of periodic wall-pressure fluctuations on the fan surfaces. It is mainly due to four aeroacoustic mechanisms:

Rotor-stator interaction The rotor wake creates a periodic variation of the downstream velocity profile which induces tonal noise sources on the stator vanes (3).

Potential effect A solid surface immersed in a flow creates a pressure rise in the upstream direction which is called potential effect [Caro and Moreau, 2000]. For an axial fan, the potential effect attached to the rotor movement creates periodic

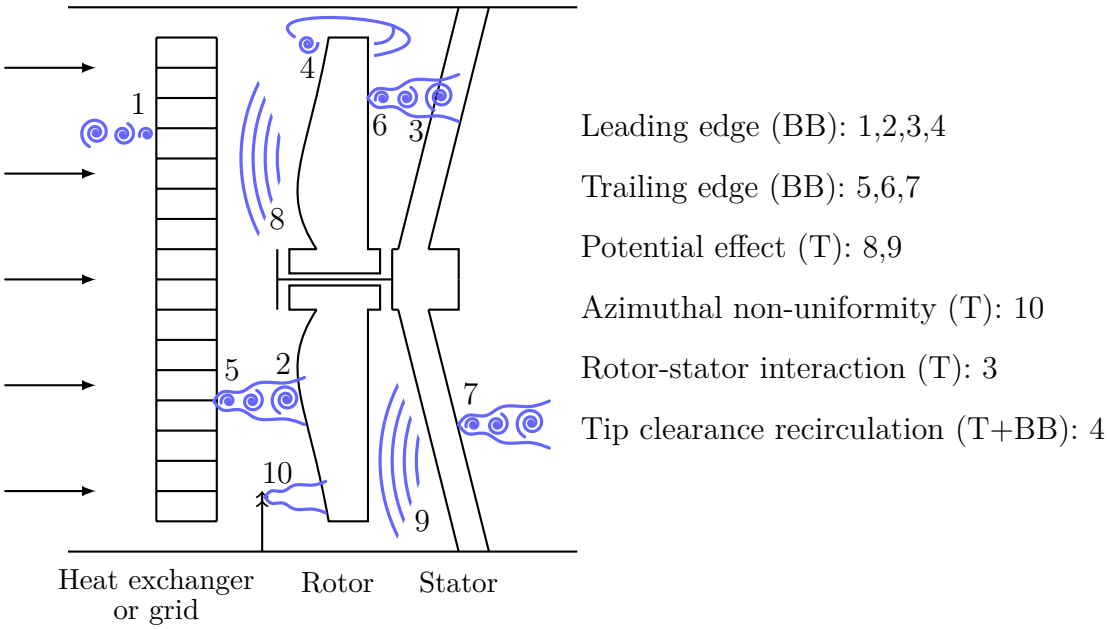

Figure 2.1 Noise sources localization on a typical automotive axial fan (T = tonal noise, BB = broadband noise).

wall-pressure fluctuations on the upstream solid surfaces (8). The same mechanism applies to the stator (9). In this case, the potential effect creates a stationary pressure field distortion which yields periodic wall-pressure fluctuations on the rotor surface. For both mechanisms, the closer the surfaces are, the stronger the resulting acoustic source is.

Azimuthal non-uniformity In a real installation, the flow upstream of the rotor is not perfectly symmetric. The struts, the duct, or the geometrical irregularities generate an azimuthal non-uniformity which affects the blade loading and creates tones at the blade passing frequency (BPF) and its harmonics (10) [Sturm and Carolus, 2012].

Tip clearance recirculation Coherent backflow vortices create periodic blade loading fluctuations which radiate tonal noise (4).

On typical low-speed fans, the number of blades B ranges from 5 to 10, and the fan rotational speed Ω ranges from a 1500 to 3500 rpm. Consequently, the blade passing frequency BPF $= B\Omega/60$ ranges from 120 to 600 Hz. The noise radiation from a typical low-speed fan is thus dominated by low frequencies (see Figure 2.2).

From a psychoacoustic point of view, tonal noise has a greater impact on the acoustic discomfort compared with broadband noise [Gérard and Besombes, 2008; Zhang *et al.*,

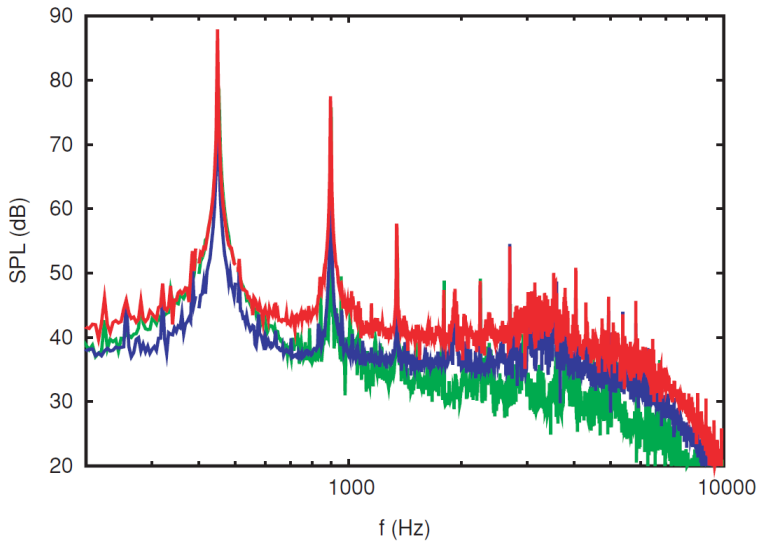

Figure 2.2 Typical acoustic spectrum radiated by a low-speed fan. Rotor contribution in green, stator contribution in blue, and overall radiation in red (from [Casalino *et al.*, 2010]).

2012]. Therefore, the present study focuses on the tonal radiation of low-speed fans. The following section presents different methods to control this type of noise.

2.2 Tonal noise control

Tonal noise control is classified into three categories: passive control, active control, and passive-adaptive control.

2.2.1 Passive control

The passive control methods are based on fixed modifications of the fan which act on the sound generation or the sound propagation.

Sound absorbing materials

The easiest method consists in the addition of acoustic damping materials at critical location in the vicinity of the fan in order to damp the noise propagation. This method is efficient from a relatively high frequency which is directly related to the thickness and mass of the material. The lower part of the spectrum is moderately damped, leading to a limited effect on the most energetic tones radiated by a fan.

Blade geometry

The blade geometry has a direct effect on the noise radiated. In particular, skewed blades are known to have a beneficial effect on noise [Carolus and Beiler, 1997]. Analytical models are often used to test a large number of geometries and optimize all the variables [Bommes *et al.*, 1995]. Additionally, numerical simulations coupled with genetic algorithms may yield an efficient optimization with a limited number of computations [Buisson *et al.*, 2013; Soulat *et al.*, 2013a; Tannoury, 2013].

Tip clearance geometry

The tip vortex developing at the blade tip may have a significant impact on the noise radiated by low-speed fans [Longhouse, 1977]. Longhouse [1978] showed that joining the blade tips with a rotating ring allows for the cancellation of the tip-vortex noise. Later on, Fukano *et al.* studied the impact of the tip-clearance variation on ducted-fan noise [Fukano *et al.*, 1986]. A smaller gap was shown to reduce tonal noise and increase the fan performance. The same effects are also noted when the rotor eccentricity is reduced. Unfortunately, these geometry modifications have a high impact on the fabrication cost, which is critical for fan manufacturers.

In an attempt to reduce the tangential velocity – swirl – of the tip clearance recirculation, DeFauw and Murley followed by several studies showed that a modification of the tip-clearance geometry yields a significant tonal noise reduction [DeFauw and Murley, 1974; Moreau *et al.*, 2006b,c; Park, 2009; Stairs and Greeley, 2002]. From an aerodynamic point of view, Soulat worked on the shroud geometry to reduce the recirculation flow rate and swirl and thus increase the fan performance [Soulat, 2010]. Additionally, Hong and Savage suggested to use the Coandă effect [1] to limit the flow recirculation in the tip clearance [Hong and Savage, 2009].

Blade spacing

Tonal noise is generated from a periodic flow non-uniformity. Several authors worked on the optimization of an irregular blade spacing in order to get an non-periodic flow distortion [Dobrzynski, 1993; Duncan and Dawson, 1974; Mellin and Sovran, 1970]. This modification does not reduce the overall sound power level but distributes the tone energy over a larger frequency range, which leads to smaller tone level and an improved comfort for the human ear. Despite the several studies conducted on this method, Cattanei *et al.* stated that more improvements can be achieved and proposed an optimization based on

1. The Coandă effect is the tendency of a fluid to be attracted by a nearby surface.

the rotor interference function [Cattanei *et al.*, 2007]. An experimental validation has been performed, but the tonal noise reduction of a real fan could not be demonstrated by Cattanei *et al.*.

Quarter-wavelength resonator

A quarter-wavelength resonator is a tube closed on one side by a rigid material and exposed to an acoustic radiation on the other side. In order to control a particular frequency, the tube length has to be equal to the fourth of the acoustic wavelength. Part of the primary acoustic wave enters in the tube, is reflected at the closed end, and comes out with an opposite phase. This principle applied to an axial fan is illustrated in Figure 2.3.

Neise and Koopmann were among the first to investigate the use of resonators to control tonal noise radiated by a fan [Neise and Koopmann, 1980]. This principle was first applied to a centrifugal fans where the quarter-wavelength resonator was placed in the volute tongue (Figure 2.5). A 23-dB attenuation was observed at the BPF inside the outlet duct, and the total sound power level showed a 7-dB(A) reduction. By keeping the original tongue geometry, the resonator does not impact the fan performance, which is one of the big assets of this technique.

In a later study, Koopmann and Neise showed the influence of the resonator setup on the acoustic directivity [Koopmann and Neise, 1982]. The tongue perforation was shown to have a direct influence on the noise control in the upstream or downstream part of the impeller. A simultaneous control in both directions was even possible with the addition of a thin separation plate inside the tongue.

As shown in Figure 2.3, Gorny and Koopmann studied the use of quarter-wavelength resonators around an axial fan in a duct [Gorny and Koopmann, 2009]. Optimization of the perforations at the connection between the resonators and the duct led to 12- and 5-dB SPL reduction at the BPF and its first harmonic, respectively, at a downstream location. However, the control was only possible in the upstream or downstream direction, but not in both simultaneously.

The passive control methods are simple to implement but their impact on tonal noise is often limited, particularly at low frequencies because of the long wavelengths. That is why several research group focus their studies on active control.

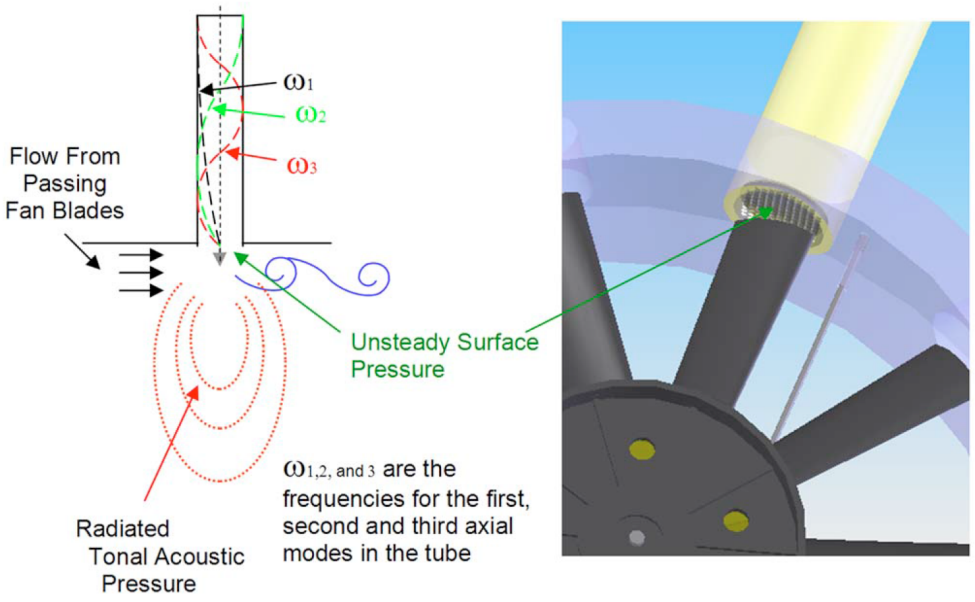

Figure 2.3 Tonal noise control of an axial fan with a quarter-wavelength resonator [Gorny and Koopmann, 2009].

2.2.2 Active control

The active control is a method based on the superposition of two acoustic waves: the primary wave generated by the noisy system and the secondary wave which is controlled to cancel the primary wave.

Active control with a secondary source

Several studies have been conducted to cancel the fan tonal noise with loudspeakers. This approach has been extensively studied to control turbofan noise [Maier *et al.*, 2001; Zillmann and Tapken, 2009]. Applying this method to computer cooling fans, Huang and Wang first studied the influence of the struts on the tonal noise [Huang, 2003; Huang and Wang, 2005]. After characterizing the primary source, they designed an active control method with one [Wang *et al.*, 2005] then several [Wang and Huang, 2006] loudspeakers. In the last study using four loudspeakers, a 13-dB global attenuation was achieved.

With a similar approach, Gérard *et al.* studied the tonal noise control of an engine cooling fan [Gérard *et al.*, 2005a,b]. The active control was based on the acoustic field extrapolation from reconstructed sources using the inversion of the Morse and Ingard's model. Experimental results showed 28- and 18-dB attenuation at the BPF and its first harmonic, respectively, at the error sensor location compared to overall SPL level.

Active control of the source

Lauchle *et al.* studied the tonal noise control of a fan by shaking the fan in the axial direction [Lauchle *et al.*, 1997]. Noise reductions of 20, 15 and 5 dB were obtained at the BPF and its first and second harmonics, respectively, at the location of the error sensor (in the experiment, a cylindrical obstruction was placed upstream of the fan to enhance the primary tonal radiation). However, it should be noted that this method requires a non-elastic liaison between the rotor and its axis, which is hardly applicable to low-speed fans since they are generally made of plastic composite.

Watkins, Piper and O'Brien based their studies on the same principle, but they controlled the fan displacement with magnetic bearings [O'Brien *et al.*, 1999; Piper, 2005; Watkins *et al.*, 1999]. A 4-dB reduction was observed at the error microphone location and a 3-dB attenuation elsewhere.

Adding actuators on the blades to generate vibrations is another method to reduce tonal noise. Kousen and Verdon showed with an analytical approach that the primary noise can be completely canceled if the number of actuators on the blades is equal to the number of acoustic modes to control [Kousen and Verdon, 1994]. More recently, Pasco *et al.* combined analytical and numerical models to achieve active control simulations of turbofan noise in duct [Pasco *et al.*, 2014a,b]. Without any knowledge of the physical field, a separation of the inlet and outlet radiation was achieved with the use of a generalized singular value decomposition.

Another technique consists in an active airflow control which reduces the azimuthal non-uniformities created by upstream obstructions [Andersson, 1997]. This method was investigated by Rao *et al.* with a microvalve-controlled fluid injection at the stator leading edge in order to attenuate the stator-rotor interaction [Rao *et al.*, 2001]. The BPF was reduced by 8 dB at a single microphone location. The same concept can also be applied to the blade trailing edge in the case of a rotor-stator interaction [Winkler, 2011]. Interested in tip clearance recirculation, Neuhaus and Neise studied the impact of airflow injection at the blade tip on the aerodynamic and acoustic performance [Neuhaus and Neise, 2002; Neuhaus *et al.*, 2003]. A steady injection led to a significant improvement of the aerodynamic performance, but also increased the noise at high flow rates. With an unsteady airflow, the control of the non-uniformity created by tip clearance backflow led to a BPF reduction of up to 20 dB at a single microphone in the outlet duct.

Although the active control is very efficient for some applications, it requires an additional energy supply and a complex control apparatus. Besides, the optimization of the algorithms

is often difficult and not particularly robust, which works against an industrially use of this method to reduce tonal noise, particularly for small, economical fans. Researchers found a technique which falls between the passive and the active control – the adaptive passive control.

2.2.3 Adaptive passive control

This control method is based on the controlled modification of the fan installation which creates a secondary source with the same amplitude, but opposite phase, as the primary noise radiated by the fan. This method is passive because it does not require an energy supply, and it is called adaptive as it can be adjusted to different operating conditions.

Quarter-wavelength resonator

If the length of a quarter-wavelength resonator is somehow controlled, the apparatus becomes a method of adaptive passive control.

Neise and Koopmann [1980] used a piston to control the resonator length (see Figure 2.5). This allowed the tonal noise control of a centrifugal fan in a large range of rotational speeds.

De Bedout worked on the automatic real-time adaptation of the resonator length [Bedout *et al.*, 1997; de Bedout, 1996]. A simple and robust algorithm was developed to control the tonal noise in a large range of rotational speeds. As long as the working conditions do not change, the resonator length stays the same. Therefore, in contrast with the active control techniques, this method needs very little energy supply.

Other studies applied this principle to high-speed turbomachines. Walker *et al.* worked to combine quarter-wavelength resonators with active sources to control tonal turbofan noise in duct [Walker *et al.*, 1999]. Following this work, a patent was issued [Hersh *et al.*, 2001]. Despite the fact that this study does not fall into the category of adaptive passive control, it appears that these developments are based on Neise and Koopmann's work.

Tip clearance design

An azimuthal variation of the tip clearance geometry can be used to create a secondary acoustic source induced by the blade rotation. Farrel and Gearhart [2002] issued a patent to reduce tonal fan noise using a sinusoidal variation of the casing geometry (Figure 2.6). With an optimal angular position and sinusoidal amplitude of the geometry variations, the pressure fluctuations on the fan blades cancel the fluctuations generated by the upstream

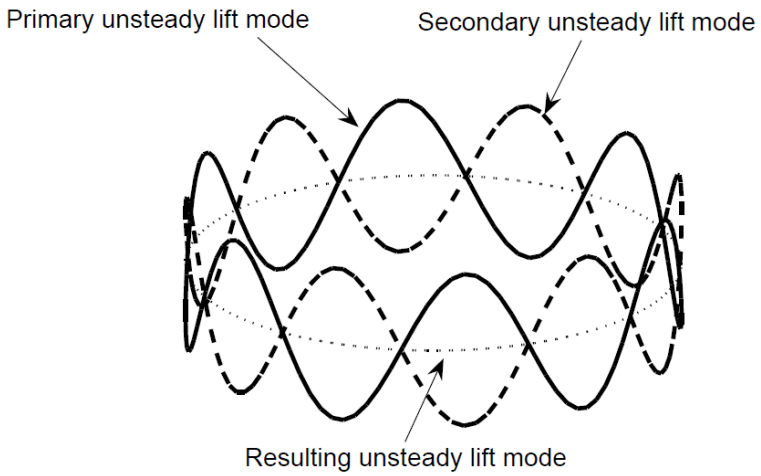

Figure 2.4 Tonal noise control using the generation of a secondary acoustic source [Gérard, 2006].

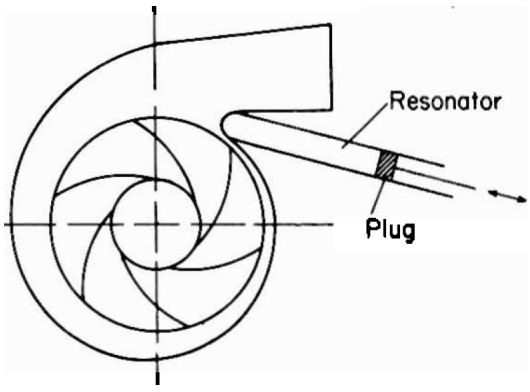

Figure 2.5 Tonal noise reduction of a centrifugal fan using a quarter wavelength resonator in the volute tongue [Neise and Koopmann, 1980].

stator vanes. Noise attenuations of 0.8, 8.2, and 7.2 dB were achieved at the BPF, its first, and its second harmonics, respectively (at a single location).

Obstructions

Fournier *et al.* were the first to use upstream obstructions in order to minimize the blade loading fluctuations and thus control tonal noise [Fournier *et al.*, 1994]. In this study, thick plates with a triangular trailing edge were introduced to compensate for the axial velocity deficit *in the rotor plane* induced by downstream stator vanes (Figure 2.7). In other words, the downstream distortion is canceled by the addition of upstream obstructions. The azimuthal variations of the velocity were divided by five, which led to a 14-dB noise reduction at the BPF.

Nelson investigated the influence of upstream perturbations on the noise radiation of a ducted turbofan [Nelson, 2000]. An analytical model was developed to evaluate the importance of each harmonic and vary the number of perturbations. The nature of the perturbation is not specified, but the author states that cylindrical obstructions or airflow injections can be used. Despite a significant noise reduction of two tones, an amplification of the others was observed.

Polacsek and Desbois-Lavergne carried out an experimental study to determine the influence of cylindrical obstructions placed upstream of an axial compressor in a duct [Polacsek and Desbois-Lavergne, 2003]. Measurements showed an 8-dB attenuation at the BPF. Additionally, a 2D unsteady RANS simulation was performed to compute the blade pressure fluctuations and propagate the acoustic sources with a Ffowcs-Williams & Hawkings (FW-H) analogy which was coupled with a Boundary Element Method (BEM) to account for

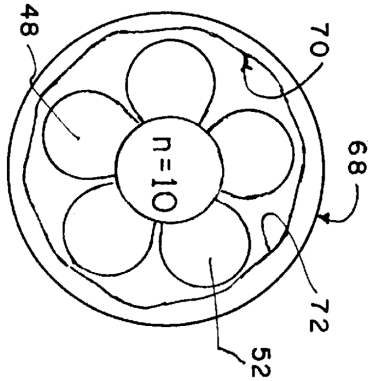

Figure 2.6 Modification of the tip clearance geometry to control tonal noise [Farrel and Gearhart, 2002].

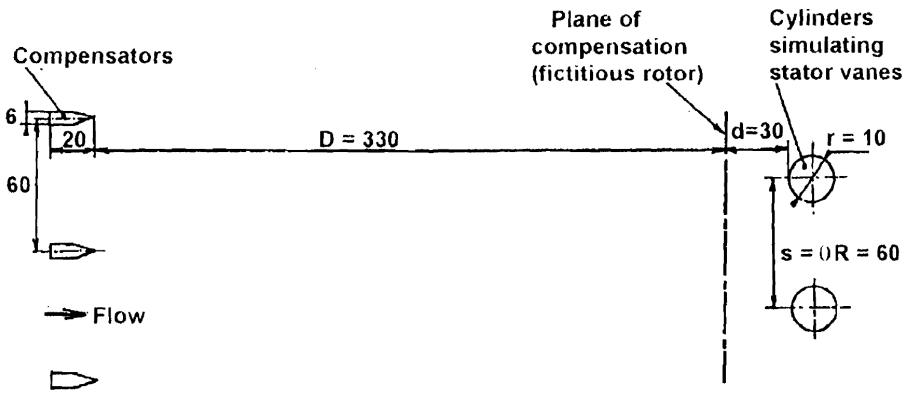

Figure 2.7 Upstream obstructions to control the blade loading fluctuations [Fournier *et al.*, 1994].

the sound propagation in a duct. A good agreement was observed between the numerical and experimental results – less than a 2-dB difference on the SPL at the BPF.

Neuhaus *et al.* placed cylindrical obstructions between the rotor and the stator of an axial compressor (Figure 2.8). A 12.6-dB tonal noise reduction was obtained at the BPF [Neuhaus *et al.*, 2003].

Kota and Wright were the first to look at automatic positioning of flow obstructions [Kota and Wright, 2006]. Their model was based on the work of Nelson [Nelson, 2000]. It consisted in controlling the inserted length of several radial cylinders in a duct in order to minimize the acoustic power level radiated by the fan (Figure 2.9). In the experimental configuration, the acoustic response was controlled by several microphones and the cylinder positioning was driven by a series of actuators. The acoustic results at low speed showed 6- and 8-dB attenuations at the BPF and its first harmonic. At higher speed, the number of propagating modes limited the algorithm convergence and the control efficiency.

Gérard *et al.* studied different types of obstructions (Figure 2.10) to control the noise radiation at the BPF without affecting the harmonics. An analytical model was developed to evaluate the harmonic content rate of the blade lift resulting from a Gaussian upstream velocity profile [Gérard *et al.*, 2009b]. This model was based on the infinitesimal radial strip theory coupled with the Sears' formulation to relate the one-dimensional incident gust to the unsteady lift [Sears, 1941]. Results showed that prominent obstructions similar to small cylinders are not ideal to control a single frequency. An experimental study on axial fans [Gérard *et al.*, 2009a] validated the analytical model with an indirect estimation of the harmonic content based on acoustic pressure measurements. Experiments in free field conducted with a sinusoidal obstruction yielded an 8-dB reduction of the sound power

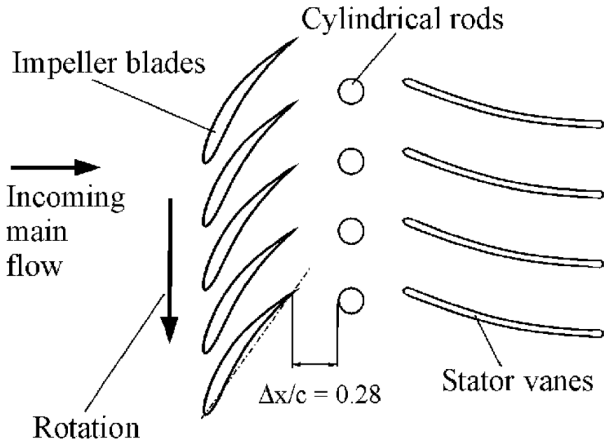

Figure 2.8 Tonal noise control with cylindrical obstructions [Neuhaus *et al.*, 2003].

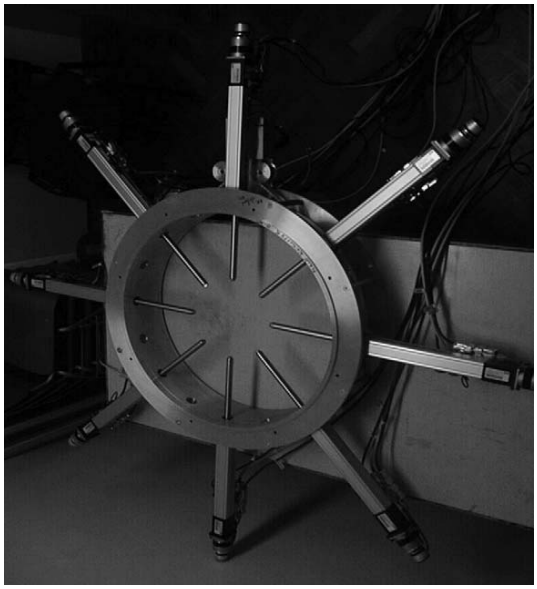

Figure 2.9 Adaptative passive control of tonal noise with cylindrical obstructions [Kota and Wright, 2006].

level and a 19-dB attenuation at the BPF. Moreover, the performance loss induced by the obtruction was estimated to be less than 2 %.

More recently, Goth *et al.* investigated the effect of the fan rotational speed on the noise reduction [Goth *et al.*, 2012]. In the studied configuration, measurements showed that an optimized obstruction could achieve a signification reduction of the sound power level at the BPF for large speed variations (several hundreds of rpm). Goth *et al.* even conjectured that the obstruction was the secondary sound source by mentioning: "When placed at the optimal distance and angle, the obstruction generates pressure pulsations that interact with the fan pressure fluctuations in a destructive way, allowing the cancellation of the noise. . . "

The secondary source created by the flow obstruction is optimized on two parameters: (1) the distance obstruction-fan or the obstruction lobe height controls the secondary source magnitude; (2) the obstruction angular position controls the source phase. Early in the development of this method, the optimization was an iterative process requiring extensive measurements. To accelerate the process, Gérard made an attempt to automatize the optimization of the obstruction position using step motors which controlled the axial and angular positions [Gérard, 2006]. More recently, a method based on the separation of the primary and secondary noise was investigated to optimize the obstruction design [Gérard *et al.*, 2013]. The separation was achieved by rotating the flow obstruction at about 3 % of the fan rotational speed in order to shift a secondary tone at a different frequency than the BPF (see Figure 2.11). In this study, the obstruction-fan distance was optimized by comparing the amplitude of the primary and secondary tones. When the distance is not optimal, the two tones have a different amplitude (Figure 2.11a). However, similar tone amplitudes indicate an optimal secondary source magnitude (Figure 2.11b).

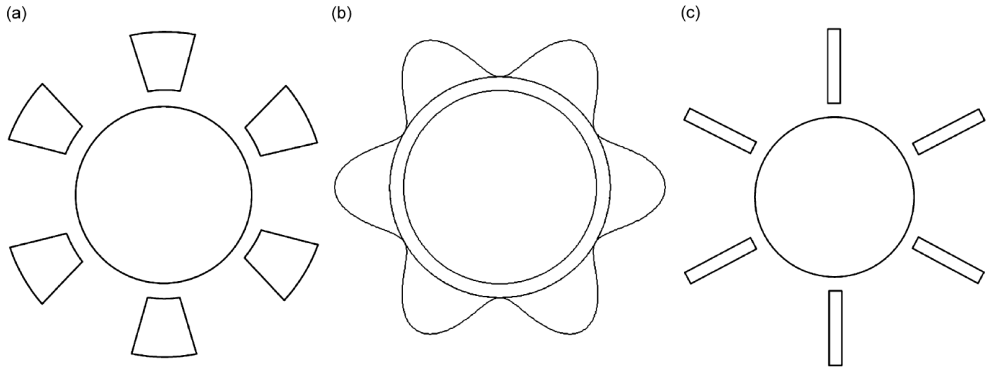

Figure 2.10 Obstruction types used by [Gérard *et al.*, 2009b] : (a) trapezoidal, (b) sinusoidal, (c) cylindrical.

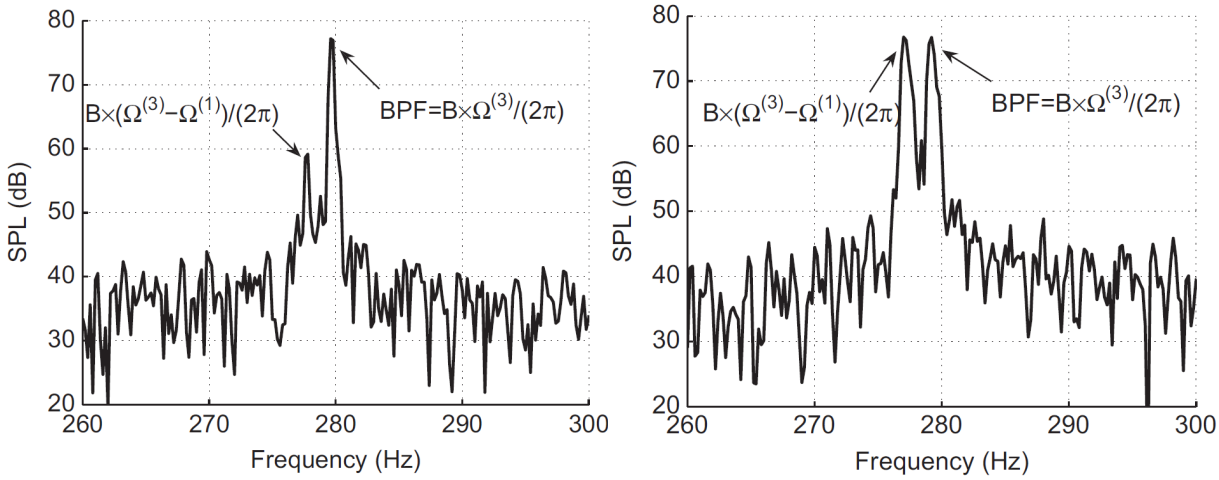

(a) Non-optimal obstruction axial position. (b) Optimal obstruction axial position.

Figure 2.11 Optimization of the obstruction axial position by rotating the obstruction [Gérard *et al.*, 2013].

As a first numerical investigation, Pérot *et al.* used a Lattice-Boltzmann method to predict the noise reduction of a centrifugal fan using a static obstruction [Pérot *et al.*, 2012]. The results showed that this approach correctly captures the effect of the obstruction on the BPF amplitude, and the prediction of the optimal angular position were in satisfying agreement with the experimental study. This initial study therefore highlighted the potential of numerical simulations to study the obstruction-fan interaction. Yet no clear conclusion was drawn from the actual noise control mechanism and whether the obstructions were generating noise or not.

2.3 Conclusion

First, the conducted literature review highlighted the noise mechanisms responsible for low-speed fan noise. Although both broadband and tonal contents have a significant impact on the acoustic signature, psycho-acoustic studies showed that tonal noise is a major annoyance for the humans.

An exhaustive description of the tonal noise control methods was presented. Three groups could be differentiated: passive, active, and adaptive-passive controls. Passive methods appear to be easy to implement, particularly at an early stage of the fan design. However, the associated noise reduction is often limited, particularly at low frequencies. Active control techniques can achieve large noise reductions on a large frequency range, but they require an additional energy supply and rely on algorithms which are often difficult to

optimize. Adaptive passive control is a good compromise. It does not require an energy supply and it yields moderate to large noise reduction at the BPF and its harmonics.

Among the adaptive passive methods, the use of flow obstructions appears to be a cheap, yet efficient way to reduce tonal noise. However, in the optimization process, this technique requires a physical prototype and iterative testing to yield some noise reduction. Moreover, an effective obstruction design is extremely difficult to achieve for certain fans [Magne *et al.*, 2014]. It thus appears that no criterion has been found to determine the controllability of a given configuration.

Most of the research conducted on tonal noise control with flow obstructions were based on experiments and simplified analytical models, which could not lead to a deep understanding of the obstruction-fan interaction. The first attempt to numerically predict the noise reduction showed a great potential to further investigate this noise control technique. Following this study, the present thesis focuses on a numerical approach to thoroughly understand the aeroacoustic phenomena responsible for the noise reduction and assess the actual acoustic impact of the obstruction. Moreover, the development of an industrially-applicable methodology to numerically design the obstruction is also explored as an alternative to extensive – and expensive – experiments.

CHAPTER 3

NUMERICAL METHODS

After presenting the acoustic sources radiated by a low-speed fan and the noise reduction techniques which could be implemented, the present chapter introduces the numerical methods used to predict the acoustic radiation. The aim is to select the methods and the computational codes which will be used to perform an extensive study of the obstruction-fan interaction.

Section 3.1 presents an introduction to computational aeroacoustics. The aerodynamic simulation methods are described in Section 3.2, whereas the acoustic propagation models are developed in Section 3.4. Finally, a test case is introduced in Section 3.5 to validate the chosen methods.

3.1 Introduction to computational aeroacoustics

The flow passing through a rotating machine can be characterized by the following two dimensionless quantities:

- The Mach number $M = U/c_0$, where U is the maximum flow velocity and c_0 is the sound velocity. In a typical low-speed fan, the maximum Mach number at the blade tip remains below 0.25, which indicates that no significant compressibility effects occur.
- The Reynolds number $\mathrm{Re} = U\,L/\nu$, where U is the mean flow velocity, L a characteristic linear dimension, and ν the kinematic viscosity. This quantity defines the ratio of inertial forces to viscous forces and characterizes the flow regimes, such as laminar or turbulent. For a typical low-speed fan, the Reynolds number based on the blade chord is about 10^5, which corresponds to a transition regime – between laminar and turbulent regimes.

Given the flow conditions, several numerical methods may be used to obtain acoustic results from an arbitrary fan geometry and installation environment. The term Computational AeroAcoustics (CAA) is often used to refer to these techniques which can be divided into two groups: the direct approach and the hybrid approach [1] [Colonius and Lele, 2004].

1. The hybrid approach is also referred as the indirect approach.

The direct approach relies on a *compressible* aerodynamic simulation to compute the noise sources and propagate the acoustic waves to the desired location. Given the order of magnitude of sound pressure fluctuations (< 1 Pa), the direct propagation requires low-dispersive and low-dissipative schemes combined with a fine and uniform grid. Wave reflections can occur at the boundaries of the computational domain, which imposes the use of non-reflective boundary conditions. Despite all the research studies conducted in the last decades, the direct noise prediction with traditional Navier-Stokes solvers remains challenging and time-consuming for the vast majority of applications. However, the development of the Lattice-Boltzmann Method has made direct predictions possible in an industrial context, particularly for low-speed applications (see more in Section 3.2.2).

The hybrid approach uses an aerodynamic simulation to compute the noise sources, whereas a second solver is used to propagate the sources and compute the sound pressure fluctuations at the desired location (see the different propagation techniques in Section 3.4). The simulation domain remains relatively small in comparison with the direct approach, which greatly reduces the computational cost. However, the acoustic prediction relies on the precision and the hypotheses of the acoustic analogy. With this approach, two types of data can be extracted from the aerodynamic simulation to feed the propagation code. On the one hand, the data are extracted from a compressible simulation on a porous surface in the near-field. In this case, the acoustic analogy allows for the dipolar *and* quadrupolar contributions.[2] On the other hand, only the wall pressure fluctuations are extracted from the aerodynamic simulation (which is not necessarily compressible). Consequently, only the dipolar sources are taken into account in the acoustic prediction. As stated in Chapter 2, the noise radiated by low-speed fans is mainly due to dipolar sources located on the fan surfaces. The propagation of the wall-pressure fluctuation is thus sufficient in the context of this thesis.

3.2 Aerodynamic simulation methods

3.2.1 Resolution of the Navier-Stokes equations

In fluid mechanics, the solution of the flow is based on the mass, the momentum, and the energy conservation. In the scope of aeroacoustic simulations, the *compressible* formulations of these principles are necessary to propagate the acoustic waves. The three corresponding equations used in Computational Fluid Dynamics (CFD) are reported below (external forces are considered negligible):

2. see Chapter 2 for a description of the different acoustic sources.

— The mass conservation:

$$\frac{\partial \rho}{\partial t} + \frac{\partial (\rho\, u_i)}{\partial x_i} = 0, \tag{3.1}$$

where ρ is the instantaneous density and u the fluid velocity. x and t represent the spatial and the temporal variables, respectively. Any suffix repeated in the terms is to be summed from 1 to 3.

— The momentum conservation:

$$\frac{\partial (\rho\, u_i)}{\partial t} + \frac{\partial}{\partial x_j} \left(\rho\, u_i\, u_j + p\delta_{ij} - \sigma_{ij}\right) = 0, \tag{3.2}$$

where $p\delta_{ij}$ is the pressure applied to the fluid surface, and σ_{ij} the viscous stress tensor.

— The energy conservation:

$$\frac{\partial (\rho\, E)}{\partial t} + \frac{\partial}{\partial x_j} \left(\rho\, u_j\, E + u_j\, p + q_j - u_i\, \sigma_{ij}\right) = 0, \tag{3.3}$$

where E is the total energy, and q_j the heat flux.

The equations obtained from these laws – called Navier-Stokes equations – are highly non-linear, which implies that they cannot be directly solved. Therefore, a spatial and temporal discretization is necessary for the computation to converge towards a stable solution.

The spatial discretization is determined by the mesh of the fluid domain which can be unstructured or structured. In the first case, each cell can have a variable number of adjacent cells (with a common face). This gives a good flexibility to discretize complex geometries, but implies an important storage of the mesh connectivity. Additionally, the implementation of high-order spatial schemes makes it difficult to solve the Navier-Stokes equations [Soulat, 2010]. As for the structured mesh, each cell is connected to six adjacent cells. The mesh is divided in blocks which are topological cubes. Each node is thus identified by a coordinate (i, j, k). This type of mesh facilitates the mesh structure and leads to a better control of the mesh size. However, complex geometries are more difficult to mesh, and the topological constraints often result in an increased number of cells in comparison with an unstructured mesh. With highly-swept and highly-skewed blades, cooling fans often present meshing challenges in the numerical pre-processing. Yet the development of efficient meshing products has greatly reduced the difficulties, and structured solvers are often used for low-speed fan applications [Liu *et al.*, 2007; Moreau and Casalino, 2005].

Temporal schemes ensure the discretization of the temporal terms of the Navier-Stokes equations. In a *steady* simulation, this discretization is used to converge the solution as fast as possible, which allows the use of different time steps across the simulation domain. In an *unsteady* simulation, the time step is the same across the whole computational domain and it is small enough to capture fluctuations of the mean quantities. Since the noise sources are related to time fluctuations, an unsteady computation is required in aeroacoustic applications. It should be noted that the temporal scheme stability is influenced by the smallest cell size and the local aerodynamic field. In practice, the time step is set to a value small enough to keep the scheme stable.

3.2.2 Turbulence modeling

As mentioned in Section 3.1, the flow passing through a low-speed fan is turbulent. In Navier-Stokes solvers, the turbulence can be computed from three main methods: the deterministic numerical resolution DNS (Direct Numerical Simulation), the semi-deterministic method LES (Large Eddy Simulation), and the statistical method RANS (Reynolds Averaged Navier-Stokes equations) [Marchesse, 2008]. In addition to that, a different approach, called Lattice-Boltzmann Method (LBM), may also be used to compute the turbulent flow past a fan. A representation of these methods is illustrated in Figure 3.1.

Direct Numerical Simulation

The DNS method directly solves the Navier-Stokes equations. All the turbulence scales are solved, which imposes a spatial discretization of the smallest structures. According to Choi and Moin [2012], a DNS simulation resolving the Kolmogoroff lengthscale requires $\mathrm{Re}^{37/14}$ mesh points. For this reason, *turbulent* DNS simulations are limited to simple geometries and small simulation domains. A DNS method is thus not applicable for low-speed fan applications ($\mathrm{Re} \approx 10^5$), as they would require 10^{13} grid points.

Large Eddy Simulation

The LES method only resolves the bigger turbulence structures and models the smaller scales. A spatial filtering is applied to select the turbulence scales which have to be modeled or solved. The computational cost is thus significantly reduced in comparison with the DNS, but this method still requires $\mathrm{Re}^{9/5}$ mesh points for $\mathrm{Re} \leq 10^6$ [Chapman, 1979]. Consequently, LES simulations are difficult to apply in an industrial context.

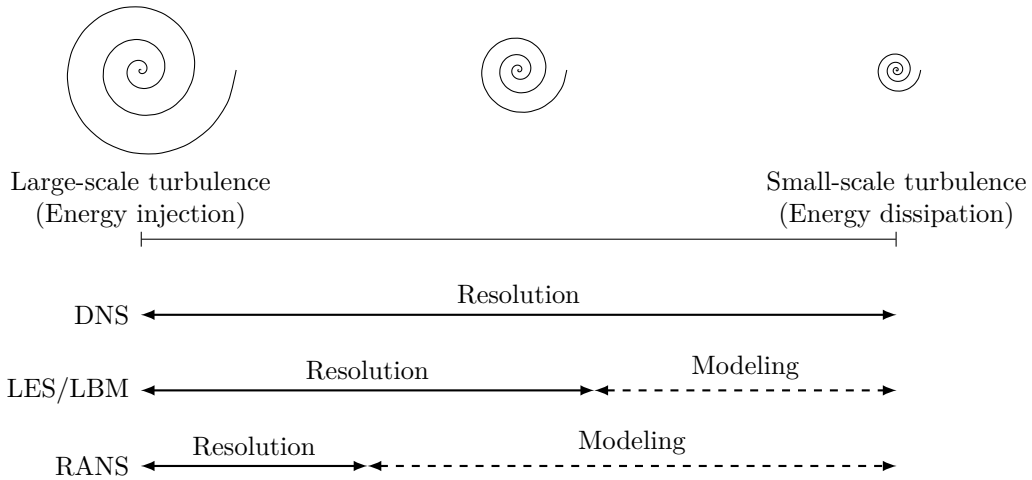

Figure 3.1 Representation of the different turbulence modeling methods (from [Marchesse, 2008]).

Reynolds Averaged Navier-Stokes

In the RANS method, only the averaged Navier-Stokes equations are solved, which results in the computation of the mean flow quantities and the use of turbulence models for all turbulence scales. However, an unsteady RANS (URANS) simulation is able to capture the impact of forced motions on the mean field, such as the large-scale fluctuations generated by the rotation of a fan blade. Consequently, tonal noise sources can be computed with this method.

Turbulence modeling allows the use of coarser meshes, which significantly reduces the computational cost. Although this method can appear to be imprecise in comparison with the DNS and LES, it remains the predominant technique used for low-speed fan application. Moreover, it is widely used by fan manufacturers.

In the present thesis, URANS simulations were performed with the code *Turb'Flow* developed at the LMFA in École Centrale de Lyon [LMFA, 2010]. This compressible, Navier-Stokes solver was designed to study rotating machines: compressors [De Laborderie, 2013], contra-rotating open rotors [Soulat *et al.*, 2013b], automotive cooling fans [Buisson *et al.*, 2013; Soulat, 2010], isolated airfoils [Henner *et al.*, 2000; Soulat *et al.*, 2013a], etc... Furthermore, Casalino [2002] and Boudet [2003] demonstrated the code abilities to simulate aeroacoustic phenomena. *Turb'Flow* thus appears to be particularly adapted to low-speed fan computations.

Lattice-Boltzmann Method

An alternative approach to the conventional Navier-Stokes equations was invented in the late 1980's with lattice gas method [Frisch *et al.*, 1986]. This method was based on the displacement of particles on a discrete lattice, and the local collisions allowed for the mass and momentum conservation. However, the unstable nature of the lattice gas method as well as the additional terms in the Navier-Stokes-level equations limited its success [Chen and Doolen, 1998]. In order to eliminate these drawbacks, the discrete particles were replaced by a density distribution to form the LBM [Pérot *et al.*, 2010b; Sanjosé *et al.*, 2011].

While the accuracy and robustness of the LBM have been demonstrated on diverse aeroacoustic applications, it should be noted that the discrete velocity model influences the validity of this approach at high Mach number. For instance, the tri-dimensional 19-state model (D3Q19, Figure 3.2) does not correctly capture the flow physics for Mach numbers $M > 0.5$ [Lew *et al.*, 2007].

For low-speed fan applications ($M < 0.3$), the LBM is an excellent alternative to the Navier-Stokes solvers. In the present study, the commercial software *PowerFLOW*, developed by Exa Corporation, was used for all the LBM computations [Exa Corporation, 2012]. Based on the D3Q19 discrete velocity model, *PowerFLOW* uses different reference frames to account for the rotation of geometrical parts relatively to others [Pérot *et al.*, 2010b].

This solver showed excellent predictions for a variety of low-speed applications [Lafitte and Pérot, 2009; Lew *et al.*, 2007; Maldonado *et al.*, 2012; Pérot *et al.*, 2010a], and particularly fan noise predictions [Moreau *et al.*, 2011; Pérot *et al.*, 2010b]. Moreover, Alstom Transport SA, collaborator of this project, currently uses this code for aeroacoustic predictions.

3.3 Solver discretizations

3.3.1 Turb'Flow

The resolution of the Navier-Stokes equations is equivalent to finding the solution of the partial differential equation

$$\frac{\partial \boldsymbol{A}}{\partial t} + \frac{\partial B}{\partial x_i} = \boldsymbol{D}, \tag{3.4}$$

where $\boldsymbol{A}$ and $\boldsymbol{D}$ are vectors and B is a tensor. In *Turb'Flow*, the resolution on the structured mesh is based on the finite volume method centered on the nodes [Boudet, 2003].

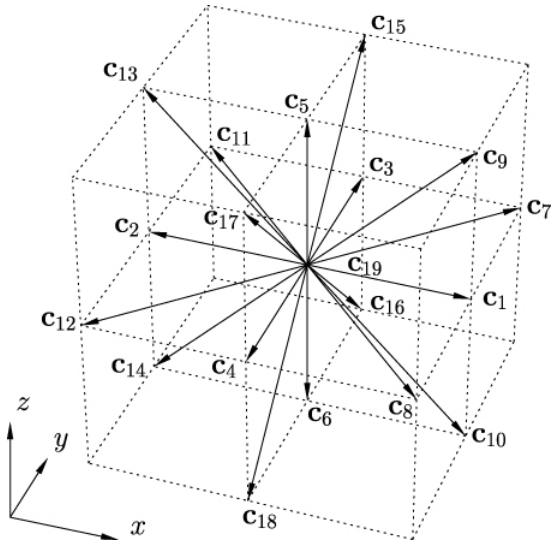

Figure 3.2 Discrete velocity model D3Q19 used in LBM.

For each cell of volume $V(t)$ and surface $S(t)$, Equation (3.4) becomes:

$$\frac{\mathrm{d}}{\mathrm{d}t}\int_{V(t)} \boldsymbol{A}\,\mathrm{d}V + \int_{S(t)} C\cdot\boldsymbol{n}\,\mathrm{d}S = \int_{V(t)} \boldsymbol{D}\,\mathrm{d}V, \tag{3.5}$$

where C corresponds to the tensor B for a stationary mesh, and $\boldsymbol{n}$ is the vector normal to the surface pointing outwards. *Turb'Flow* computes the integrals from the values at the grid points and the interpolated values at the center of the cell surfaces. The temporal discretization is ensured by a Runge-Kutta scheme, whereas several schemes are implemented to discretize the spatial terms. However, only the schemes used in the present thesis (Jameson's [Jameson *et al.*, 1981] and Liou's AUSM+ [Liou, 1996]) are presented here.

Jameson's scheme

Jameson's spatial scheme is centered on the cell. Given $\boldsymbol{q}$ the vector of conservative variables, the flux in the direction l at the interface between the nodes of coordinate $i-1$ and i (see Figure 3.3) is given by [Soulat, 2010]:

$$\mathcal{F}^l_{i-1/2} = \mathcal{F}^l(\boldsymbol{q}_{i-1/2}), \tag{3.6}$$

where

$$\boldsymbol{q}_{i-1/2} = -\frac{1}{12}\left(-\alpha\,\boldsymbol{q}_{i-2} + (\alpha+6)\boldsymbol{q}_{i-1} - (\alpha+6)\boldsymbol{q}_i + \alpha\,\boldsymbol{q}_{i+2}\right) \tag{3.7}$$

with $\alpha = 0$ for a second-order scheme or $\alpha = 1$ for a fourth-order scheme. This approximation of $\boldsymbol{q}_{i-1/2}$ does not introduce any dissipation, which is important to propagate small fluctuations in aeroacoustic applications. However, the lack of dissipation generates instabilities. To keep the scheme stable, a dissipative flux $\mathcal{F}_d$ is added to the formulation:

$$\mathcal{F}^l_{d,i-1/2} = \mathcal{J}(u_l + c|\boldsymbol{a}|)_{i-1/2} \left(\frac{1}{2}\epsilon_2(\boldsymbol{q}_i - \boldsymbol{q}_{i-1}) + \frac{1}{8}\epsilon_4(\boldsymbol{q}_{i+1} - 3\boldsymbol{q}_i + 3\boldsymbol{q}_{i-1} - \boldsymbol{q}_{i-2}) \right), \quad (3.8)$$

where $\mathcal{J}$ is the Jacobian, a is the contravariant vector, and ϵ_2 and ϵ_4 are the second and fourth-order numerical viscosity coefficients, respectively. Consequently, the complete flux at the interface $\mathcal{F}_c$ is given by:

$$\mathcal{F}^l_c = \mathcal{F}^l + \mathcal{F}^l_d. \quad (3.9)$$

In the *Turb'Flow* solver, the two numerical viscosity coefficients (ϵ_2 and ϵ_4) are set by the user, but this additional dissipation should be minimized to correctly propagate acoustic waves.

Liou AUSM+

Liou's Advection Upstream Splitting Method+ (AUSM+) is an upwind spatial scheme which separates the flux into a purely convective term $\mathcal{C}^l$ and a pressure term $\mathcal{P}^l$ [Liou, 1996]:

$$\mathcal{F}^l = \mathcal{C}^l + \mathcal{P}^l, \quad (3.10)$$

where

$$\mathcal{C}^l = \mathcal{J}c^m \begin{pmatrix} M^{l+}\rho^L + M^{l-}\rho^R \\ M^{l+}(\rho u_1)^L + M^{l-}(\rho u_1)^R \\ M^{l+}(\rho u_2)^L + M^{l-}(\rho u_2)^R \\ M^{l+}(\rho u_3)^L + M^{l-}(\rho u_3)^R \\ M^{l+}(\rho E + p)^L + M^{l-}(\rho E + p)^R \end{pmatrix} \quad (3.11)$$

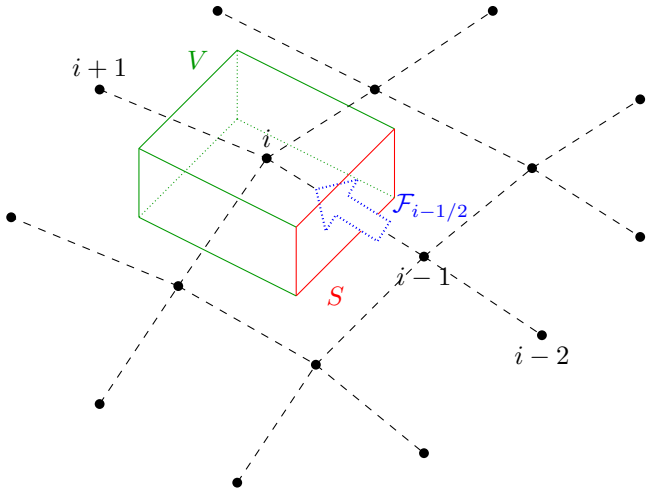

Figure 3.3 Volume discretization and flux at the surface of a cell (adapted from Boudet [2003]).

and

$$\mathcal{P}^l = \mathcal{J} \begin{pmatrix} 0 \\ (p^{l+}p^L + p^{l-}p^R)\frac{\partial l}{\partial x_1} \\ (p^{l+}p^L + p^{l-}p^R)\frac{\partial l}{\partial x_2} \\ (p^{l+}p^L + p^{l-}p^R)\frac{\partial l}{\partial x_3} \\ -(p^{l+}p^L + p^{l-}p^R)\frac{\partial l}{\partial t} \end{pmatrix} \tag{3.12}$$

c^m is the mean speed of sound at the interface, L/R exponents define the values at the left and right of the cell interface, respectively, and Liou's Mach number is given by $M^{l\pm} = (M^l \pm |M^l|)/2$. Consequently, the sign of M^l defines whether the left or the right terms are used to evaluate the flux. In the pressure term $\mathcal{P}^l$, $p^{l\pm}$ is defined in a similar manner to select which terms to use.

Unlike a centered scheme which uses values from each side of the face to evaluate the flux, an upwind scheme uses only the cells in the upstream direction [Soulat, 2010]. For this reason, upwind schemes are adapted to transonic and supersonic applications, but they generate a relatively large dissipation in zones with low Mach numbers. For this reason, Liou's scheme does not appear to be ideal for the simulation of a low-speed fan. Nevertheless, this scheme was used on the validation test case (Section 3.5) to compare the results with Jameson's scheme.

3.3.2 PowerFLOW

In the LBM, the density distribution function of particles $f_i(\boldsymbol{x}^*, t^*)$ corresponds to the mass per unit volume of the particles at the time t^*, at the position $\boldsymbol{x}^*$, and with the velocity $\boldsymbol{c}_i^*$ [Pérot *et al.*, 2010b; Sanjosé *et al.*, 2011]. i refers to the i^{th} direction according to a finite set of discrete velocity vectors (see Figure 3.2) and * denotes the dimensionless quantities used by the solver. The Lattice-Boltzmann advection equation is thus given by

$$f_i(\boldsymbol{x}^* + \boldsymbol{c}_i^* \Delta t^*, t^* + \Delta t^*) - f_i(\boldsymbol{x}^*, t^*) = C_i(\boldsymbol{x}^*, t^*), \tag{3.13}$$

where C_i is the collision operator, Δt^* the time increment, and $\boldsymbol{c}_i^* \Delta t^*$ the space increment. In *PowerFLOW*, C_i is approximated by the Bhatnagar-Gross-Krook (BGK) form [Bhatnagar *et al.*, 1954] which drives the particle distribution to the local equilibrium distribution function f_i^{eq} with the relaxation time t':

$$C_i(\boldsymbol{x}^*, t^*) = -\frac{1}{t'}\Big(f_i(\boldsymbol{x}^*, t^*) - f_i^{eq}(\boldsymbol{x}^*, t^*)\Big), \tag{3.14}$$

where t' is the relaxation time which is related to the dimensionless kinematic viscosity $\nu^* = c_s^{*2}(t' - \Delta t^*/2)$. f_i^{eq} is approximated by a second order expansion valid for low Mach numbers:

$$f_i^{eq} = \rho^* w_i \left(1 + \frac{\boldsymbol{c}_i^* \cdot \boldsymbol{u}^*}{c_s^{*2}} + \frac{(\boldsymbol{c}_i^* \cdot \boldsymbol{u}^*)^2}{2c_s^{*4}} - \frac{|\boldsymbol{u}^*|^2}{2c_s^{*2}}\right), \tag{3.15}$$

where w_i is a weighting factor relative to the discrete velocity model, and $c_s^* = 1/\sqrt{3}$ the dimensionless speed of sound [Chen and Doolen, 1998]. Additionally, the local hydrodynamic properties ρ^* and $\boldsymbol{u}^*$ are obtained through summation of the discrete momentum:

$$\rho^*(\boldsymbol{x}^*, t^*) = \sum_i f_i(\boldsymbol{x}^*, t^*) \tag{3.16}$$

$$\rho^* \boldsymbol{u}^*(\boldsymbol{x}^*, t^*) = \sum_i \boldsymbol{c}_i^* f_i(\boldsymbol{x}^*, t^*) \tag{3.17}$$

Consistent with the formal solutions of the transient, viscous, and compressible Navier-Stokes equations, this method is easily parallelized because of the local aspect of the algorithm. This approach is used to simulate resolvable flow scales while the turbulence fluctuations are computed by replacing the molecular relaxation time t' with an effective turbulent relaxation time t'_{eff} derived from the resolution of a Re-Normalization Group

(RNG) $k-\epsilon$ underlying model [Fares, 2006]. This is why the LBM is often associated with a Very Large Eddy Simulation (VLES).

In the case of a fan, an axisymmetric interface is defined between the Local Reference Frame (LRF) domain attached to the rotor, and the global reference frame attached to the stationary parts (ground). Inside the LRF, Equation (3.13) is modified to include the external body force term $\boldsymbol{E}_i(\boldsymbol{x}^*, t^*)$ [Guo *et al.*, 2002; Pérot *et al.*, 2010b]:

$$f_i(\boldsymbol{x}^* + \boldsymbol{c}_i^* \Delta t^*, t^* + \Delta t^*) - f_i(\boldsymbol{x}^*, t^*) = -\frac{1}{t'}\Big(f_i(\boldsymbol{x}^*, t^*) - f_i^{eq}(\boldsymbol{x}^*, t^*)\Big) + \boldsymbol{E}_i(\boldsymbol{x}^*, t^*) \quad (3.18)$$

3.4 Acoustic propagation models

With a hybrid approach (see Section 3.1), an additional solver is used to propagate the acoustic sources in the far field. Three types of codes can be distinguished: the linearized Euler's equations (LEE), the Kirchhoff formulation, and the acoustic analogies.

The LEE model is a numerical method which computes the radiated sound from the near-field aerodynamic flow [Bogey *et al.*, 2002]. This technique accounts for the propagation effects due to complex geometries, but introduces spurious waves which can interfere with the acoustic waves. Also, the numerical propagation to the far-field may induce large computational cost relatively to the other acoustic models based on integral formulations.

The Kirchhoff method propagates the sources from a *stationary* surface to the far field using the wave equation (linear propagation) [Lyrintzis, 2002]. Consequently, the acoustic sources and the non-linear effects are assumed to be inside the surface. As seen in Section 2.1, in a typical low-speed fan configuration, tonal noise sources are located on the solid surfaces and particularly the rotating blades. Therefore, the Kirchhoff method cannot be used to propagate the dipolar sources located on the fan.

The acoustic analogies include several integral formulations for acoustic propagation. Extending the early works of Lighthill [1952] and Curle [1955], Ffowcs Williams and Hawkings [1969] (FW-H) developed an elegant formulation which accounts for the movement of sources. For this reason, the FW-H analogy is extensively used for fan noise prediction.

Before presenting the FW-H formulation in Setion 3.4.3, the following two sections introduce the Lighthill's and Curle's analogies.

3.4.1 Lighthill's analogy

Lighthill's analogy [Lighthill, 1952] is a model of the sound generated by a small region of turbulent flow embedded in an infinite, homogeneous fluid in which the speed of sound c_0 and the density ρ_0 are constant [Goldstein, 1976]. Although this analogy does not include the effect of solid surfaces such as a fan blade, this work is presented here as the foundation of the analogies which are introduced in the following sections.

Lighthill's formulation is derived from the gas kinetic equations. Subtracting the spatial derivation of momentum equation (3.2) to the temporal derivation of continuity equation (3.1) gives

$$\frac{\partial^2 \rho}{\partial t^2} - \frac{\partial^2 (\rho\, u_i\, u_j)}{\partial x_i\, \partial x_j} = \frac{\partial^2}{\partial x_i\, \partial x_j} \left(p\delta_{ij} - \sigma_{ij}\right) \tag{3.19}$$

Additionally, the following expressions are introduced:

$$\rho' = \rho - \rho_0, \tag{3.20}$$

$$p' = p - p_0, \tag{3.21}$$

$$c_0^2 = \gamma \frac{p_0}{\rho_0} \tag{3.22}$$

where ρ_0 is the fluid density at rest, p_0 the pressure at rest, ρ' and p' the density and pressure fluctuations, respectively, c_0 the sound velocity in the fluid at rest, and γ the specific heat ratio.

Inserting Equations (3.20) and (3.21) in Equation (3.19), Lighthill's equation is given by

$$\frac{\partial^2 \rho'}{\partial t^2} - c_0^2 \frac{\partial^2 \rho'}{\partial x_j^2} = \frac{\partial^2 T_{ij}}{\partial x_i\, \partial x_j} \tag{3.23}$$

where

$$T_{ij} = \rho u_i u_j + (p' - c_0^2 \rho')\delta_{ij} - \sigma_{ij} \tag{3.24}$$

is the Lighthill's tensor and δ_{ij} the Kronecker delta ($\delta_{ij} = 0$ if $i \neq j$; and $\delta_{ij} = 1$ if $i = j$).

Assuming that the acoustic fluctuations and the source terms can be separated, the solution of this pseudo-wave equation can be formally solved using the free-field Green's function:

$$\rho'(\boldsymbol{x},t) = \frac{1}{4\pi c_0^2}\int_V \frac{1}{r}\frac{\partial^2 T_{ij}(\boldsymbol{y},t-r/c_0)}{\partial y_i\,\partial y_j}\mathrm{d}V, \tag{3.25}$$

where $\boldsymbol{x}$ and $\boldsymbol{y}$ are the observer and source location vectors, respectively, and $r = |\boldsymbol{x}-\boldsymbol{y}|$ the distance between the observer and the source (see Figure 3.4). The integral is written over the whole space V, but the integrand is non-zero only over the source distribution.

If the observer is located many wavelengths away from the source (far field), any function $f(t-r/c_0)$ verifies

$$\frac{\partial^2 f(t-r/c_0)}{\partial y_i \partial y_j} = \frac{(x_i-y_i)(x_j-y_j)}{r^2 c_0^2}\frac{\partial^2 f(t-r/c_0)}{\partial t^2}. \tag{3.26}$$

Consequently, Equation (3.25) can be transformed into a temporal derivation:

$$\rho'(\boldsymbol{x},t) = \frac{1}{4\pi c_0^2}\int_V \frac{(x_i-y_i)(x_j-y_j)}{r^3 c_0^2}\frac{\partial^2 T_{ij}(\boldsymbol{y},t-r/c_0)}{\partial t^2}\mathrm{d}V. \tag{3.27}$$

In the far field, $(x_i - y_i)$ can be approximated by x_i, provided that the origin is taken within the flow. Finally, for an isentropic flow in which ρ'/ρ_0 is relatively small, the solutions of

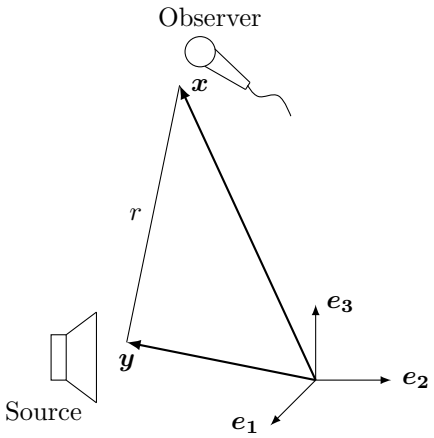

Figure 3.4 Sketch of the source and observer vectors.

the sound pressure fluctuation $p' = \rho' c_0^2$ are

$$p'(\boldsymbol{x},t) = \frac{1}{4\pi|\boldsymbol{x}|}\int\limits_V \frac{\partial^2 T_{ij}(\boldsymbol{y},t-r/c_0)}{\partial y_i\,\partial y_j}\mathrm{d}V \tag{3.28}$$

$$p'(\boldsymbol{x},t) = \frac{1}{4\pi c_0^2}\frac{x_i\,x_j}{|\boldsymbol{x}|^3}\int\limits_V \frac{\partial^2\, T_{ij}(\boldsymbol{y},t-r/c_0)}{\partial t^2}\mathrm{d}V. \tag{3.29}$$

It should be noted that the Equation (3.25) cannot be solved directly. In his article [Lighthill, 1952], Lighthill suggests for low Mach numbers and high Reynolds numbers the following simplification: $T_{ij} \approx \rho_0\, v_i\, v_j$, where $\boldsymbol{v}$ is the incompressible velocity fluctuation due to the turbulence (acoustic fluctuations are neglected). Allowing the equation resolution, this approximation is extensively used in aeroacoustics.

3.4.2 Curle's analogy

Curle's analogy [Curle, 1955] is a generalization of Lighthill's analogy. In addition to the quadrupolar term, this formulation adds two terms which account for the noise radiated by the solid surfaces in the flow. Despite the stationary state of the solid surfaces, this work was an important contribution to aeroacoustics. More importantly for fan noise prediction, it led to the development of the Ffowcs-Williams & Hawkings' analogy which includes the movement of sources (see Section 3.4.3).

In Curle's analogy, the acoustic pressure fluctuation is

$$p'(\boldsymbol{x},t) = \frac{1}{4\pi}\frac{\partial^2}{\partial y_i\,\partial y_j}\int\limits_V \frac{T_{ij}(\boldsymbol{y},t-r/c_0)}{r}\mathrm{d}V \tag{3.30a}$$

$$-\frac{1}{4\pi}\frac{\partial}{\partial y_i}\int\limits_S \frac{p'(\boldsymbol{y},t-r/c_0)}{r}\,n_i\,\mathrm{d}S \tag{3.30b}$$

$$+\frac{1}{4\pi}\frac{\partial}{\partial t}\int\limits_S \frac{[\rho\,\bar{u}_i](\boldsymbol{y},t-r/c_0)}{r}\,n_i\,\mathrm{d}S, \tag{3.30c}$$

where S is the solid surface and $\boldsymbol{n}$ is the vector normal to the surface (pointing outwards), and $\bar{\boldsymbol{u}}$ is the suction/injection velocity vector at the surface. The first integral (3.30a) is taken from Lighthill's equation (3.25), the second term (3.30b) corresponds to the dipolar source generated on the surface, and the third term (3.30c) is the monopolar radiation created by the mass flux through the surface (fluid injection or suction).

Following the same approximations used in the Lighthill's development, it can be demonstrated that the dipolar radiation in the far field is given by

$$p'(\boldsymbol{x},t) = -\frac{x_i}{4\pi c_0|\boldsymbol{x}|^2}\frac{\partial}{\partial t}\int_S p'(\boldsymbol{y}, t - r/c_0)\, n_i \,\mathrm{d}S. \tag{3.31}$$

3.4.3 Ffowcs-Williams & Hawkings' analogy

FW-H analogy generalizes Lighthill's and Curle's equations to account for the movement of the acoustic sources [Ffowcs Williams and Hawkings, 1969]. The space is divided into two sub-spaces bounded by the surface S which moves at the velocity $\boldsymbol{V}(\boldsymbol{x},t)$ (see Figure 3.5). S includes all the acoustic sources – the rigid surfaces and the turbulent fluctuations – and the outside of S is only fluid at rest. In the formulation, two functions $f(\boldsymbol{x},t)$ and $H(f)$ are introduced to formalize the problem:

— $f(\boldsymbol{x},t) = 0$ on S, outside $f > 0$ and inside $f < 0$;
— $H(f) = 1$ when $f > 0$ and $H(f) = 0$ when $f < 0$ (Heaviside function).

Given these functions, the equations of mass and momentum conservation are rewritten in a single equation:

$$\begin{aligned}\frac{\partial^2 \rho'\, H(f)}{\partial t^2} - c_0^2\frac{\partial^2 \rho'\, H(f)}{\partial x_i^2} = \;& \frac{\partial^2 T_{ij}\, H(f)}{\partial x_i\, \partial x_j} \\ & -\frac{\partial}{\partial x_i}\Big(L_i \delta(f)\Big) \\ & +\frac{\partial}{\partial t}\Big(\rho_0\, U_i\, n_i\, \delta(f)\Big).\end{aligned} \tag{3.32}$$

with

$$L_i = (p'\delta_{ij} - \sigma_{ij})n_j + \rho\bar{u}_i(\bar{u}_i n_i - V_i n_i) \tag{3.33}$$

$$U_i = \left(1 - \frac{\rho}{\rho_0}\right) V_i + \frac{\rho}{\rho_0}\bar{u}_i \tag{3.34}$$

The first term in Equation (3.32) corresponds to the volume sources (quadrupoles), the second one takes into account the radiation from the solid surfaces (dipoles), and the third term characterizes the thickness noise (monopoles).

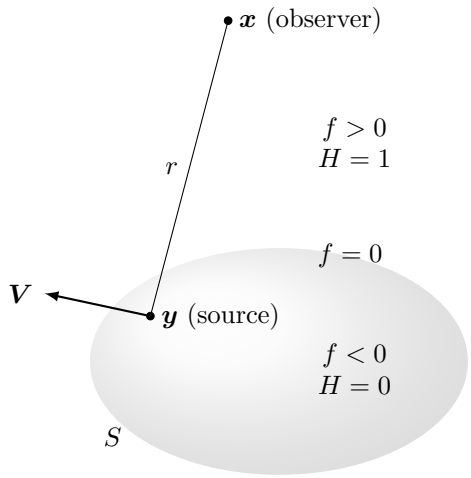

Figure 3.5 Sketch of Ffowcs-Williams & Hawkings' analogy.

Using the free-field Green's function, the solution of the acoustic pressure fluctuation is

$$\begin{aligned} 4\pi\, p'(\boldsymbol{x},t) = \quad & \frac{\partial^2}{\partial x_i\, \partial x_j} \int\int_V \left[\frac{T_{ij}}{r}\right] \mathrm{d}V \mathrm{d}t'' \\ & -\frac{\partial}{\partial x_j} \int\int_S \left[\frac{L_i}{r}\right] \mathrm{d}S \mathrm{d}t'' \\ & +\frac{\partial}{\partial t} \int\int_S \left[\frac{\rho_0\, U_i\, n_i}{r}\right] \mathrm{d}S \mathrm{d}t'', \end{aligned} \tag{3.35}$$

where $\boldsymbol{n}$ is the vector normal to the surface and the brackets symbolize the evaluation at the time $(t - t'' - r/c_0)$, with t'' the source emission time.

In the present thesis, the code *FoxWHawk* [Casalino, 2009] was used to propagate the acoustic sources with the FW-H analogy. This code, developed by Casalino [2003], is based on the conversion of the retarded-time formulation of Brentner and Farassat [1998] into a forward-time formulation of the FW-H equation proposed by Difrancescantonio [1997]. This change allows a concurrent flow/noise simulation and, therefore, enhances the flexibility and the computation time efficiency of the acoustic propagation [Casalino *et al.*, 2010; Moreau *et al.*, 2006a]. Since quadrupolar noise is negligible in the scope of this thesis, only the monopolar and dipolar radiation terms were computed by *FoxWHawk*. The expressions of these two contributions are reported below (see [Casalino, 2003] for the complete development).

Monopolar noise

$$4\pi p'(\boldsymbol{x},t) = \int_S \left[\frac{\rho_0(\dot{U}_n + U_{\dot{n}})}{r\,(1-M_r)^2}\right] \mathrm{d}S + \int_S \left[\frac{\rho_0 U_n \left(r\dot{M}_r + c_0(M_r - M^2)\right)}{r^2(1-M_r)^3}\right] \mathrm{d}S, \tag{3.36}$$

where M_r is the projection of a point source Mach number on the source-observer line, and the other terms are given by

$$U_n = U_i n_i \tag{3.37}$$

$$U_{\dot{n}} = U_i \dot{n}_i \tag{3.38}$$

$$\dot{U}_n = \dot{U}_i n_i \tag{3.39}$$

Dotted quantities denote time derivative with respect to the source time.

Dipolar noise

$$\begin{aligned} 4\pi p'(\boldsymbol{x},t) = &\frac{1}{c_0}\int_S \left[\frac{\dot{L}_r}{r\,(1-M_r)^2}\right] \mathrm{d}S + \int_S \left[\frac{L_r - L_M}{r^2(1-M_r)^2}\right] \mathrm{d}S \\ &+ \frac{1}{c_0}\int_S \left[\frac{L_r \left(r\dot{M}_r + c_0\,(M_r - M^2)\right)}{r^2(1-M_r)^3}\right] \mathrm{d}S, \end{aligned} \tag{3.40}$$

where L_r and L_M are the projection of L_i on the source-observer line and the movement direction, respectively.

In the present work, Equations (3.36) and (3.40) are solved at the forward-time t_{adv} which is equal to the sum of the emission time and the propagation time between the source and the observer.

3.4.4 Compact rotating dipole analogy

For large acoustic wavelengths with respect to the blade span, the pressure fluctuation on a fan blade can be seen as a compact rotating dipole [Goldstein, 1976]. In a typical low-speed axial fan with a blade span $l_s = 150$ mm , this condition is verified for frequencies below $\omega = c_0\, l_s^{-1} = 2280$ Hz. Given typical B and Ω in low-speed fan applications (see Section 2.1.2), the tonal noise prediction is generally valid for the BPF and the first three harmonics.

For a compact source, the dipolar noise radiated by a point fluctuating force in arbitrary motion can be derived from Equation (3.35):

$$p'(\boldsymbol{x},t) = \left[\frac{(x_i - y_i)}{(1-M_t)c_0 R'}\frac{\partial}{\partial t}\left(\frac{F_i}{4\pi R'(1-M_t)}\right)\right], \tag{3.41}$$

where

$$F_i = \int_S p(\boldsymbol{y},t) n_i dS \tag{3.42}$$

is the fluctuating force acting on the blade, R' the source-observer distance, and $M_t = \Omega\, R_0\, c_0^{-1}$ the tangential Mach number at the radius R_0 (see sketch in Figure 3.6). The brackets denote the evaluation at the retarded time t_e which verifies the equation:

$$t_e - t + \frac{R'}{c_0} = 0, \tag{3.43}$$

which is equivalent to

$$t_e - t + \frac{R}{c_0}\left(1 - 2\sin\theta\frac{R_0}{R}\cos(\Omega t_e - \varphi) + \left(\frac{R_0}{R}\right)^2\right)^{1/2} = 0, \tag{3.44}$$

where (R,θ,φ) are the spherical coordinates of the observer $\boldsymbol{x}$. Consequently, the resolution is difficult at the retarded time, but necessary to study time-based mechanisms such as the *beating* noise from a helicopter. For any other purpose, Equation (3.41) is transformed in the frequency domain, which eliminates the retarded time calculation and allows an easier and faster resolution. The formulation is then simplified based on the assumption that the noise sources on each rotor blade can be approximated by a compact rotating dipole (the complete development is presented in Appendix A). Consequently, the formulation of the acoustic pressure in the far field radiated by a single blade is

$$\tilde{p}(\boldsymbol{x},\omega) = \frac{i\omega}{8\pi^2 c_0}\int_{-\infty}^{+\infty}\frac{\boldsymbol{F}\cdot\boldsymbol{x}}{|\boldsymbol{x}|^2}e^{i\omega(t-\boldsymbol{x}(t)/c_0)}\mathrm{d}t, \tag{3.45}$$

where ω is the angular frequency and the tilde denotes the frequential quantity. Besides, the force $\boldsymbol{F}$ can be decomposed in harmonics s of the rotational frequency:

$$\tilde{\boldsymbol{F}}(\omega) = \sum_{s=-\infty}^{+\infty}\boldsymbol{F}^s\,\delta(\omega - s\Omega), \tag{3.46}$$

where $\boldsymbol{F}^s$ are the Fourier coefficients of the fluctuating force $\tilde{\boldsymbol{F}}$. For a B-blade rotor, it can be shown that the sound is radiated at the frequencies $mB\Omega$, where m is the order of the harmonic radiated (see Appendix A). The expression of the acoustic pressure radiated by the complete rotor is given by:

$$\begin{aligned}\tilde{p}(\boldsymbol{x}, mB\Omega) = &\frac{imB^2\Omega e^{imB\Omega R/c_0}}{4\pi c_0 R} \\ &\times \sum_{s=-\infty}^{+\infty} e^{i(mB-s)\left(\varphi-\frac{\pi}{2}\right)}\Bigg[F_R^s \sin\theta J'_{mB-s}(mBM_t\sin\theta) \\ &+ \left(F_A^s\cos\theta - F_T^s\tfrac{mB-s}{mBM_t}\right) J_{mB-s}(mBM_t\sin\theta)\Bigg],\end{aligned} \tag{3.47}$$

where J_α is the Bessel function of the first kind of order α; and F_A^s, F_R^s, F_T^s are the Fourier coefficients of the axial, radial, and tangential force components, respectively.

The large majority of fan aeroacoustic studies currently relies on *incompressible* codes (low Mach number) coupled with an acoustic analogy for the sound propagation (high Reynolds number). The present study will however focus on two different approaches using *compressible* solvers characterized by a low dissipation and a low dispersion:

— *Turb'Flow*: a Navier-Stokes solver dedicated to turbomachinery and used in aeroacoustics [LMFA, 2010];
— *PowerFLOW*: an LBM solver which includes an LRF formulation to account for the fan rotation [Exa Corporation, 2012].

3.5 Validation – Flow past a cylinder

The numerical methods to perform aeroacoustic computations were presented in the previous sections. Before performing simulations of a low-speed fan configuration, the selected codes (*Turb'Flow* and *PowerFLOW*) were validated on a simpler test case to characterize their properties and check accuracy and mesh requirements. Additionally, this case allowed the comparison of different acoustic analogies (Curle, FW-H and the compact rotating dipole) in order to validated the chosen sound propagation code (*FoxWHawk*).

The acoustic radiation of the flow past a cylinder has been extensively studied for more than one hundred years; hence it is an excellent validation case for the aforementioned aeroacoustic codes.

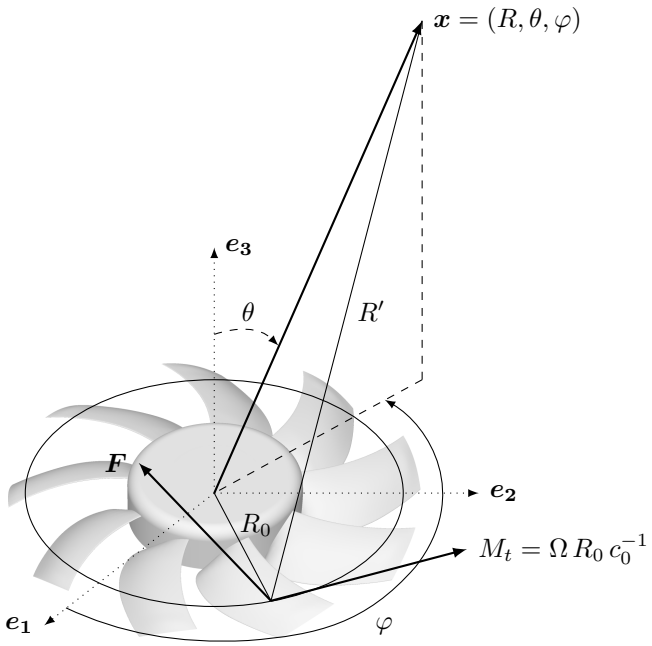

Figure 3.6 Sketch of the compact rotating dipole analogy.

3.5.1 Aerodynamic and acoustic regimes of the flow past a cylinder

The noise radiated by the flow past a blunt body (cylindrical or square rod, airfoil...) is of prime importance for understanding the aeroacoustic sources related to the turbulence as well as the boundary layer separation and reattachment. Initiated more than one hundred years ago by the works of Strouhal [1878] and Kármán [2013], this research area is still active. The evolution of experimental and numerical techniques leads to a more precise characterization of the aeroacoustic phenomena, and the study of the flow past a cylinder remains very interesting considering the diversity of the regimes which can be observed. These regimes mainly depend on the non-dimensional Reynolds number based on the cylinder diameter

$$\mathrm{Re}_D = \frac{U_\infty D}{\nu_\infty}, \tag{3.48}$$

where D is the cylinder diameter, U_∞ the mean flow velocity, and ν_∞ the mean kinematic viscosity. The following sections describe the four main regimes which can be distinguished [Pérot, 2004; Sumer and Fredsoe, 2006; Williamson, 1996].

Steady, laminar regime: $\mathrm{Re} \leqslant 49$

For a Reynolds number below 5, no separation is observe – the flow follows the cylinder surfaces (see Figure 3.7a). Above $\mathrm{Re} = 5$, a flow separation appears and creates two

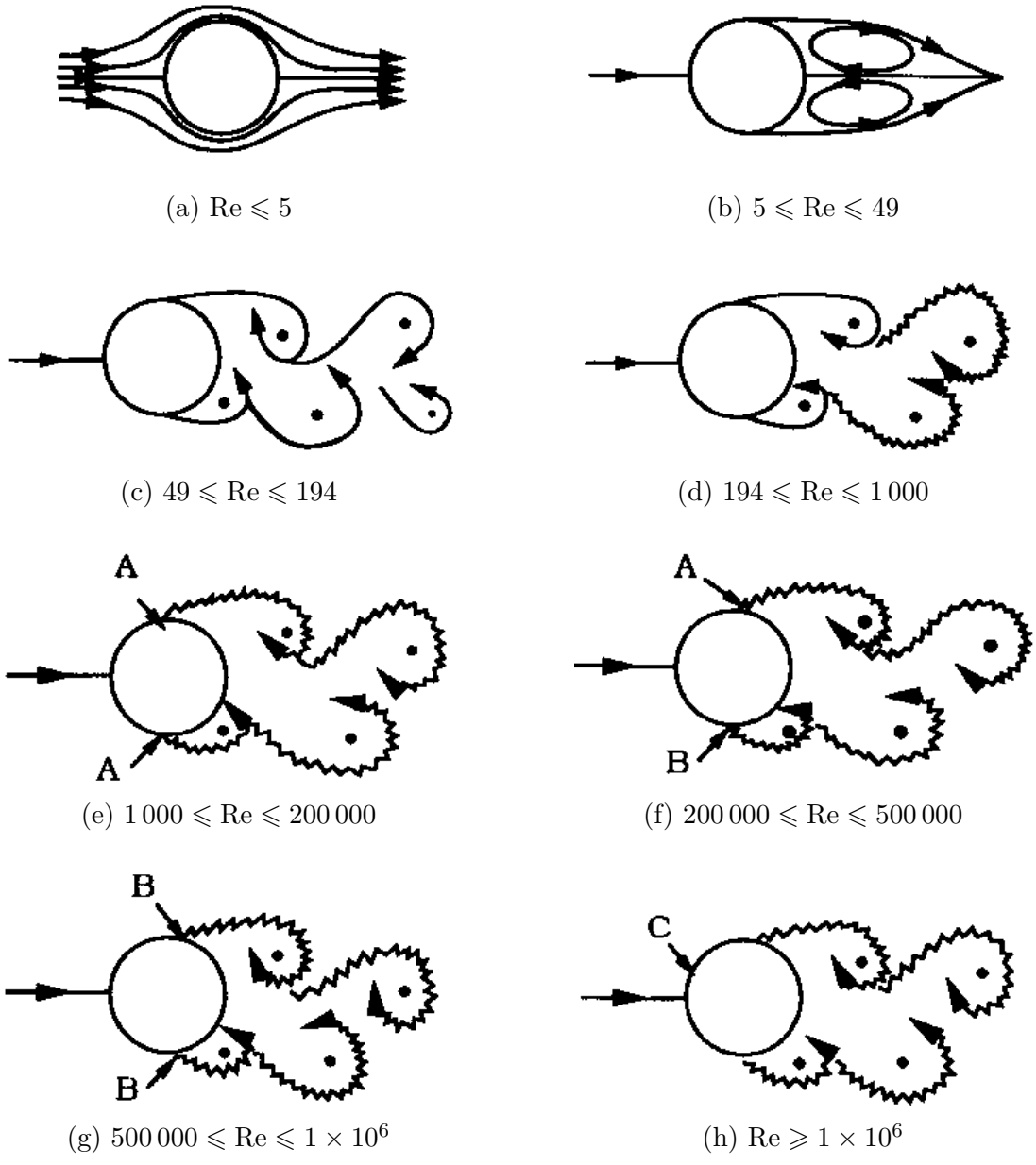

(a) $\mathrm{Re} \leqslant 5$

(b) $5 \leqslant \mathrm{Re} \leqslant 49$

(c) $49 \leqslant \mathrm{Re} \leqslant 194$

(d) $194 \leqslant \mathrm{Re} \leqslant 1\,000$

(e) $1\,000 \leqslant \mathrm{Re} \leqslant 200\,000$

(f) $200\,000 \leqslant \mathrm{Re} \leqslant 500\,000$

(g) $500\,000 \leqslant \mathrm{Re} \leqslant 1 \times 10^6$

(h) $\mathrm{Re} \geqslant 1 \times 10^6$

Figure 3.7 Regimes of the flow past a cylinder [Sumer and Fredsoe, 2006].

recirculations downstream of the cylinder (Figure 3.7b). This laminar regime remains perfectly steady for $\mathrm{Re} \leqslant 49$. Therefore no noise is radiated at this regime.

Wake-transition regime: $49 \leqslant \mathbf{Re} \leqslant 1\,000$

Beyond $\mathrm{Re} = 49$, the recirculations are destabilized. This constitutes the first step of the transition from a laminar to a fully turbulent regime. The cylinder wake becomes unsteady, and an oscillation of the surface pressure coefficient appears (Figure 3.7c). This phenomenon is known as the Kármán vortex street (Figure 3.7d). The vortex shedding frequency f is often characterized by the non-dimensional Strouhal number

$$\mathrm{St} = \frac{fD}{U_\infty}. \tag{3.49}$$

The wake oscillations create periodic wall-pressure fluctuations at the vortex-shedding frequency. Therefore, tonal noise is radiated by the cylinder at the frequency f and its harmonics.

For $49 \leqslant \mathrm{Re} \leqslant 194$ the regime remains stable and the wake, laminar. Above $\mathrm{Re} = 194$, a discontinuity can be observed in the evolution of the Strouhal number as a function of the Reynolds number. This discontinuity is induced by turbulent three-dimensional structures appearing in the Kármán vortex street. Vortex pairings are observed in the transverse direction, which characterizes the so called mode A (Figure 3.8a). This pattern has a 3-diameter characteristic length. When the Reynolds number reaches 230, a second discontinuity appears in the Strouhal evolution. Finer transverse structures with a 1-diameter characteristic length are then observed, which is called mode B (Figure 3.8b). The modes A and B coexist up to $\mathrm{Re} \approx 250$ (hysteresis), but beyond $\mathrm{Re} = 250$ only the mode B exists and an increase of the turbulence with the Reynolds number is observed.

Shear-layer transition regime: $1\,000 \leqslant \mathbf{Re} \leqslant 200\,000$

For Reynolds numbers above 1 000, two-dimensional structures, called Kelvin-Helmholtz instabilities, appear in the shear layers (Figure 3.7e). A complex interaction between these structures and the Kármán vortices appears, which induces a decrease of the Strouhal number and an increase of the pressure coefficient at the cylinder downstream point.

In addition to the tonal noise radiated by the vortex-shedding, the collisions and distortions of the turbulent structures which appear at this regime create a broadband acoustic source.

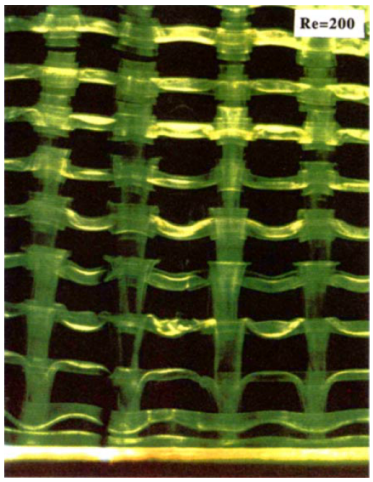

(a) Mode A: $194 \leqslant \mathrm{Re} \leqslant 250$.

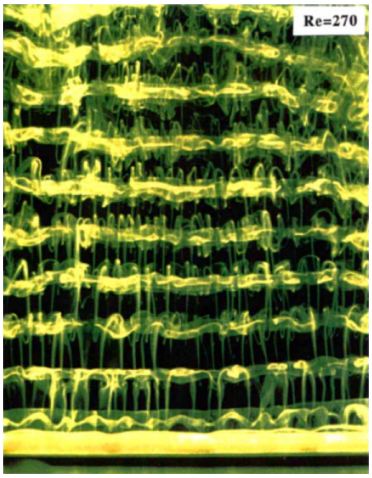

(b) Mode B: $\mathrm{Re} \geqslant 250$.

Figure 3.8 Experimental visualization of the transition modes observed downstream a cylinder [Williamson, 1996]. The cylinder is horizontal, at the bottom of the images; the flow is vertical, from the bottom to the top.

Boundary-layer transition regime: Re $\geqslant 200\,000$

For $200\,000 \leqslant \mathrm{Re} \leqslant 500\,000$, the drag coefficient drops significantly and, as a consequence of the boundary-layer separation and transition, the separation point moves further downstream. A recirculation bubble is observed on one side, which creates an asymmetrical regime (Figure 3.7f). Additionally, the vortex shedding width decreases, which causes the rise of the Strouhal number. This transition is called critical regime.

For Reynolds numbers between $500\,000$ and 1×10^6, the regime becomes supercritical. Two symmetric recirculation bubbles are developed, which increases the flow stability. The pressure coefficient is almost invariant in this interval.

Beyond $\mathrm{Re} = 1 \times 10^6$, the regime is post-critical. The recirculation bubbles disappear and the boundary layers become fully turbulent from the stagnation point (Figure 3.7h).

As for the noise radiation, the increase of the turbulent intensity generates stronger broadband sources along with the tonal noise created by the vortex shedding.

3.5.2 Simulation setups

Since the present thesis is focused on tonal noise, the acoustic codes were validated on an unsteady laminar regime which yields a strong dipolar source at the shedding frequency. The Reynolds number was fixed to $\mathrm{Re}_D = 150$ in order to compare the results with the works

of Inoue and Hatakeyama [2002] and Lafitte and Pérot [2009]. The corresponding regime is two-dimensional, fully laminar and unsteady with a Kármán vortex street developed downstream of the cylinder (see Section 3.5.1). Additionally, the Mach number was chosen to give a velocity magnitude close to what is typically found in low-speed fan applications ($M = 0.2$). The cylinder diameter was computed from the aforementioned conditions to ensure normal atmospheric pressure and temperature [3]. All the simulation parameters are reported in Table 3.1.

This simple test case aims at validating:

— The direct propagation of the acoustic waves with the compressible codes;
— The noise prediction based on acoustic analogies;
— The influence of different spatial schemes with a Navier-Stokes solver.

Turb'Flow and *PowerFLOW* were used to perform the two-dimensional aeroacoustic simulations. Considering the laminar regime of the flow past the cylinder, no turbulence models were needed and DNS were performed with both codes.

Turb'Flow simulations

With *Turb'Flow* 1.9.0 [LMFA, 2010], the compressible Navier-Stokes equations were directly solved with an explicit method. A Runge-Kutta method with 3 steps was used to discretize the temporal terms, yielding a good compromise between precision and performance. Additionally, a convergence study showed that the stability of the computation was maintained with 4 000 iterations per vortex shedding period. With a shedding frequency $f_0 = 3.8972 \times 10^5$ Hz, the time-step was set to 6.41×10^{-10} s.

3. The velocity is defined by the Mach number and the kinematic viscosity depends on the pressure and temperature conditions. Therefore, the definition of the Reynolds number (Equation 3.48) shows that the cylinder diameter is the only parameter which can be modified to set the Reynolds number.

Table 3.1 Parameters used in the simulation of the flow past a cylinder.

Cylinder diameter	D	$= 3.24 \cdot 10^{-5}$ m
Reynolds number	Re_D	$= 150$
Mach number	M	$= 0.2$
Speed of sound	c_∞	$= 343$ m.s^{-1}
Flow velocity	U_∞	$= 69$ m.s^{-1}
Temperature	T_∞	$= 293$ K
Static pressure	P_∞	$= 1.0 \cdot 10^5$ Pa
Kinematic viscosity	ν_∞	$= 1.49 \cdot 10^{-5}$ m^2.s^{-2}

Four spatial schemes were tested: Jameson's centered scheme of 2nd and 4th order [Jameson *et al.*, 1981], and Liou's Advection Upstream Splitting Method+ (AUSM+) of 2nd order [Liou, 1996]. As stated in Section 3.2.2, Jameson's centered scheme is low dissipative and well suited for aeroacoustic applications. Due to its larger dissipation in low-speed zones, Liou's upstream scheme is more dedicated to supersonic applications, but was tested in the present study to compared the results with Jameson's scheme.

Two structured grids were generated with *Gridgen* 15.17 [Pointwise, 2010]: a circular and an octagonal mesh (Figures 3.9a and 3.9b, respectively). The parameters of the meshes are presented in Table 3.2. As for the circular mesh, the cell size is constant in the radial direction up to a damping zone where the size ratio is relatively large. In the octagonal grid, the cell size follows a geometrical progression with a ratio of 1.07. It should be noted that although the circular mesh has a greater number of cells, the boundary layer is more finely resolved with the octagonal mesh. Additionally, both meshes have a large cell size at the outer edge (relatively to the acoustic wavelength λ_0) to ensure that no wave reflections occur on the boundary condition.

A static pressure boundary condition with a free flow direction was applied at the outer edge of the simulation domain, leaving the code decide whether a node is an inlet or an outlet depending on the velocity vector orientation. With this type of condition combined with a circular mesh, a purely horizontal flow may cause singularities at the top and bottom nodes. Therefore, an octagonal shape was tested to see the effect of these singularities. At the center of the domain, an adiabatic, non-slip boundary condition was applied to the cylinder wall.

PowerFLOW simulation

Table 3.2 Geometrical parameters of the meshes used to compute the flow past a cylinder (λ_0 is the acoustic wavelength at the vortex shedding frequency f_0).

	Turb'Flow		*PowerFLOW*
	Circular mesh	Octagonal mesh	Square mesh
Cell number	162 816	40 320	36 078 288
External diameter	$300 \times D$	$408 \times D$	$400 \times D$
First cell size	431 nm	24.1 nm	203 nm
Last cell size	346 µm $\approx \frac{1}{3}\lambda_0$	679 µm $\approx \frac{2}{3}\lambda_0$	13 µm
Cell size ratio	1.0 + damping	1.07	2.0 (Cartesian)

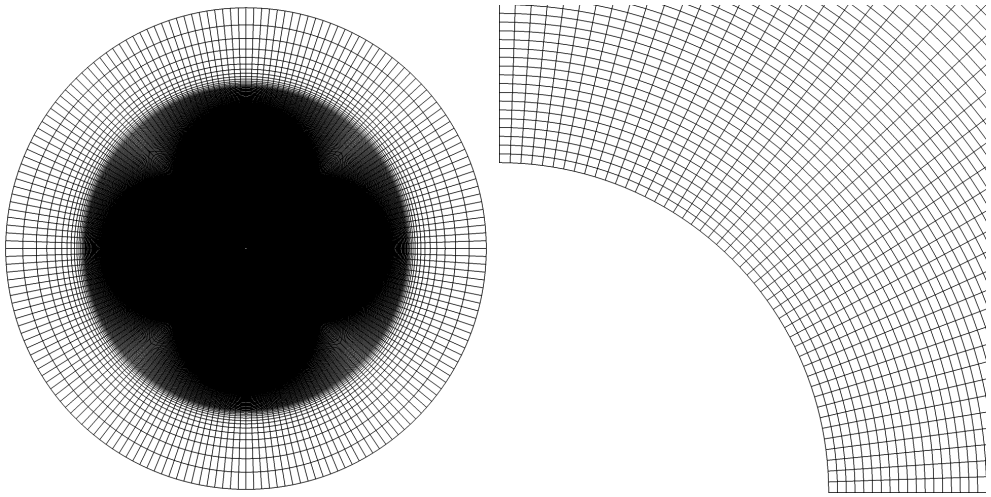

(a) *Turb'Flow*: Circular mesh (constant cell size in the radial direction followed by a damping zone).

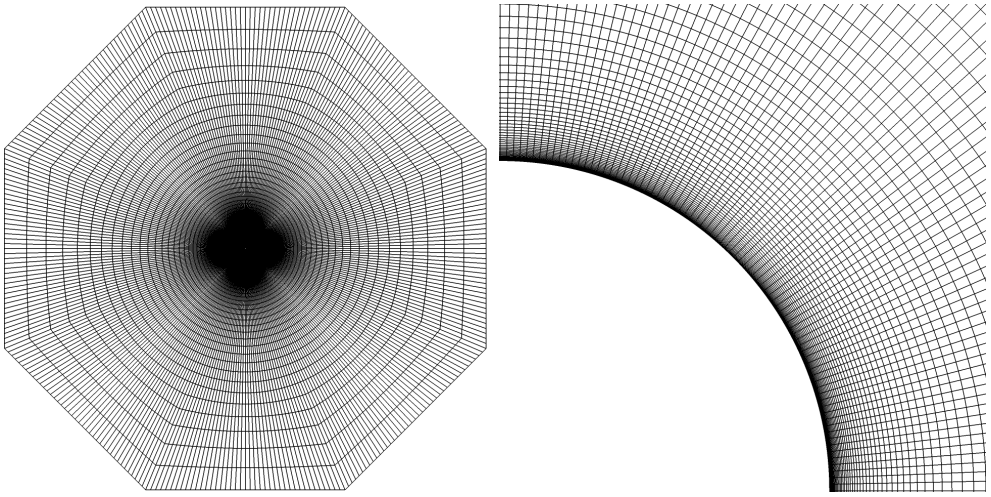

(b) *Turb'Flow*: Octagonal mesh (cell size ratio of 1.07 in the radial direction).

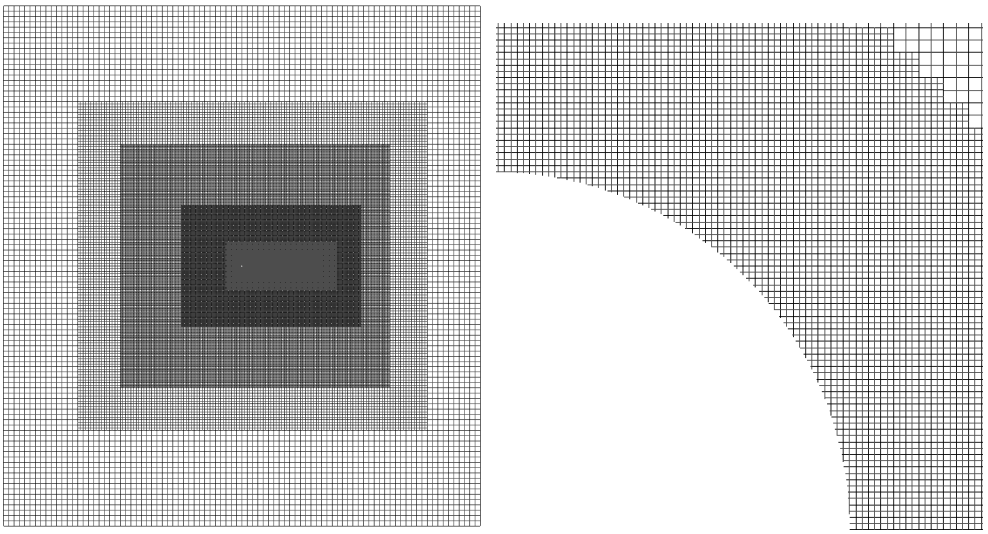

(c) *PowerFLOW*.

Figure 3.9 Meshes used in the simulations (left: full domain; right: zoom on the cylinder surface).

In addition to the *Turb'Flow* solver, an LBM simulation was performed with *PowerFLOW* 4.2a. With this code, the mesh is Cartesian and automatically generated from Variable Resolution (VR) regions where the grid size changes by a factor of two for two adjacent regions of voxels. In the present setup, the cylinder was placed in the middle of a 400-D-long, square domain (see Figure 3.9c). Seven VR were used with a 203-nm smallest voxel. Although the largest cell was relatively small compared with the *Turb'Flow* meshes (see Table 3.2), three viscosity volumes changed the local viscosity in the outer regions and absorbed the acoustic waves coming from the cylinder.

Similarly to the *Turb'Flow* simulations, a static pressure boundary condition with a free flow direction was imposed at the outer edges of the domain, and an adiabatic, no-slip boundary condition was applied to the cylinder wall. Additionally, the time-step was set to 3.378×10^{-10} s to ensure the stability of the temporal scheme in the finest regions.

It should be noted that, despite the lager number of cell in the *PowerFLOW* setup (see Table 3.2), *Turb'Flow* was twice slower – each vortex shedding period was computed in 17.5 and 32 Central Processing Units (CPU) hours for *PowerFLOW* and *Turb'Flow*, respectively. However, given the present study, this speed difference was considered as acceptable.

3.5.3 Aerodynamic results

In the *Turb'Flow* simulations, the mesh and the spatial scheme did not significantly influence the aerodynamic results; hence the results presented in this section are valid for all the schemes and both meshes.

As expected for this Reynolds number ($Re = 150$), a vortex shedding is observed in the flow downstream of the cylinder. The non-dimensional instantaneous vorticity $\widetilde{\omega} = D\omega/c_\infty$ is presented in Figure 3.10. The Kárman vortex street is well developed, and the vorticity levels are in very good agreement with Inoue and Hatakeyama [2002].

The aerodynamic results with *Turb'Flow* and *PowerFLOW* are compared with the works of Inoue and Hatakeyama [2002] and Lafitte and Pérot [2009] in Table 3.3. Five quantities are presented: the Strouhal number St, the time-averaged drag coefficient C_D, and its fluctuation amplitude c'_D, and the fluctuation amplitude of the lift coefficient c'_L. A very good agreement is observed for all the quantities. The drag coefficient C_D shows the largest discrepancies, but lower values of C_D are also found in literature (Marsden [2005]: $C_D = 1.330$; Henderson [1995], $C_D = 1.335$). Additionally, it should be noted that the acoustic prediction is directly related to the fluctuation of the forces acting on the cylinder surface rather than the mean value of the lift and drag.

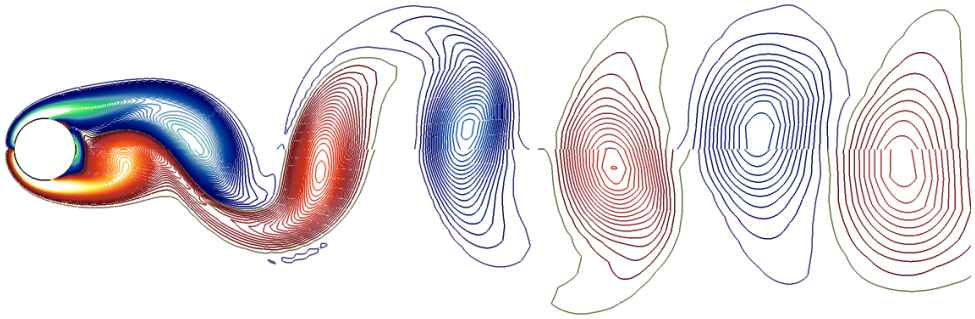

(a) *Turb'Flow*.

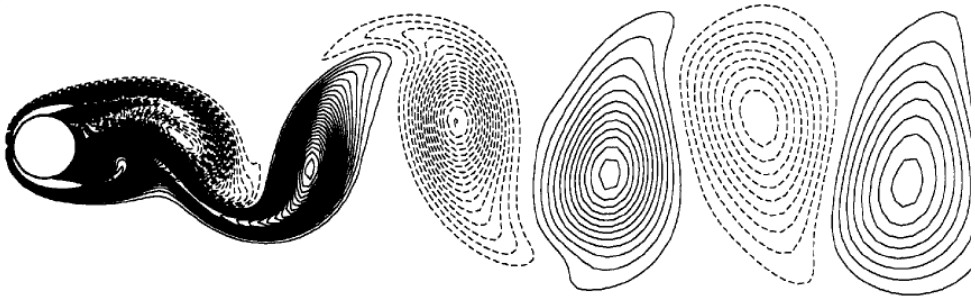

(b) Inoue and Hatakeyama [2002].

Figure 3.10 Non-dimensional instantaneous vorticity $\tilde{\omega}$ in the cylinder wake (contours between -1 et 1).

Table 3.3 Aerodynamic results.

	St	C_D	c'_D	c'_L
Turb'Flow (all configs.)	0.182	1.33	0.024	0.51
PowerFLOW	0.183	1.34	0.025	0.52
Inoue and Hatakeyama [2002]	0.183	1.39	0.026	0.53
Lafitte and Pérot [2009]	0.185	1.39	0.028	0.56

3.5.4 Acoustic results

The noise radiated by a flow past a cylinder is generated by two acoustic sources. The first one is the dipolar radiation induced by the presence of the cylinder wall in the fluid. The second one is the quadrupolar source due to the turbulent structures in the flow. Given the low Mach and Reynolds numbers chosen for this study (Table 3.1), the quadrupolar component is dominated by the dipolar noise [Curle, 1955]. Additionally, the present thesis is focused on the tonal noise prediction. Therefore, the noise predictions only accounted for the dipolar radiation and the validation was based on the amplitude of the non-dimensional acoustic pressure fluctuations $\widetilde{P'}$ which is given by

$$\widetilde{P'} = \frac{P'_{max} - P'_{min}}{0.5\ \rho_\infty c_\infty^2}, \tag{3.50}$$

where P' is the acoustic pressure fluctuation and ρ_∞ the mean density. The evolution of $\widetilde{P'}$ as a function of the radial distance was observed in the direction normal to the flow where the radiation is maximal ($\theta = \pi/2$, where θ is the polar angle relative to the downstream direction).

Influence of the spatial scheme

The influence of the *Turb'Flow* spatial schemes was studied on the circular mesh which contains a large cell size ratio in the damping zone. Since this type of coarsening is often found in real fan meshes, this mesh appeared to be a good way to study the behavior of the spatial schemes. The decay of $\widetilde{P'}$ is presented in Figure 3.11 for four configurations: Liou AUSM+ 2$^{\text{nd}}$ order, Jameson 2$^{\text{nd}}$ order, Jameson 4$^{\text{th}}$ order, and Jameson 2$^{\text{nd}}$ order with a 2$^{\text{nd}}$ order in the damping zone.

As expected from a two-dimensional dipolar radiation, the decay is proportional to $1/\sqrt{r}$, which is typical of a cylindrical acoustic propagation. With this particular mesh, the Jameson 2$^{\text{nd}}$ order appears to be the closest to a $1/\sqrt{r}$-decay from 10 to 100 D. An influence of the damping zone is clearly visible beyond 40 D with the three other configurations (Liou AUSM+ 2$^{\text{nd}}$ order, Jameson 4$^{\text{th}}$ order, and Jameson 2$^{\text{nd}}$ order with a 2$^{\text{nd}}$ order in the damping zone), which leads to an overprediction of $\widetilde{P'}$. Therefore, the scheme of Jameson 2$^{\text{nd}}$ order correctly propagates the acoustic waves and yields a correct decay even with a rapid coarsening in the damping zone. For this reason, the results presented in the following chapters were obtained from simulations with this spatial scheme.

Influence of the spatial discretization

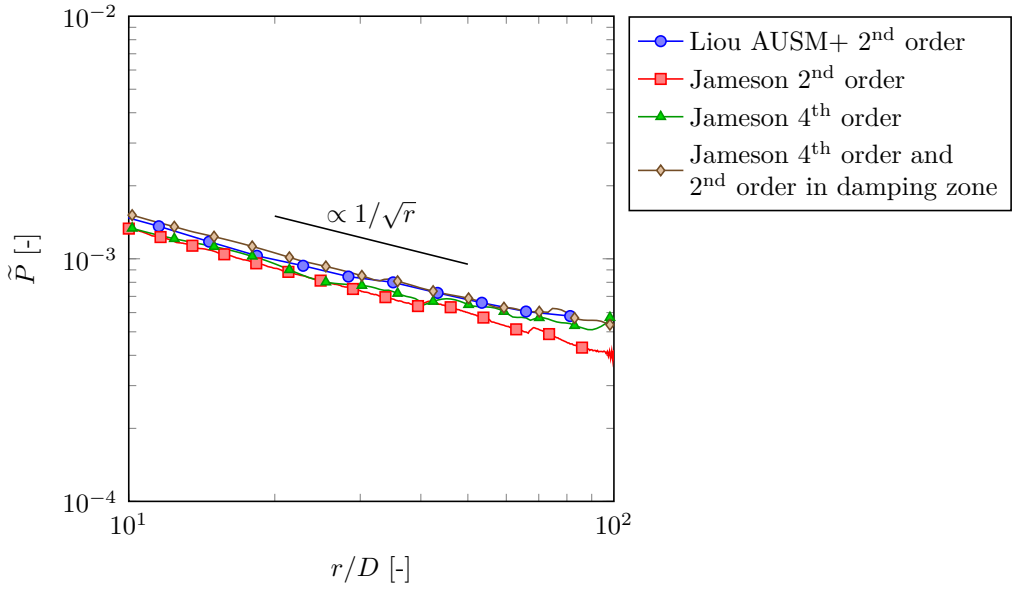

Figure 3.11 Influence of the *Turb'Flow* spatial scheme on the decay of the non-dimensional acoustic pressure fluctuations $\widetilde{P'}$ ($\theta = \pi/2$; circular mesh; direct acoustic propagation).

The constant cell size ratio used in the octagonal mesh is a good test-case to evaluate the minimal spatial discretization which allows the acoustic wave to propagate correctly. As observed in Figure 3.12, the dissipation of the acoustic wave with the octagonal mesh occurs from a 50-D distance. At this radial position, the mesh refinement corresponds to 10 points per acoustic wavelength λ_0, which is in agreement with Soulat's study on *Turb'Flow* spatial schemes [Soulat, 2010].

Comparison of direct propagation and acoustic analogies

As stated in Section 3.4, the noise prediction in the far field may be computed from two different methods: a direct propagation of the acoustic waves using a compressible solver, or the propagation of the near-field sources using an acoustic analogy. Since the *Turb'Flow* and PowerFLOW simulations are computed in 2D, the direct propagation can only be compared to acoustic analogies which are based on the 2D Green's function. In the present study, a 2D Curle analogy in the frequency domain was implemented to propagate the acoustic sources located on the cylinder surface which were recorded in the *Turb'Flow* simulation with a circular mesh. As observed in Figure 3.12, the decay of $\widetilde{P}$ is very well captured, and the result is in very good agreement with the direct acoustic radiation predicted by the codes *Turb'Flow* and *PowerFLOW*.

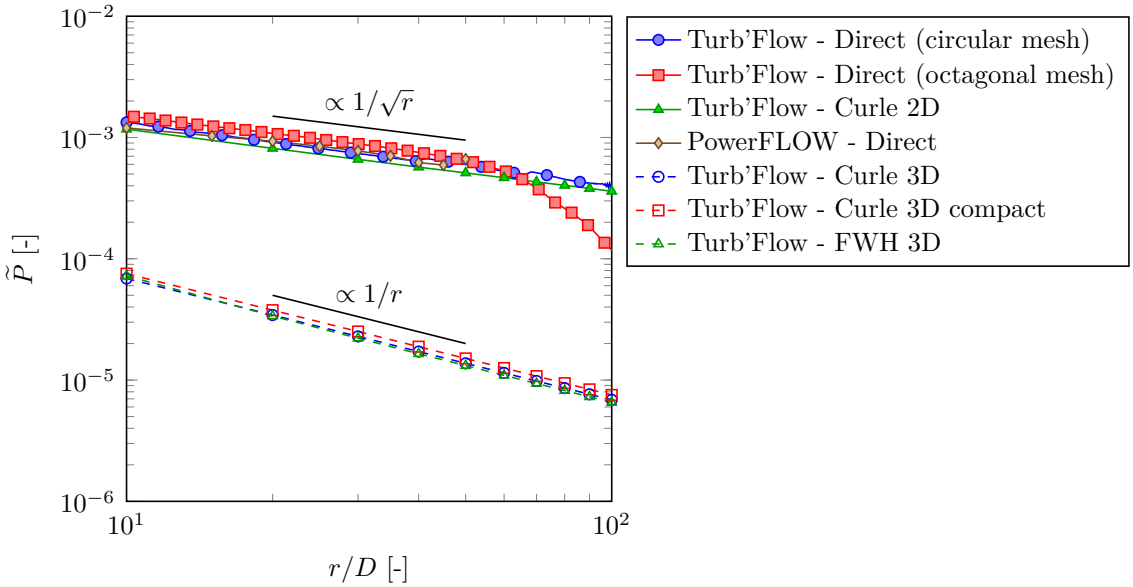

Figure 3.12 Decay of the non-dimensional acoustic pressure fluctuations ($\theta = \pi/2$).

In a fan simulation, the direct propagation of the acoustic sources would require a very fine and very large simulation domain, which would result in an impractically-large computation cost. The present aeroacoustic simulation of the flow past a cylinder is thus used to validate the code *FoxWHawk* which will be used to propagate the acoustic sources located on the fan. This code, developed by Casalino [2003], uses the conversion of Brentner and Farassat's retarded-time formulation [Brentner and Farassat, 1998] into a forward-time formulation of the FW-H equation proposed by Difrancescantonio [1997]. Since this formulation is based on the 3D Green's function, the acoustic decay is proportional to $1/r$ which is typical of a spherical acoustic propagation; hence the results cannot be directly compared with the 2D direct acoustic propagation. Therefore, for the purpose of validating the *FoxWHawk* prediction, two Curle's analogies based on the 3D Green's function were coded in the time domain. One formulation is based on the pressure fluctuations at the cylinder surface whereas the second one is a compact formulation based on the lift and drag fluctuations. The *Turb'Flow* results with a circular mesh were used to feed the three acoustic analogies.

As presented in Figure 3.12, the three codes are in very good agreement. The non-compact formulations (FW-H and Curle 3D) show a less than 1-% difference, which validates the *FoxWHawk* acoustic prediction for a static source.

3.6 Conclusion

In this chapter, the numerical methods for aeroacoustic simulations were presented. The acoustic sources are first computed from aerodynamic simulation. With compressible codes, these sources can be directly propagated in the flow, which requires very fine and large simulation domains. Since the computational cost associated with a direct propagation remains too high for Navier-Stokes solvers, acoustic analogies are often used to propagate the sources in the far field.

To validate the aerodynamic and acoustic methods used in the present thesis, an acoustic prediction of the flow past a cylinder was performed. With a Reynolds number of 150, the regime was unsteady and laminar, which led to the development of a vortex shedding downstream of the cylinder. Two different approaches were tested: the Navier-Stokes solver *Turb'Flow* and the LBM solver *PowerFLOW*. The aerodynamic predictions were in excellent agreement with the literature, and a more detailed study was conducted on the sound radiated by the cylinder. Several *Turb'Flow* simulations were performed to highlight the influence of the spatial discretization and the spatial scheme on the direct sound propagation. Among the four tested configurations, the 2^{nd}-order Jameson scheme yielded the best prediction of the acoustic decay; hence this scheme is used in the following chapters of this thesis. Additionally, the wall-pressure fluctuations at the cylinder surface were recorded to feed four different acoustic codes: a 2D Curle's analogy in the frequency domain, a 3D Curle's analogy in the time domain and its compact formulation, and a 3D FW-H analogy (*FoxWHawk*). All the acoustic predictions were in very good agreement, which validated the tools used to predict the tonal noise radiation of low-speed fans.

CHAPTER 4

ROTOR SIMULATIONS IN UNIFORM INLET FLOW

THE previous chapter presented numerical methods for aeroacoustic prediction. As a first step to simulate the interaction between an obstruction and a fan, the aeroacoustic prediction of a single rotor in a typical fan test configuration was performed to compute its acoustic signature – the fan primary noise. In particular, this numerical study aimed at establishing the potential contribution of the tip clearance to tonal noise, free of any upstream or downstream distortion. To the best of authors' knowledge, the precise aeroacoustic mechanisms responsible for this noise had not yet been studied in this particular configuration.

Unsteady RANS simulations were carried out to feed two acoustic models in order to propagate the noise sources in the far field. The numerical configuration and the aerodynamic results are discussed in Section 4.1, whereas the acoustic models and the noise prediction are presented in Section 4.2.

This chapter is in most part based on an article accepted for publication in the Journal of the Acoustical Society of America and entitled *Subharmonic tonal noise from backflow vortices radiated by a low-speed ring fan in uniform inlet flow* [Magne *et al.*, 2015].

4.1 Aerodynamic simulations

4.1.1 Numerical configuration

A typical axial automotive cooling fan was chosen for all the aeroacoustic simulations presented in this thesis. This choice was made based on the extensive studies conducted on this particular fan in the last 15 years.

As seen in Figure 4.1, the fan features 9 blades connected by an L-shaped rotating ring and a short hub. It is a well-documented machine on which both experimental and numerical data exist [Caro and Moreau, 2000; Coggiola *et al.*, 1998; Foss *et al.*, 2001; Moreau and Bakir, 2003, 2004; Moreau and Bennett, 1997; Moreau and Roger, 2007; Moreau *et al.*, 2011; Pérot *et al.*, 2010b; Roger *et al.*, 2006]. The literature aerodynamic data were obtained

at the fan design condition (2500 rpm; 2500 m^3/h). However, the torque-meter noise did not allow the acoustic measurements at the same rotational speed. Consequently, the acoustic data found in the literature were recorded at 2000 rpm, and three flow rates were tested: 2000, 1542, and 924 m^3/h. It should be noted that the operating point (2000 rpm; 2000 m^3/h) is self-similar to the design condition (2500 rpm; 2500 m^3/h) according to fan laws. To validate the numerical data, four simulations were therefore performed at the aforementioned operating points (three at 2000 rpm and one at 2500 rpm).

The 380 mm outer diameter implies typical Mach numbers up to 0.15 at the blade tip (low-subsonic), with a Reynolds number based on the chord of about 1.5×10^5 at midspan (transition regime). With this Reynolds number, the small turbulence scales could not be directly solved at a reasonable computational cost. An unsteady RANS method was thus chosen to model all turbulence eddies.

In the numerical configuration, the rotor was flush-mounted on a plenum wall and no upstream or downstream distortions were present. This setup allowed a comparison with the aerodynamic and acoustic experiments [Foss *et al.*, 2001; Moreau and Roger, 2007; Moreau *et al.*, 2011], in which the rotor was supported by a long shaft and no stator was present.

In order to reduce the computational cost, only one blade passage was meshed; therefore a uniform circumferential blade distribution was assumed. The multi-block structured mesh was generated with *Gridgen* 15.17 [Pointwise, 2010] for a total of 5.2 million nodes using the same grid distribution that was shown to yield proper wall resolution of the boundary layers with *ANSYS CFX* 12 [Moreau *et al.*, 2011]. The blade was meshed with 85 nodes along the spanwise direction and 285 nodes around the profile (Figure 4.2). The tip clearance contained 17 nodes in the radial direction. The dimensionless wall distance

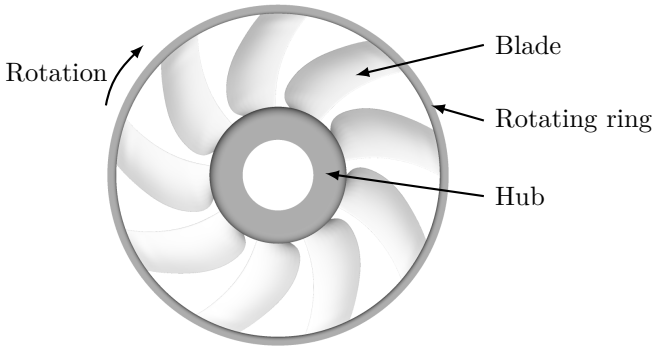

Figure 4.1 Rotor geometry.

based on the turbulent shear stress, y^+, was mostly around 1-2 and kept under 6.5 on the whole rotor surface.

Since this fan had been previously studied with the LBM code *PowerFLOW* [Pérot *et al.*, 2010b], the flow passing through the fan was solved with *Turb'Flow* using an unsteady compressible RANS method [LMFA, 2010]. The turbulence modeling was ensured by a TNT Kok $k-\omega$ model [Kok, 2000] with a turbulent kinetic energy limiter to prevent unphysical high production at stagnation points. The discretization of the equations was performed by the spatial, second-order, centered scheme of Jameson which showed the best performance on the test-case validation (see Section 3.5). The temporal discretization was ensured by a Runge-Kutta scheme with five steps. As shown in Figure 4.3, the flow rate was *uniformly imposed* at the inlet of the domain on a spherical plenum. Downstream, a porous medium was set with a large axial permeability and a low transverse permeability. As a result, the recirculations downstream of the fan were straightened, which ensured a clean, axial flow at the outlet, where the pressure was imposed with a radial equilibrium. In order to enhance the numerical accuracy, the entire simulation domain was solved in the rotating frame of the rotor, taking into account the Coriolis and inertia terms. Additionally, this configuration avoided interfaces between fixed and moving domains, which ruled out all interpolation errors.

The initial aerodynamic field was generated analytically with a uniform field, and then a *steady* RANS simulation was carried out in order to reduce the convergence duration. Once the aerodynamic field was established, a constant and global time step was set to achieve the *unsteady* simulation. A preliminary time convergence study showed that the stability of the temporal scheme was maintained with 30 000 iterations per blade passage period, leading to a time step of 8.9×10^{-8} s and a maximum Courant-–Friedrichs-–Lewy (CFL) condition of 3.

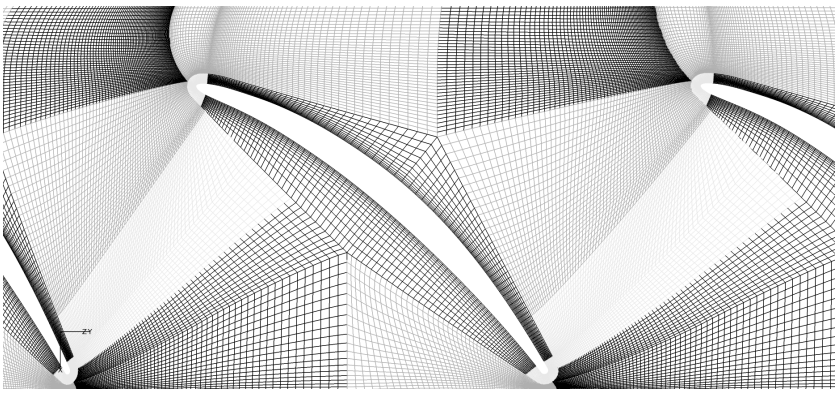

Figure 4.2 Mesh around the blade showing the multi-block topology.

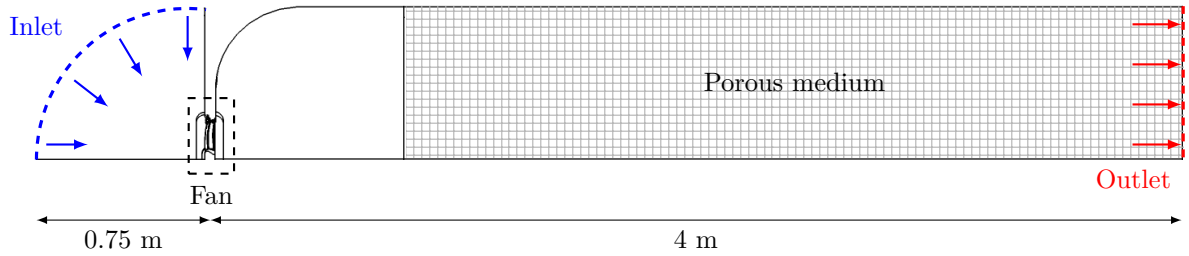

Figure 4.3 Complete simulation domain with boundary conditions.

The simulations were performed on the Mammoth Series II cluster on 31 cores, leading to 5.03 CPU-years per fan revolution (cluster technical specifications are reported in Appendix B). In comparison, only 16.7 CPU-days per fan revolution were required by the *PowerFLOW* solver [Pérot *et al.*, 2010b].

4.1.2 Aerodynamic results

The aerodynamic results were compared with previous simulations [Moreau *et al.*, 2011; Pérot *et al.*, 2010b] and experimental data [Foss *et al.*, 2001] performed at 2500 rpm and 2500 m^3/h.

Convergence

The aerodynamic convergence was checked by monitoring the pressure rise, the flow rate on different surfaces along the simulation domain, and the integrated force on the blade. This strategy had been previously used successfully in cascades [Henner *et al.*, 2000] and similar cooling fan systems [Buisson *et al.*, 2013; Moreau and Roger, 2007; Soulat *et al.*, 2013a].

The convergence of the simulation at 2500 rpm and 2500 m^3/h is presented in Figure 4.4. The mean value of the three quantities is converged after 5.5 fan revolutions. The small oscillations observed after the transient period are the result of the blade rotation on the surrounding flow field. The polar plot (Figure 4.4d) confirms that the differences between the cycles remain very small (notice the axis scales). Consequently, the aerodynamic and acoustic results presented in the following sections were processed from data recorded after the convergence. The same approach was also used for the three simulations at 2000 rpm.

Fan performance

The validation of the fan performances was based on the static pressure rise across the rotor and the torque applied on the fan. In the present work, the pressure rise was extracted between two planes which were 3 chords away from the rotor plane in the upstream and downstream directions. In Figure 4.5a, the result shows a very good agreement with

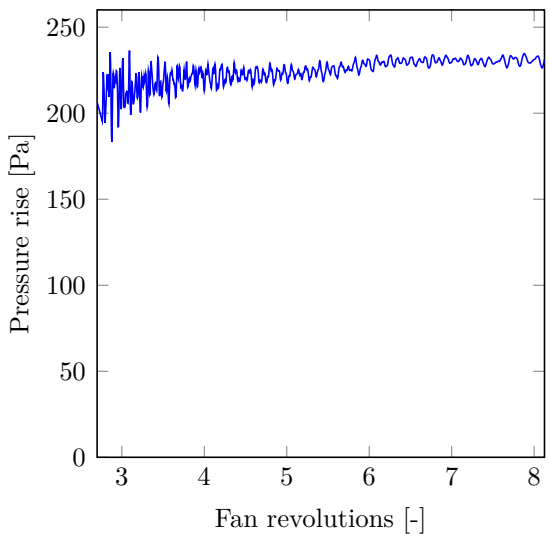

(a) Pressure rise across the fan.

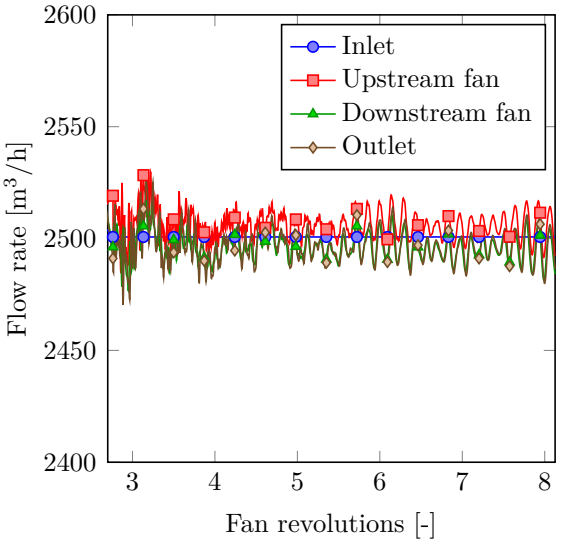

(b) Flow rate.

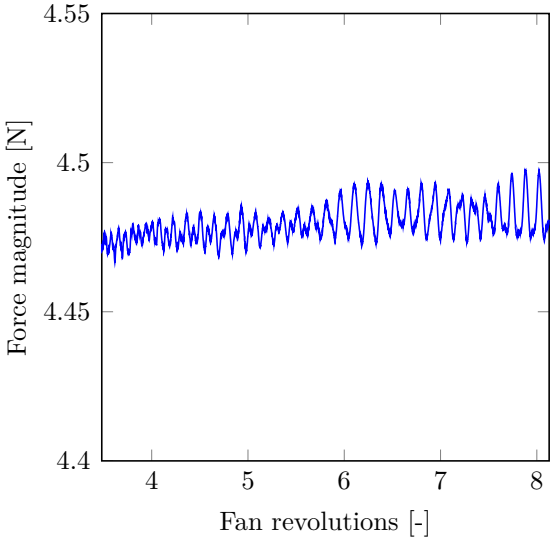

(c) Magnitude of the force applied on the blade surface.

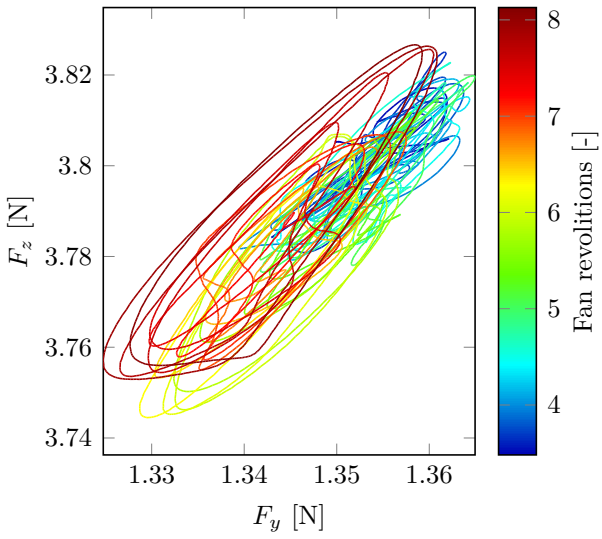

(d) Polar plot of the force applied on the blade surface.

Figure 4.4 Simulation convergence (2500 rpm; 2500 m^3/h).

existing experimental data and other numerical simulations [Foss *et al.*, 2001; Moreau *et al.*, 2011; Pérot *et al.*, 2010b]. The measurements are plotted as upper and lower bounds that account for the molding and prototyping variability. At this operating point, a significant improvement is achieved in comparison with the previously reported steady results (CFX RANS) on coarser grids (less than 1 million points) [Foss *et al.*, 2001]. Similarly, the prediction of torque applied on the rotor surfaces is in good agreement with the experiment (Figure 4.5b).

Flow topology

The meridional view of the axial velocity is presented in Figure 4.6. As observed close to the ring section, the pressure rise across the fan induces a flow recirculation in the tip clearance. This secondary flow interacts with the blade leading-edge and generates an unsteady load on the fan surfaces. As observed previously [Moreau *et al.*, 2011], the dominant flow unsteadiness occurs in this region. In Figures 4.7a and 4.7b, the nature of the flow at the design condition is very well highlighted by the iso-surface of the Q-factor defined as:

$$Q = -\frac{1}{2}\left[\left(\frac{\partial U_1}{\partial x_1}\right)^2 + \left(\frac{\partial U_2}{\partial x_2}\right)^2 + \left(\frac{\partial U_3}{\partial x_3}\right)^2\right] - \frac{\partial U_1}{\partial x_2}\frac{\partial U_2}{\partial x_1} - \frac{\partial U_1}{\partial x_3}\frac{\partial U_3}{\partial x_1} - \frac{\partial U_3}{\partial x_2}\frac{\partial U_2}{\partial x_3} \qquad (4.1)$$

Coherent vortices come from the rotating ring and impinge the blades in the upper section, which confirms the previous statement. At lower flow rates (Figures 4.7c and 4.7d), the backflow vortices are much larger and they go further upstream. This is the consequence of a larger pressure rise across the fan. Since only one blade passage was simulated, a flow confinement likely affects the validity of the URANS simulations at these lower flow rates.

In the present configuration, the small tip clearance, the stationary shroud wall, and the L-shaped labyrinth of the ring creates a strong resistance to the flow and, therefore, reduce the velocity of the backflow. Consequently, the velocity (including its tangential component) is reduced between the downstream and the upstream flow. In the simulation at the design condition (2500 rpm; 2500 m^3/h), the backflow angular velocity was estimated to be 580 rpm. This speed difference implies that each blade impacts a vortex structure at the frequency $H_1 = B\,\Omega_r = 288$ Hz, where $B = 9$ is the number of blades and $\Omega_r = (2500 - 580)/60 = 32\ s^{-1}$ is the relative angular velocity between the vortices and the rotor. As one can expect, the main acoustic radiation should occur at this frequency H_1 and its harmonics H_2, H_3, ...

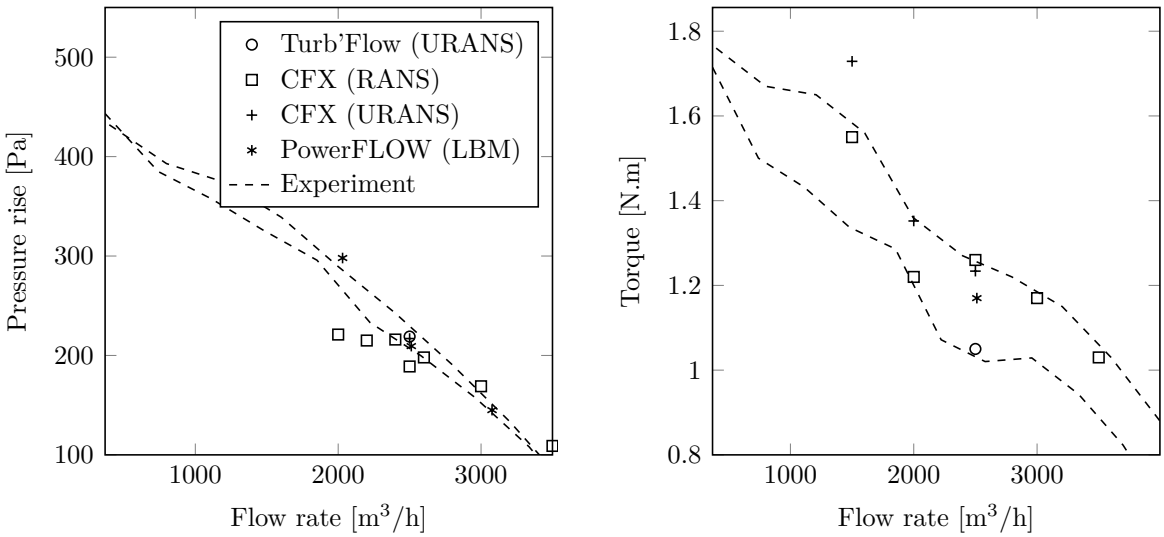

(a) Pressure rise across the fan (b) Torque applied on the rotor

Figure 4.5 Monitoring of the fan performance.

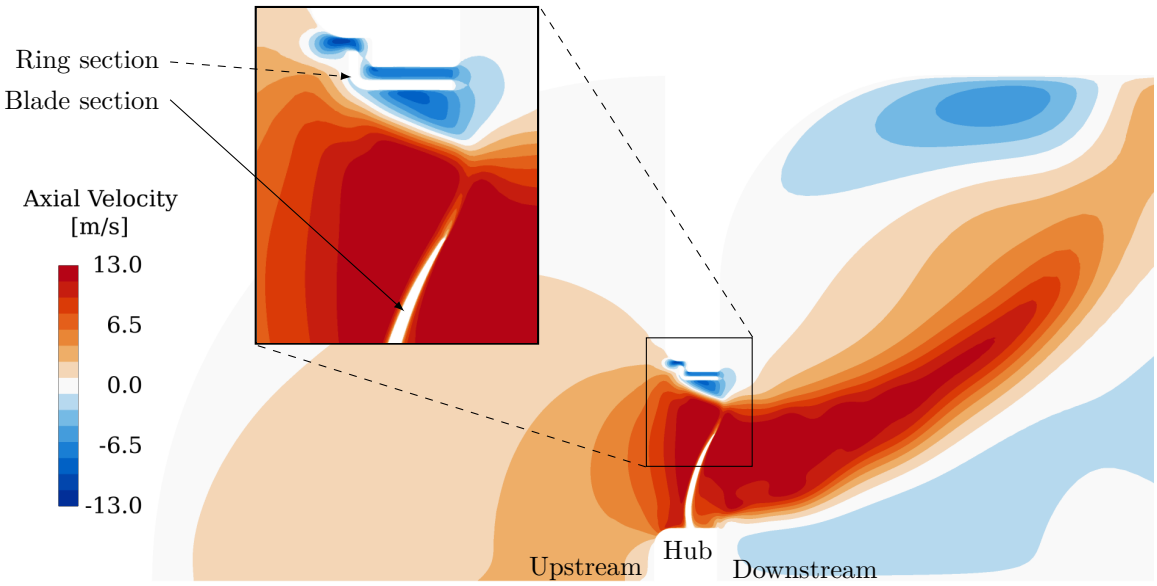

Figure 4.6 Axial velocity field at constant angular position (2500 rpm; 2500 m^3/h).

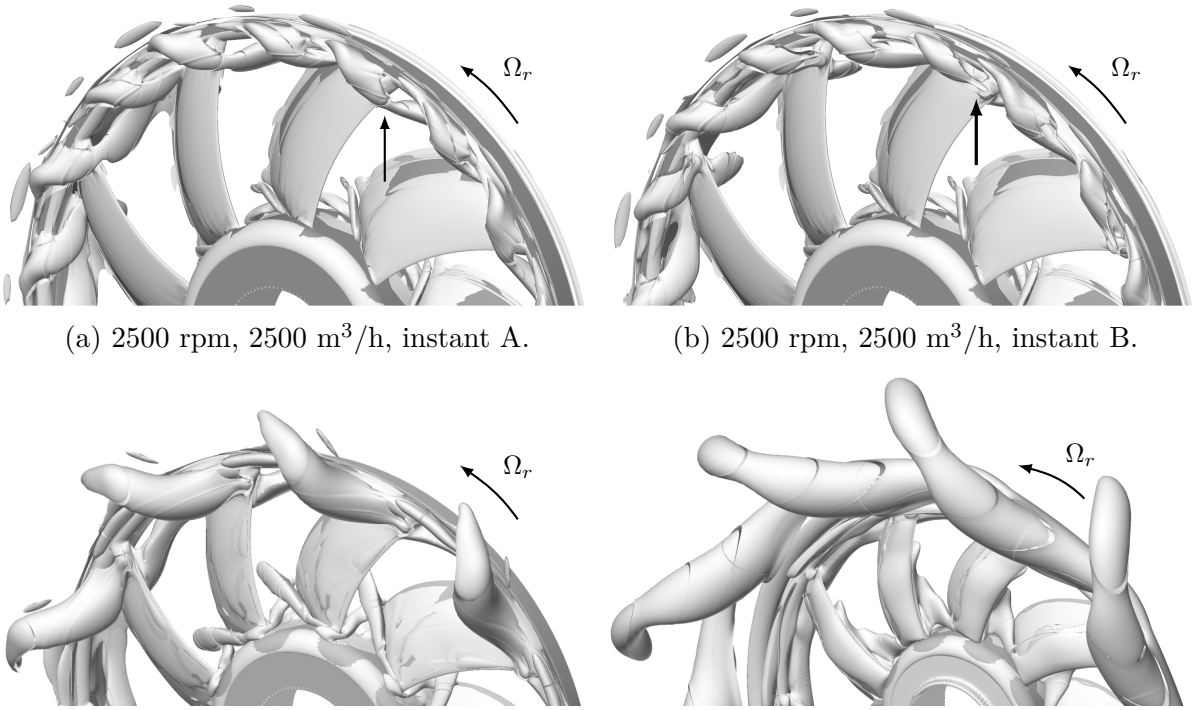

(a) 2500 rpm, 2500 m^3/h, instant A.

(b) 2500 rpm, 2500 m^3/h, instant B.

(c) 2000 rpm, 1542 m^3/h.

(d) 2000 rpm, 924 m^3/h.

Figure 4.7 Iso-surface of the Q-factor in the rotor frame of reference on the suction side of the fan (upstream). Ω_r is the relative velocity between the fan and the backflow vortices.

Wake analysis

For the purpose of validating the aerodynamic simulation in detail, the *Turb'Flow* results were compared to data found in the literature: hot-wire measurements performed at Michigan State University [Foss *et al.*, 2001], *ANSYS CFX* RANS simulation [Foss *et al.*, 2001; Moreau *et al.*, 2011], and *PowerFLOW* LBM simulation [Pérot *et al.*, 2010b].

Figure 4.8 presents the three components of the phase-averaged velocity (in the absolute frame of reference) extracted in a plane 33 mm downstream of the trailing edge. *Turb'Flow* aerodynamic results are in excellent agreement with the experiments. In particular, the prediction of the radial velocity is noticeably improved compared with the *ANSYS CFX* RANS simulation, and it shows a better prediction than the *PowerFLOW* solver. However, a small discrepancy is observed on the tangential velocity. This component is overestimated at the blade tip, which is likely caused by the differences between the experimental and numerical configurations. The experimental setup employed a fan flushed-mounted on a wall, whereas a rounded outlet domain with a limited diameter was used in the *Turb'Flow* simulations (see Figure 4.3). This led to a dissimilarity of the recirculation developed downstream of the fan (visible in blue in the upper-right area of Figure 4.6) which is presumably longer in the computation. Since the *PowerFLOW* simulation domain is similar to the experimental setup, this conjecture agrees with the smaller tangential velocity found near the ring in the *PowerFLOW* results. However, it should be noted that tuft visualizations close to the ring showed high levels of unsteadiness in the experiments [Foss *et al.*, 2001]. It was thus more difficult to align the hot wire with the flow, which caused larger experimental uncertainties at higher radius.

To further analyze the rotor wake, six azimuthal-averaged flow kinematic variables were compared with the hot-wire measurements and *PowerFLOW* predictions: the three velocity components (in the absolute frame of reference), the velocity magnitude, the turbulent kinetic energy, and the wake angle relative to the rotor axis. Figure 4.9 presents linear plots of those azimuthal-averaged quantities as a function of the radial position.

Overall, the numerical results are coherent with the phase-averaged velocity measurements and show a good agreement with the experiments over most of the blade span. Additionally, the turbulent kinetic energy is well predicted, confirming that the unsteady RANS simulation accurately predicts the velocity fluctuations. Only at the hub and at the tip, differences remain. At the hub, an axial and tangential velocity deficit is observed. This confirms the contribution of radial ribs placed inside the hub in the experimental mock-up. Since the present numerical simulation does not take into account those ribs (the hub

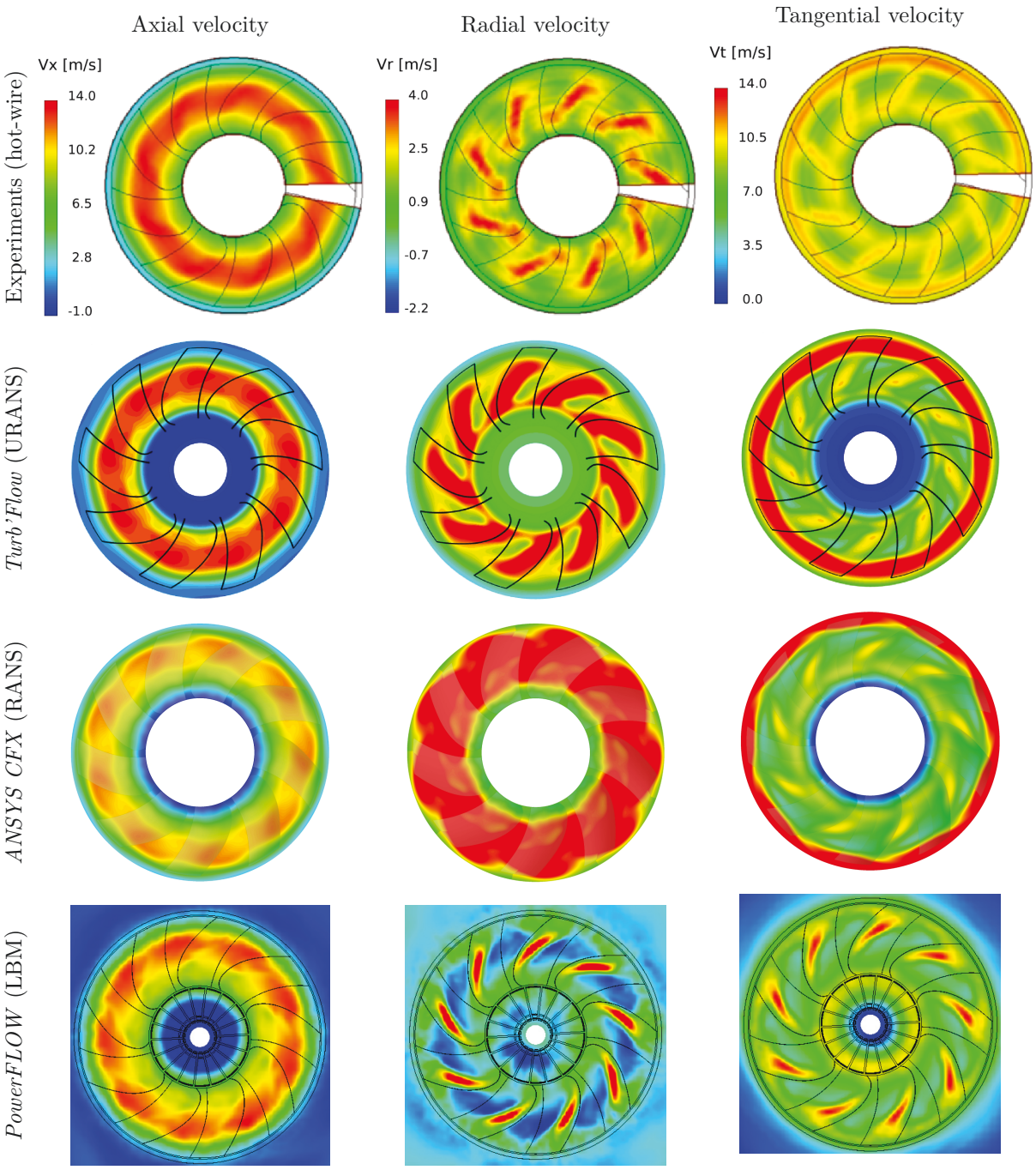

Figure 4.8 Phase-averaged velocity components in a plane 33-mm downstream of the trailing edge.

being filled up), the centrifugal effect induced by the radial ribs is missing in the present work. The higher tangential velocity at very low radius in the *PowerFLOW* simulation confirms this statement. Pérot *et al.* [2010b] illustrated and compared this effect with LDV measurements on a plane of rotation very close to the blade trailing edge. At high radius, the negative values of the wake angle highlight a wake constriction close to the rotor ring. As a result, the axial and radial components of the velocity show lower values than expected and the tangential component is consequently higher to make up for the flow rate. As stated previously, this constriction likely occurs because of the differences between the experimental and numerical setups. In the *PowerFLOW* simulation, the overprediction of the radial component induces a higher wake angle over the all span. It should also be noted that, close to the hub, the very low axial velocity causes a divergence of the wake angle in the two simulations.

Although some slight aerodynamic differences can be observed in the wake, these discrepancies are coherent with the setup geometries. Additionally, the present simulation greatly improves the numerical results reported by Foss *et al.* [2001]. Therefore, the present unsteady aerodynamic simulation can be considered as validated.

4.2 Acoustic predictions

The acoustic prediction in the far field was achieved using two different methods based on the above aerodynamic simulations: a FW-H analogy in the time-domain and a compact rotating dipole formulation in the frequency-domain. The latter is similar to the method used for small computer cooling fans by Huang [2003] and Huang and Wang [2005] who based their formulation on Lowson's work for compressor noise [Lowson, 1970]. The former is related to Lee's work on automotive cooling fans [Lee *et al.*, 2000].

4.2.1 FW-H analogy

The FW-H analogy (see Section 3.4.3) was computed by the code *FoxWHawk*, and an approach similar to previous works on automotive cooling fans was used [Casalino *et al.*, 2010; Moreau *et al.*, 2006a]. The transient static pressure on the rotor surface of a single blade passage (81 808 quadrilateral elements) was imported, and *FoxWHawk* automatically generated the complete rotor configuration before the acoustic integration by taking into account the phase delay between each blade. Given the Mach numbers at the blade tip, the effects of the quadrupole noise were neglected while only the thickness noise

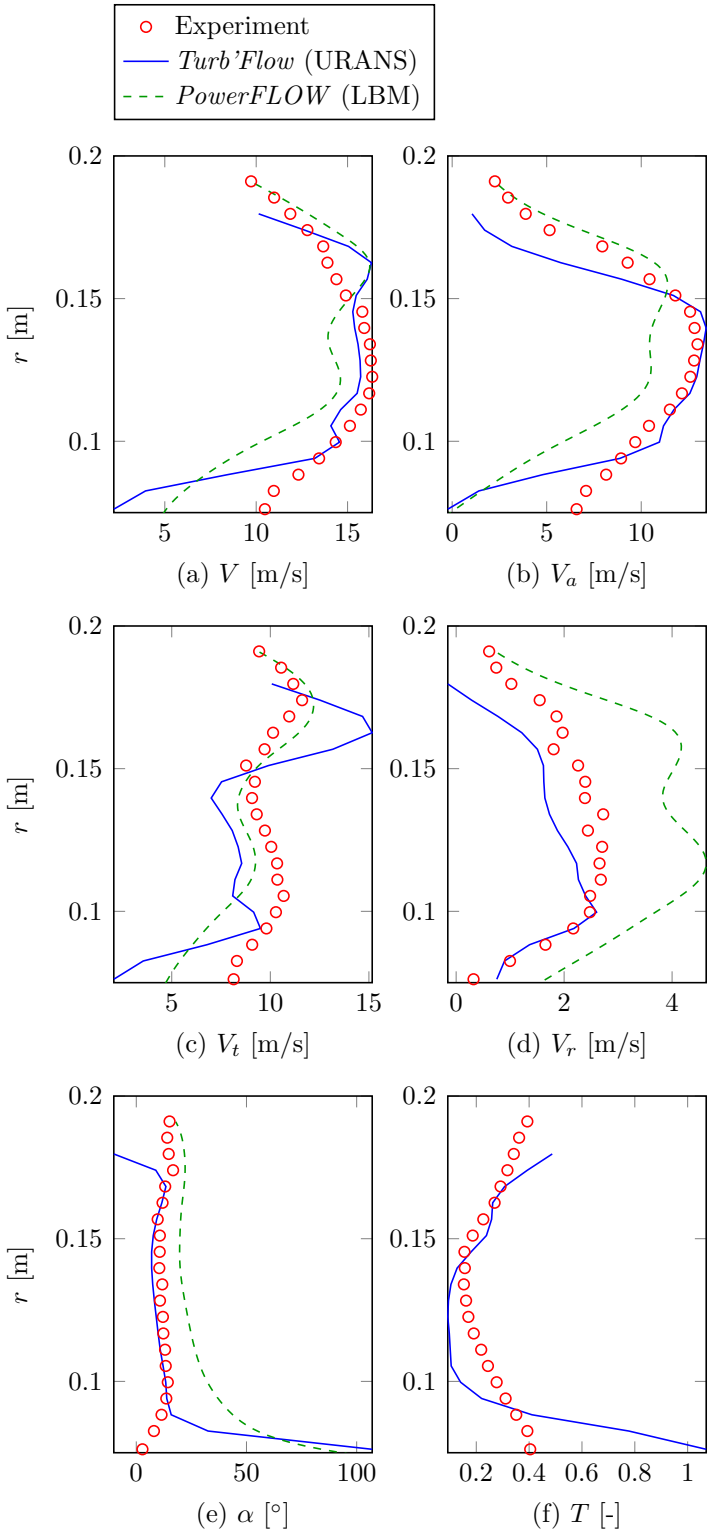

Figure 4.9 Azimuthal-averaged flow kinematic variables in a plane 33 mm downstream of the blade trailing edge: (a) velocity magnitude, (b) axial velocity, (c) tangential velocity, (d) radial velocity, (e) wake angle, (f) turbulent kinetic energy. Simulations at 2500 rpm and 2500 m^3/h.

(monopolar noise, Equation (3.36)) and the loading noise (dipolar noise, Equation (3.40)) were computed.

4.2.2 Compact rotating dipole analogy

The second acoustic prediction method was based on the compact rotating dipole analogy (see Section 3.4.4). This frequency-domain formulation is usually used to predict the radiation at the BPF and its harmonics. However, the present work was focused on the radiation caused by the interaction between the tip-clearance vortices and the blades (see Figure 4.7). For this reason, the angular velocity Ω in Equation (3.47) was replaced by the relative velocity between the rotor and the backflow vortices Ω_r which was estimated from the Q-factor visualizations (Figure 4.7). Consequently, the prediction was made at the frequencies $H_1 = B\,\Omega_r$ and its harmonics.

Figure 4.10 presents the Fourier decomposition of the force components normalized by $\frac{1}{2}\rho_0\,Q^2 S^{-1}$, where Q is the flow rate passing through the fan and S the area between the hub and the blade tip. The force predicted by the unsteady RANS simulation is significant up to the 81^{th} harmonic ($9B$) which corresponds to a frequency of 2592 Hz. Therefore, the sum on s in Equation (3.47) was computed up to this order.

As expected for this type of fan, the axial force shows the highest amplitude of the fluctuations (Figure 4.10). However, the tangential and radial contributions are significant in comparison to other ducted, high-speed fans [De Laborderie *et al.*, 2014]. The latter is mainly caused by a radial equilibrium issue inherent to the design of this particular large-span rotor, whereas the former is the consequence of the blade sweep (lean in high-speed turbomachinery).

4.2.3 Acoustic results

The acoustic pressure fluctuations were computed at 26 virtual microphone positions (observers) equally distributed on a sphere, 1 m away from the rotor center. Given the wavelength at the expected tone (288 Hz) or the blade passing frequency (375 Hz), the diffraction on the rotor surfaces could be considered negligible and the fan was assumed to be compact. Additionally, the observer distance was approximately equal to one wavelength for these frequencies; hence the acoustic field at the observer locations could be considered as the far field.

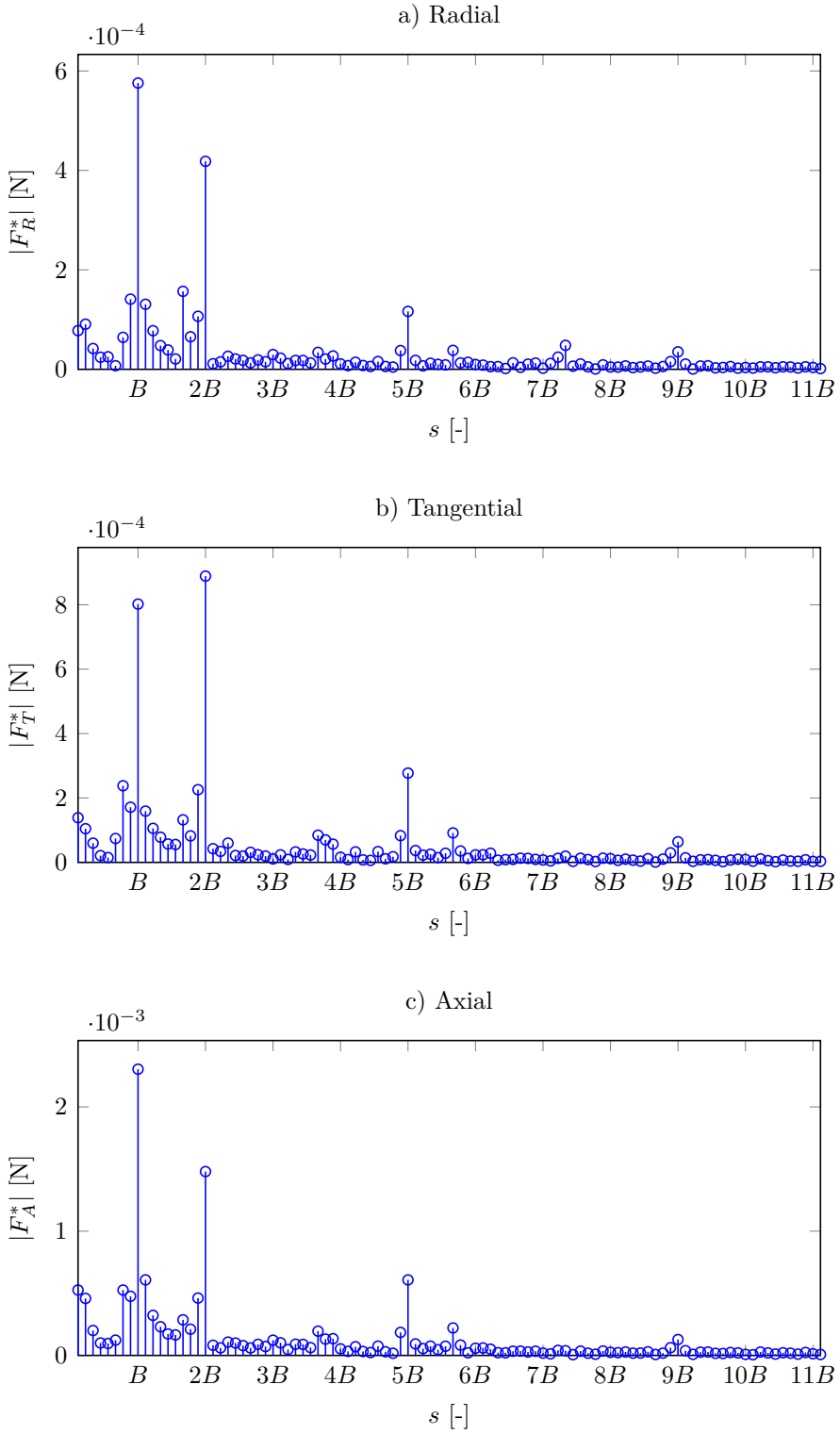

Figure 4.10 Fourier decomposition of the three force components acting on the rotor blade. Simulation at 2500 rpm and 2500 m^3/h.

Once the convergence of the aerodynamic computation was obtained, 20 blade passage periods were recorded to feed both acoustic codes. Although the thickness noise was taken into account in the following FW-H computations, it appeared to be negligible compared with the loading noise, as mentioned by Casalino *et al.* [2010].

Sound power level

From the time pressure signal computed by the FW-H analogy and located on different observers, the acoustic power level is given by:

$$L_{\mathrm{w}} = 10 \log_{10} \left(\frac{\int_S \boldsymbol{I} \cdot \boldsymbol{n} \, \mathrm{d}S}{W_{\mathrm{ref}}} \right), \tag{4.2}$$

where S is an arbitrary closed surface of integration that encloses the source, $\boldsymbol{I}$ the acoustic intensity vector, $\boldsymbol{n}$ the vector normal to S, and W_{ref} the reference acoustic power equal to 10^{-12} W. The acoustic intensity in the far field for an observer i can be approximated by $\hat{p}_i^2 (\rho_0 \, c_0)^{-1}$, where $\hat{p}_i$ is the RMS value of the acoustic pressure at the observer location (still isentropic region away from the fan). For an integration on a sphere of radius r on which N observers are equally distributed, Eq. (4.2) becomes:

$$L_{\mathrm{w}} = 10 \log_{10} \left(\frac{4\pi r^2}{W_{\mathrm{ref}} \, N} \sum_{i=1}^{N} \frac{\hat{p}_i^2}{\rho_0 \, c_0} \right). \tag{4.3}$$

For the design condition (2500 rpm; 2500 m^3/h), the total acoustic power obtained by the FW-H analogy led to a level of 89.2 dB, which was lower than the experimental measurement of 96.2 dB. This different is explained by the fact that only the tonal noise sources are computed by the unsteady RANS simulation. Additionally, the relative large broadband noise radiated by this particular rotor confirms this statement [Moreau *et al.*, 2012].

Sound pressure spectrum

The sound pressure spectrum is presented in Figure 4.11 for two observer locations, one on the rotor axis and the other in the rotor plane. The results of the FW-H analogy confirm the predicted fundamental tone at the frequency of the impact between the tip vortices and the blades (288 Hz). Additionally, the first harmonic (576 Hz) is higher than the fundamental frequency for both observers. This is consistent with the Q-factor visualization (Figure 4.7) in which two coherent vortices are observed per blade passage.

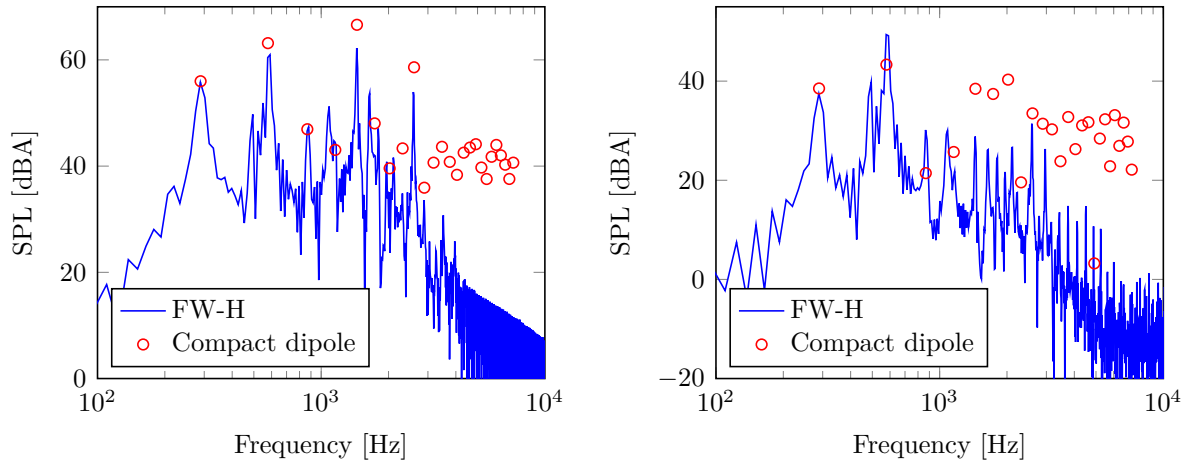

(a) Observer on the rotor axis.

(b) Observer on the rotor plane.

Figure 4.11 Sound pressure spectra computed by the FW-H analogy and the analytical formulation (Eq. (3.47)) of a compact rotating dipole.

The analytical formulation of the compact rotating dipole is in good agreement with the FW-H prediction at lower frequencies. However, the model shows its limits for frequencies above 3000 Hz. Considering that the span dimension of the blades (106 mm) is equal to an acoustic wavelength at 3200 Hz, the compactness of the source is no longer verified for frequencies higher than 3200 Hz and, therefore, an overestimation of the sound pressure level occurs.

Sound power spectra

The sound power spectra computed by both methods is compared with experimental measurements in a reverberant wind tunnel and *PowerFLOW* prediction in Figure 4.12. Since no acoustic data could be recorded at the design condition (2500 rpm; 2500 m^3/h), the numerical prediction at this operating point is compared with the experimental result at 2000 rpm and 2000 m^3/h rescaled according to a dipolar assumption (Figure 4.12a). The computations at 2000 rpm were performed to verify the scaling of the subharmonic tones [Magne *et al.*, 2015].

The unsteady RANS simulation does not resolve small and medium turbulence scales but only large coherent structures; hence only distinct tones are present in the FW-H prediction. This lack of broadband energy throughout the frequency spectrum explains the discrepancy of the total acoustic power level (see Section 4.2.3). *PowerFLOW*, on the other hand, accurately captures the broadband level from 500 Hz as well as the decay in the 1000-2000 Hz range.

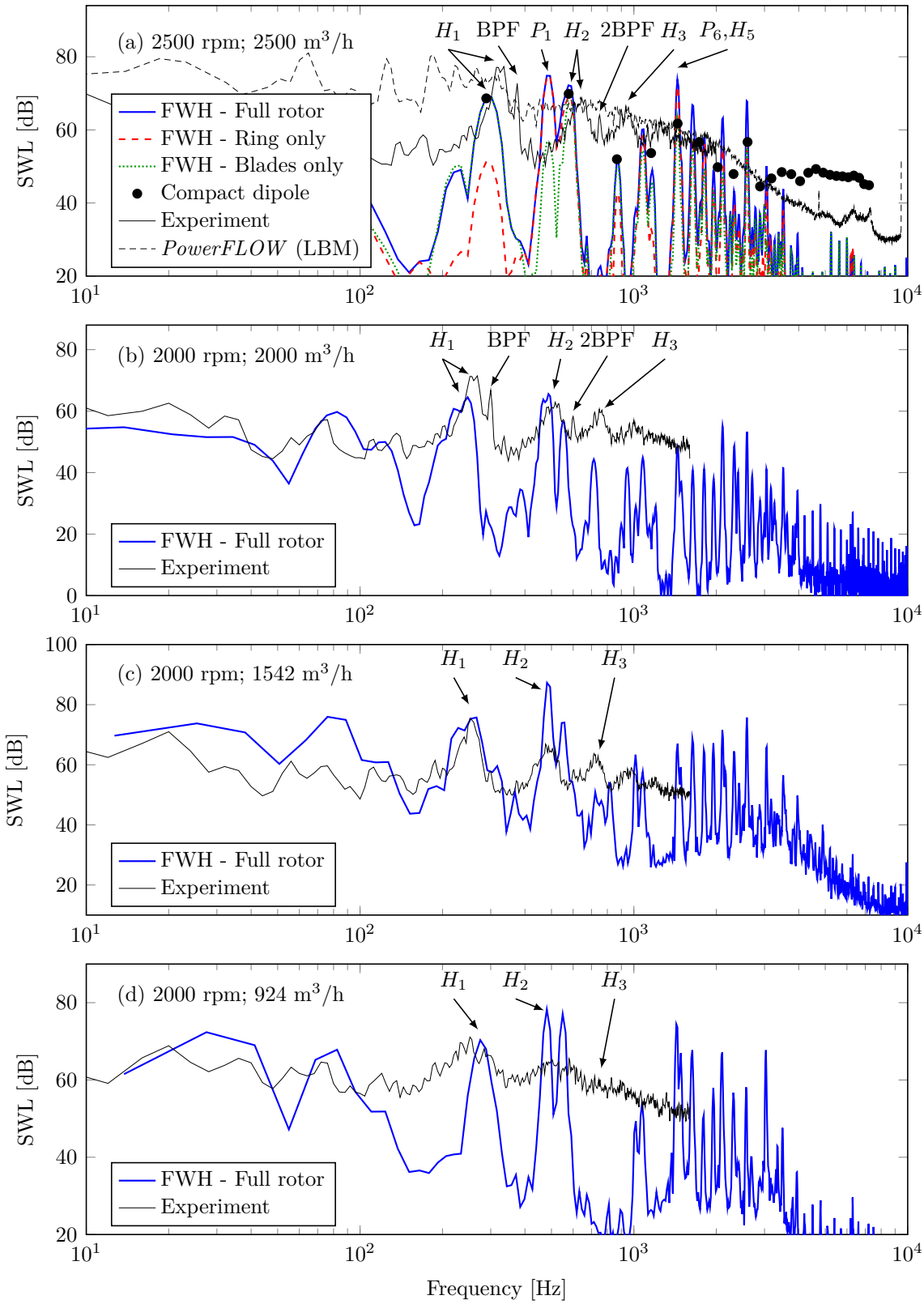

Figure 4.12 Sound power spectra at the computed operating points.

For all the operating points, the aeroacoustic simulations confirm the predominant subharmonic tonal noise radiated at the fundamental frequency H_1 lower than the BPF as observed experimentally. At the design condition (Figures 4.12a and 4.12b)), the BPF most likely appears in the experiment either because the inlet flow was not perfectly uniform [Sturm and Carolus, 2012] or because of a misalignment between the rotor and the casing. This is confirmed by the lack of radiation at the BPF in the other experimental results at lower flow rates (Figures 4.12c and 4.12d). Considering the aerodynamic phenomena leading to a lower angular speed of tip clearance vortices (see Section 4.1.2), the frequencies H_1, H_2, and H_3 strongly depend on the quality of the tip clearance, its geometry, and its surface finishing (rough walls inducing more shear and slower backflow, for instance). This could explain the slight frequency shift observed between the experimental data and the FW-H prediction at the design conditions (Figures 4.12a and 4.12b). However, the positions of the subharmonic humps are in excellent agreement with the experiments for the lower flow rates (Figures 4.12c and 4.12d). Overall, the results confirm that the aeroacoustic phenomena are well captured by the *Turb'Flow* simulations. In the *PowerFLOW* computation (Figure 4.12a), a higher acoustic power is predicted around the subharmonic frequency H_1, but the second and third subharmonic humps do not appear clearly in spectrum. Unpublished work however showed that a finer discretization of the tip clearance could capture the frequencies H_2 and H_3, yielding an excellent agreement with the experiments [Moreau *et al.*, 2015].

As seen in Figures 4.12c and 4.12d, the *Turb'Flow* computations at lower flow rates overpredict the sound power level at the frequency H_2. This is likely the result of the simulations on a single blade passage which could accurately compute the very large flow structures coming from the tip recirculation (see Q-factor visualizations in Figures 4.7c and 4.7d).

At 2500 rpm (Figure 4.12a), a different set of tones appears in the simulation at the frequency $P_1 = 485$ Hz and its harmonics. This contribution is mainly due to sources located on the rotating ring. Besides adding numerous tones in the acoustic signature, this phenomenon is also responsible for a strong tone at 1440 Hz which corresponds to the sixth harmonic P_6 and the harmonic H_5 at the same time.

Wall pressure fluctuations

Figure 4.13 presents the wall pressure fluctuations on the rotor which are filtered around three frequencies of interest for the simulation at the design condition (2500 rpm; 2500 m^3/h). This visualization allows a precise location of the acoustic sources, which is very helpful in

the characterization process of the aeroacoustic phenomena. Also, the filter bandwidth and the level range are kept constant to be able to compare the fluctuation levels between the three frequencies.

In terms of levels, the fluctuations at the frequencies H_1 and P_1 dominate strongly the fluctuations at the BPF. This confirms the perfect axisymmetry and the uniform inlet flow in the simulation. Furthermore, the strongest sources are observed at the fundamental subharmonic tone H_1. They are located at the blade leading edge, in the upper third of the span, where the tip vortices impinge the rotor (see Figure 4.7). These sources appear stronger on the pressure side, mainly due to the angle of attack in the upper section of the blade. As for the acoustic sources at the frequency P_1, they are more evenly distributed on the ring and at the blade tip. Although this tone seems to be related to the tip clearance recirculation, its precise origin is still under investigation. Since the tones P do not appear in the experimental spectrum, they may be inherent to the numerical setup and the turbulence modeling. Additional simulations with a different turbulence model may clarify this point.

4.3 Conclusion

A complete aeroacoustic study of an automotive ring fan in *uniform inlet flow* highlighted the mechanism responsible for subharmonic tonal noise. First, a compressible unsteady RANS simulation provided the aerodynamic flow and the acoustic sources located on the rotor. Secondly, two different methods were used to propagate the sources in the far field: a FW-H analogy in the time-domain and an analytical formulation of a compact rotating dipole in the frequency-domain. The conclusions of the study are:

— The aerodynamic prediction of the fan is significantly improved in comparison to previous works, showing consistent results with both overall and detailed measurements (performance and hot wire measurements). The detailed wake analysis was in good agreement with the *PowerFLOW* results found in the literature.

— The main source of unsteadiness on the rotor is caused by coherent vortices coming from the tip-clearance recirculation and rotating at a lower speed than the rotor. Thus, the periodic pressure fluctuations created on the rotor occur at a different frequency than the BPF, creating subharmonic humps in the acoustic spectrum.

— The unsteady RANS coupled with the FW-H analogy successfully estimated the levels of these subharmonic tonal humps and showed that the acoustic sources located on the blade surface contribute mainly to this noise. This analogy also

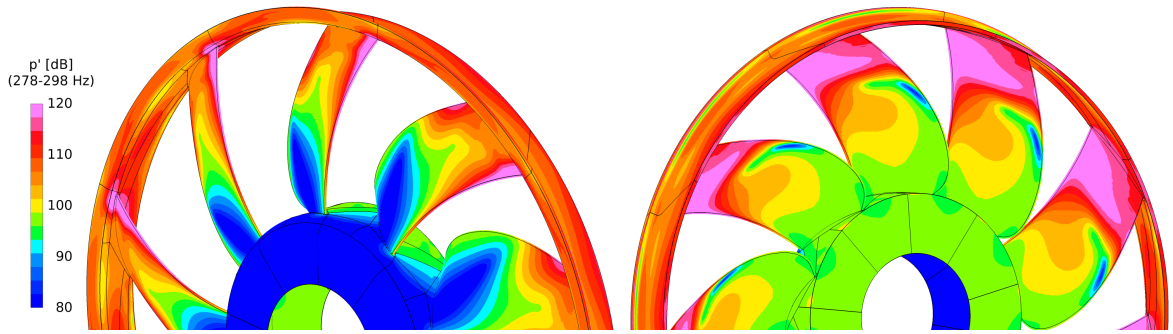

(a) Fundamental subharmonic tone $H_1 = 288$ Hz.

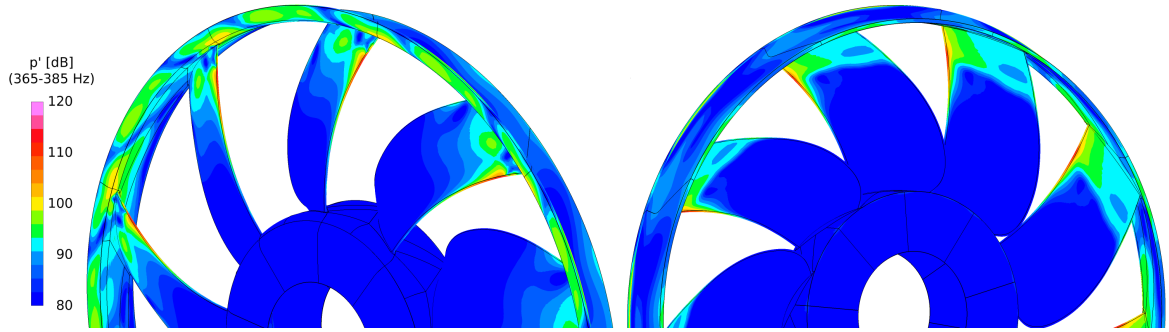

(b) Blade passing frequency BPF = 375 Hz.

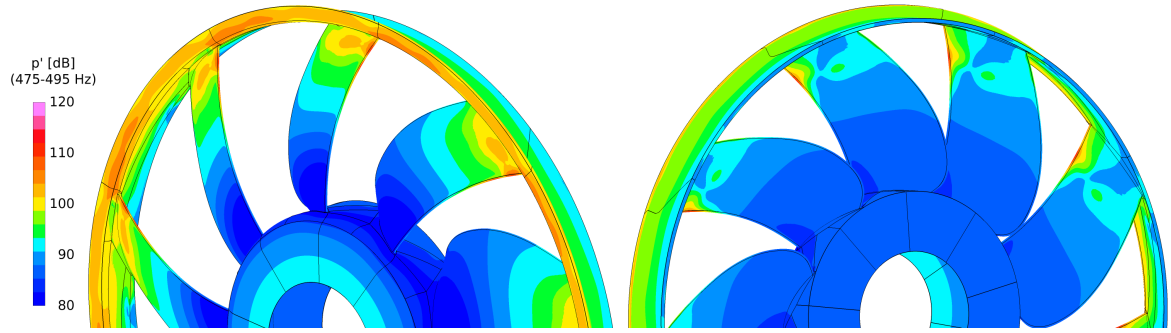

(c) Tone $P_1 = 485$ Hz.

Figure 4.13 Wall pressure fluctuations on the rotor surface filtered with a 20-Hz bandwidth centered on the studied frequency (left: suction side; right: pressure side). Simulation at 2500 rpm and 2500 m^3/h.

stressed that the loading noise strongly dominates the acoustic radiation and that the three force components contribute to the far field noise of this fan.

— The frequency-domain compact dipole model was able to predict quickly the acoustic level at the frequency of the interaction between the tip vortices and the blade, in addition to its first three harmonics. Moreover, the amplitude of these tones can be estimated by an unsteady RANS simulation.

— In this configuration, *PowerFLOW* is significantly faster than *Turb'Flow*.

These findings contribute to a better understanding of the tonal noise radiation of a ring fan free of upstream or downstream distortions. However, the main radiation occurring at a different frequency than the BPF implies that the noise radiated by this fan cannot be controlled by a *static* flow obstruction. Therefore, the present configuration cannot be used to study the obstruction-fan interaction, and a new configuration enhancing the noise at the BPF is presented in the next chapter.

CHAPTER 5

ROTOR-STATOR SIMULATIONS IN UNIFORM INLET FLOW

THE previous chapter showed that an isolated ring fan radiates tonal noise at a different fundamental frequency than the BPF. Since the acoustic control with a static obstruction is not possible in this configuration, the present chapter introduces a different setup which enhances the noise at the BPF and its harmonics. Two different approaches were used to characterize the resulting acoustic signature: the Navier-Stokes solver *Turb'Flow* coupled with a FW-H analogy, and a direct acoustic prediction using the LBM solver *PowerFLOW*. The numerical results were compared to measurements performed in a fully-anechoic room.

The geometry design of the new rotor-stator configuration is presented in Section 5.1. A description of the two numerical setups is then found in Section 5.2, whereas the experimental setup is described in Section 5.3. The aerodynamic and acoustic results are discussed in Sections 5.4 and 5.5, respectively.

5.1 Geometry design

In the previous simulations (see Chapter 4), the 380-mm ring rotor was free of upstream or downstream distortion. In the present configuration, a stator is added 20 mm downstream of the blade trailing edge. This stator, shown in green in Figure 5.1, is designed to increase the noise radiation at the BPF from two mechanisms. First, the vanes are large, 12-mm cylinders and are placed close to the rotor leading edge. Therefore, the potential effect of the stator creates periodic pressure fluctuations on the rotor blades. Second, the vanes are swept to follow the rotor wakes. The impact of the wakes therefore occurs at the same time along the stator, resulting in a coherent source of tonal noise.

The simulations with the rotor alone were performed with the fan flush-mounted on a plenum (see Figure 4.3). In order to perform experimental measurements, this configuration would have required to place the fan between two adjacent rooms. For this reason, it was decided to place the fan in a short duct, which facilitated measurements in the middle of an anechoic room (see Section 6.3 for a complete description of the experimental rig). The

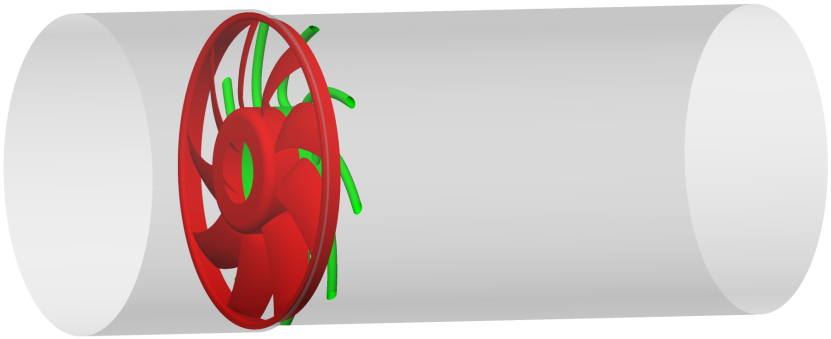

(a) Overview.

(b) Pressure side.

(c) Suction side.

Figure 5.1 Rotor-stator configuration: Rotor in red, stator in green, and duct in grey.

duct is 1.25-m long, and the upstream and downstream portions have different diameters to match the dimensions of the L-shaped tip clearance.

As for the operating point, the rotational speed and flow rate were set at the design condition, 2500 rpm and 2500 m^3/h, respectively.

5.2 Numerical setups

The same two codes were used again to perform the aeroacoustic simulation: *Turb'Flow* [LMFA, 2010], the Navier-Stokes solver used for the isolated rotor computations; and *PowerFLOW* [Exa Corporation, 2012], the LBM solver developed by Exa Corporation.

5.2.1 Turb'Flow simulation

The *Turb'Flow* numerical setup was based on the previous rotor simulations which showed good agreements with experimental measurements (Chapter 4). The multi-block structured mesh was kept identical around the rotor, and the inlet, stator, and downstream sections

were generated using *Gridgen* 15.17 [Pointwise, 2010]. The final mesh contained 7.9 million nodes (50 % more points than for the isolated rotor).

The flow rate was uniformly imposed at the inlet of the duct. Downstream of the stator, a porous medium was set to ensure a positive axial flow at the outlet, where the pressure was imposed with a radial equilibrium. A circumferential Fourier transform was computed by *Turb'Flow* to exchange data at the interfaces between static and rotating blocks.

The discretization of the Navier-Stokes equations was also performed by a second-order spatial centered scheme of Jameson and a Runge-Kutta temporal scheme with five steps. A preliminary time convergence study showed that the stability of the temporal scheme was maintained with 80 000 iterations per blade passing period, leading to a time step of 3.3×10^{-8} s.

To predict the acoustic radiation, the wall pressure fluctuations on the rotor and the stator were recorded as input to the FW-H code *FoxWHawk*. Similarly to the rotor computations, the acoustic sources were propagated to 26 observers equally distributed on a 1-m-radius sphere. It should be noted that the propagation is a free-field formulation. Thus, reflection and diffraction of the acoustic waves on the duct surfaces are not taken into account.

5.2.2 PowerFLOW simulation

The LBM simulation was performed using *PowerFLOW* 4.4b. The setup was built following the *PowerFLOW* guidelines for external aeroacoustic simulations. As shown in Figure 5.2a, the fan is centered in a large, 44-m long, cubic fluid domain. The inlet of the duct features a large bellmouth which limits the development of large upstream structures. This yielded a velocity profile at the fan inlet which was similar to the *Turb'Flow* simulation, but with thicker boundary layers (see Figure 5.3).

As in an experimental test, only the fan rotational speed was imposed to achieve the given operating point. The pressure rise and the flow rate resulted from the losses in the system which were computed by the solver. Three different configurations were tested to control the pressure loss at the duct outlet. Two simulations considered a conical plug at the duct outlet with two different grid refinements (Figure 5.2b), and a third simulation considered an outlet porous medium (Figure 5.2c). The differences between the three simulations demonstrated: 1) the simulation convergence; 2) the mesh convergence with the plug; and 3) the influence of the operating-point control device (conical plug or porous medium). Additionally, preliminary computations (not presented here) were performed to adjust the

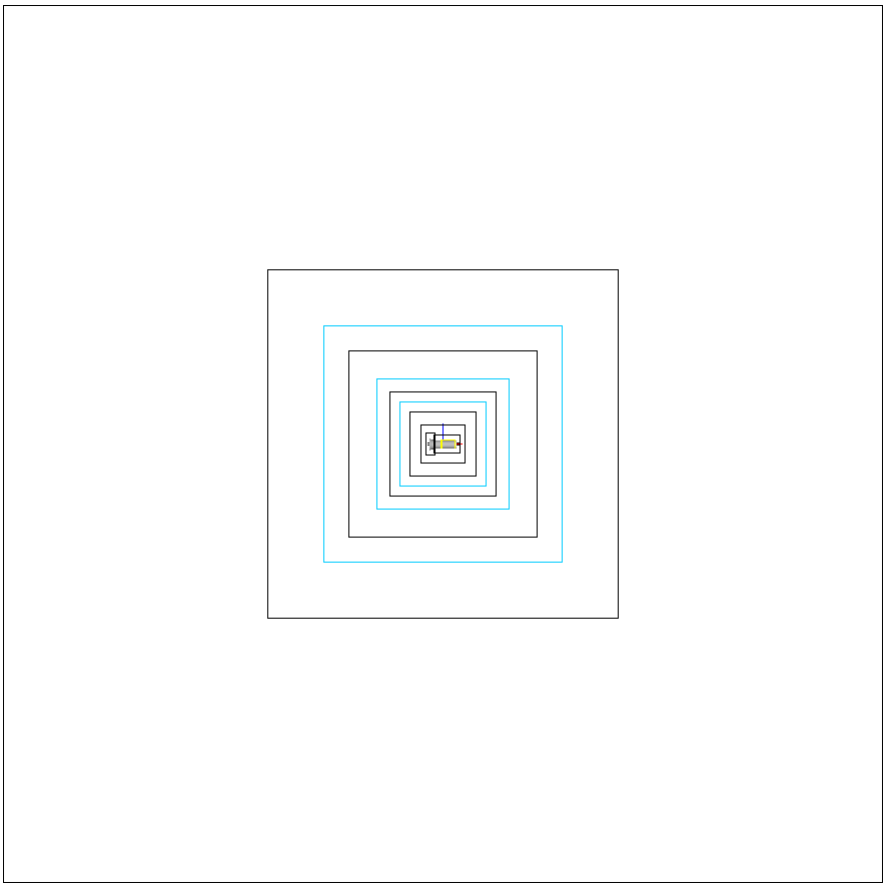

(a) Full simulation domain (mesh refinement volumes in black; viscosity volumes in blue).

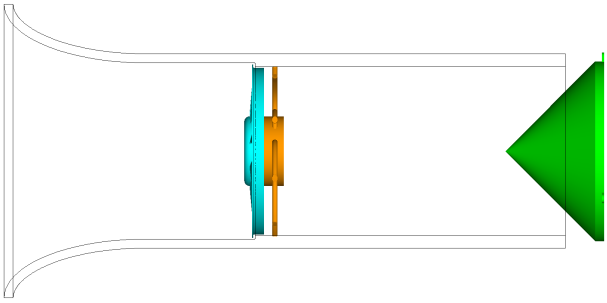

(b) Setup with a conical plug.

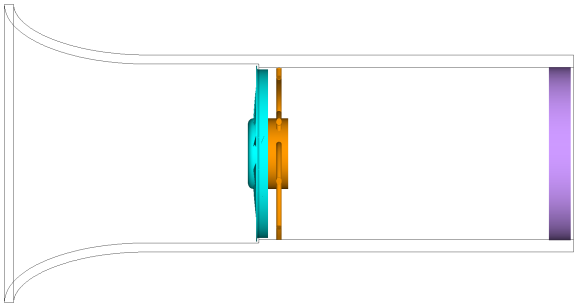

(c) Setup with a porous medium.

Figure 5.2 *PowerFLOW* numerical setup: Rotor in blue, stator in orange, duct in black, plug in green, and porous medium in purple.

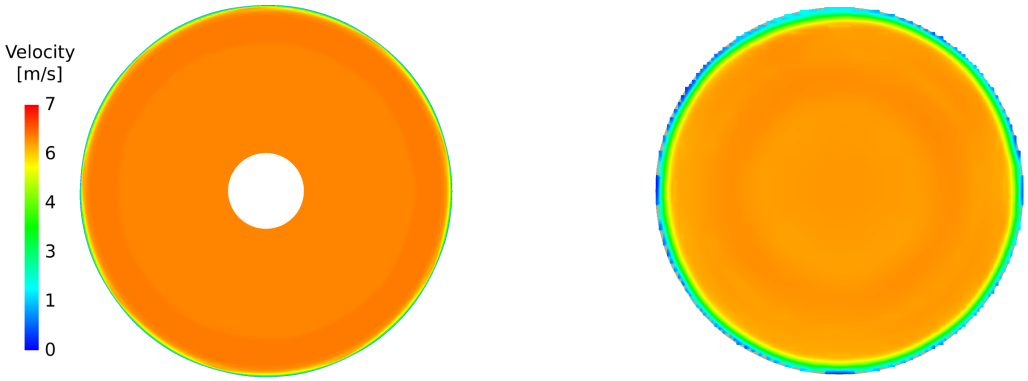

(a) *Turb'Flow* (URANS). (b) *PowerFLOW* (LBM).

Figure 5.3 Velocity magnitude at the fan inlet.

axial position of the plug and the thickness of the porous medium in order to obtain the desired flow rate (2500 m^3/h).

An outlet boundary condition with a free flow direction and an imposed ambient static pressure was applied on all the faces of the simulation domain. 11 mesh refinement volumes (in black in Figure 5.2a) defined the local the voxel size and three viscosity volumes (in blue in Figure 5.2a) changed the local viscosity in order to absorb the acoustic waves coming from the fan. Therefore, the setup was perfectly representative of a fully-anechoic room.

Given the results of previous convergence studies on this fan [Moreau *et al.*, 2011], the smallest voxel was set to 0.5 mm in a volume which included the rotor and the stator. From the smallest voxel size, the solver computed the time-step to ensure a CFL number of one (based on the speed of sound). In the present simulation, this resulted in a time-step of 8.243×10^{-7} sec.

The rotation of the fan was set using a volume of revolution which defined the sliding mesh interface between the fixed and the rotating fluid domains. The distance between this interface and the rotor wall was set to 10 times the local voxel size (5 mm).

Compressible LBM simulations allow a direct propagation of the acoustic sources. Therefore, the noise predictions were based on the pressure fluctuations captured at specific locations in the fluid domain, outside of the duct. In the present simulation, 62 point probes were placed on a sphere of 1.5-m radius from the rotor center to yield proper directivity and enough spatial resolution for sound power evaluation. At this distance the coarsest grid resolution was 64 mm, which gave an accurate capture of the acoustic waves up to

2.4 kHz or 6×BPF. [1] Unlike the FW-H analogy used with the *Turb'Flow* solver, the direct propagation of the sources to locations outside of the duct took into account the acoustic diffraction on the duct surfaces.

5.2.3 Solver performance

The performance of both solvers are presented in Table 5.1. On the one hand, *Turb'Flow* simulation was performed on the Mammoth Series II cluster (Intel Xeon E5462 2.8 GHz processors). The simulation was decomposed on 128 cores, giving a simulation speed of 176 hours per BPP (equivalent to 941 CPU-days). On the other hand, *PowerFLOW* simulations were performed on the Mammoth Parallel II cluster (AMD Opteron 6172 2.1 GHz). The computations were decomposed on 480 cores, leading to a simulation speed of 37 min per BPP (equivalent to about 12.5 CPU-days).

For aeroacoustic applications, the computed physical time (after convergence) must be long enough to obtain a sufficient frequency resolution in the acoustic spectrum. Despite the larger number of cells, the 360° geometry, and the larger simulation domain, *PowerFLOW* is 75 times faster than *Turb'Flow*. In an industrial context, only *PowerFLOW* could provide results within reasonable delays, and *Turb'Flow* would therefore be ruled out.

5.3 Experimental setup

The experimental setup took place in the fully anechoic room of the Université de Sherbrooke. Figure 5.4 presents the overview of the setup. To reproduce the numerical setup, the fan was placed in a duct which was machined in polycarbonate (PC) and acrylonitrile butadiene styrene (ABS) using fused deposition modeling (FDM). Due to prototyping constraints, the duct was designed in three parts: (1) the bellmouth and the fan interface, (2) the stator, and (3) the downstream part with the cone fixation.

1. It is here assumed that an accurate capture needs 5 points per wavelength, as shown by Brès *et al.* [2009].

Table 5.1 Solver performances for rotor-stator simulations.

	Cells	Cores	Time/BPP	Time/BPP for 1 core
Turb'Flow	7.9 M	128	176 hr	941 days
PowerFLOW Porous	67.5 M	480	37.5 min	12.5 days
PowerFLOW Plug	69.1 M	480	38.0 min	12.7 days
PowerFLOW Plug refined	72.2 M	480	38.5 min	12.8 days

The fan was driven by a 450-W electrical motor which is connected to a 20 V/40 A DC power supply. It should be noted that the maximum input voltage (20 V) led to a rotational speed between 2400 and 2450 rpm (instead of 2500 rpm in the simulation). Consequently, all the experimental results presented in this chapter were scaled according to a dipolar assumption at 2500 rpm to match the numerical results.

The aerodynamic and acoustic measurements are described in the following two sections.

5.3.1 Aerodynamic measurements

The fan operating point was controlled using a metal cone at the duct outlet, exactly as it was in the *PowerFLOW* simulations. The cone created a pressure drop at the outlet which modified the flow rate and the pressure rise across the fan.

The fan flow rate was estimated by a pitot tube (Figure 5.5). A micrometer screw attached to the duct translated the tube axially in order to measure a horizontal velocity profile between the end of the duct and the cone wall (see the line segment l in Figure 5.5b). The tube was carefully oriented in the flow direction to rule out any measurement inaccuracy. Assuming that the flow was perfectly axisymmetric, the resulting flow rate Q is given by

$$Q = 2\pi R\,\rho\,\Delta x \sin\beta \sum_{i=1}^{N} U_i, \tag{5.1}$$

where R is the radius position, ρ the air density, Δx the axial distance between two measurement points, β the velocity angle, N the number of measurement points, and U_i the velocity magnitude at the point i.

Five wall-pressure probes measured the static pressure inside the duct on a plane 150 mm downstream of the stator plane. Their values were averaged by connecting the probes to a single tube. The pressure rise across the fan was determined by the pressure difference between the probes and the ambient static pressure in the anechoic room.

5.3.2 Acoustic measurements

The acoustic pressure was recorded by eight 1/2-inch PCB HT378B02 microphones (377B02 microphone and HT426E01 preamplifier). Seven microphones were located in the horizontal plane, on the upstream semicircle, and one microphone was on the rotor plane, above the fan (see locations in Figure 5.4). Each location was 1.8 m away from the rotor center.

Figure 5.4 Experimental setup in the fully anechoic room.

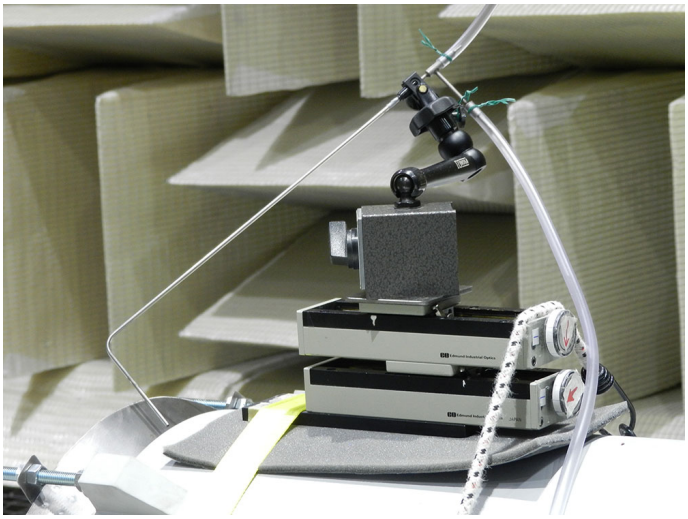

(a) Photograph of the pitot tube and the micrometric screw attached to the duct.

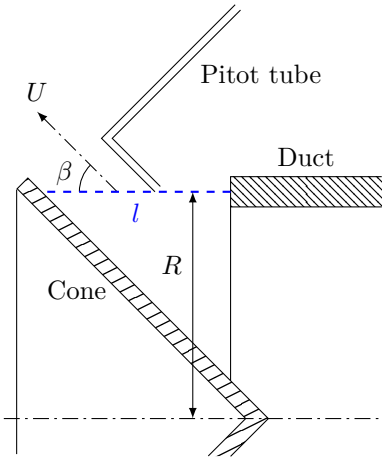

(b) Sketch of the duct output.

Figure 5.5 Flow rate measurement.

A Brüel & Kjær accelerometer Type 4397 was positioned on the duct in order to measure its vibrations and verify that no significant acoustic radiation of the duct wall was measured by the microphones. Figure 5.6 presents the frequency spectrum for each microphone along the acceleration measurement on the duct wall. A strong vibration occurs at the fan rotational frequency (42 Hz) and affects the noise at all the microphone locations. However, acceleration at higher frequencies was two to three orders of magnitude lower, which confirms that the duct vibration did not significantly impact the microphone measurements at the BPF (375 Hz).

5.3.3 Acquisition parameters

The signals from the microphones and the accelerometer were recorded using a 12-channel acquisition card and the Brüel & Kjær PULSE software.

The acquisition time was 40 sec for all the measurements. The time history was recorded and the acoustic spectra were computed by PULSE with a Hanning windowing and a 75-% overlap.

5.4 Aerodynamic results

5.4.1 Simulation convergence

In the *Turb'Flow* simulation, the initial aerodynamic field around the rotor was generated from the preliminary rotor simulation, resulting in a reduction of the transient time. The convergence was checked by monitoring the pressure rise across the fan, the flow rate on different sections, and the force applied on the rotor blade and the stator vane. The time evolution of these quantities are presented in Figure 5.7. The mean value of the three quantities is converged after 2.5 fan revolutions. After the convergence, small oscillations are observed at the BPF. These fluctuations are the result of the blade rotation on the surrounding flow field. Moreover, the polar plots of the forces (Figures 5.7e and 5.7f) confirm that the BPF cycles are regular after 2.5 revolutions.

Similarly, in the *PowerFLOW* simulation, the convergence of the three configurations was verified by monitoring the mass flow rate (Figure 5.8a), the pressure rise across the fan system (Figure 5.8b), and the forces applied on the rotor and the stator (Figures 5.8c and 5.8d, respectively). Unlike calculating the force on a single blade as in the *Turb'Flow* simulation (ring and hub were excluded), the force was computed from the integration over the full rotor surface (360°). As observed in Figure 5.8, the transient period lasts for 5 fan

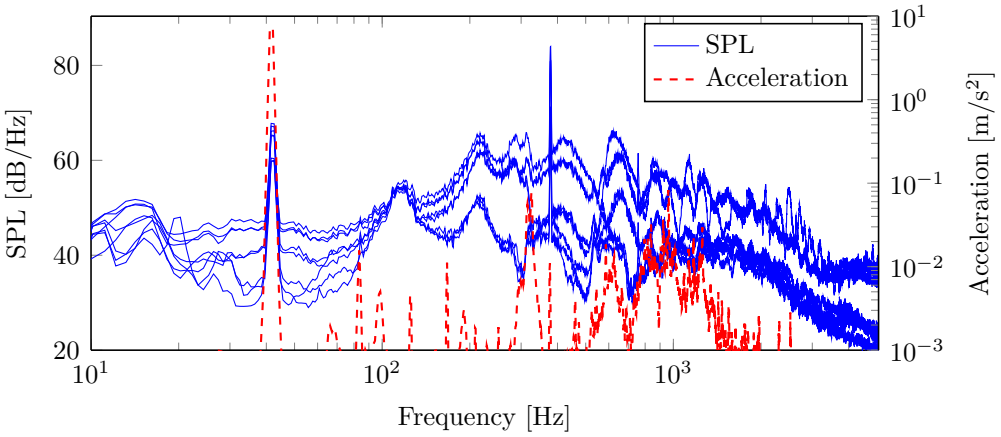

Figure 5.6 Sound pressure spectra at the microphone locations and acceleration spectrum of the duct wall.

revolutions, and converged flow conditions are obtained after 10 fan revolutions (it could be noted that the computation with a porous medium seems to have a longer convergence than the two other configurations). The aerodynamic and acoustic results presented in this chapter are thus processed from data collected after the end of the transient period.

Figure 6.7 also shows a negligible difference between the aerodynamic results with a porous medium and those with a conical plug. Only the force applied on the stator shows a small discrepancy, but no impact is observed on the static pressure prediction. The operating-point control device has thus a small influence on the recorded aerodynamic parameters. The use of a conical plug was thus preferred to match the experimental configuration. Additionally, similar aerodynamic predictions are observed for the two meshes around the conical plug, which validates the mesh convergence in the outlet region. Therefore, the results presented in the rest of this chapter were performed with the coarsest grid around the plug in order to reduce the simulation time.

5.4.2 Fan performance

In the experiments, the fan operating point was controlled by the cone opening l. The flow rate Q and the wall pressure rise ΔP_{wall} are presented in Table 5.2 for different openings. The numerical operating point is obtained for $l = 50$ mm. Therefore, all the measurements were performed with this cone opening in order to obtain similar flow conditions and comparable results.

The fan performance was evaluated on the pressure rise across the fan. The pressure rise was measured between the inside duct wall, 150-mm downstream of the stator plane, and

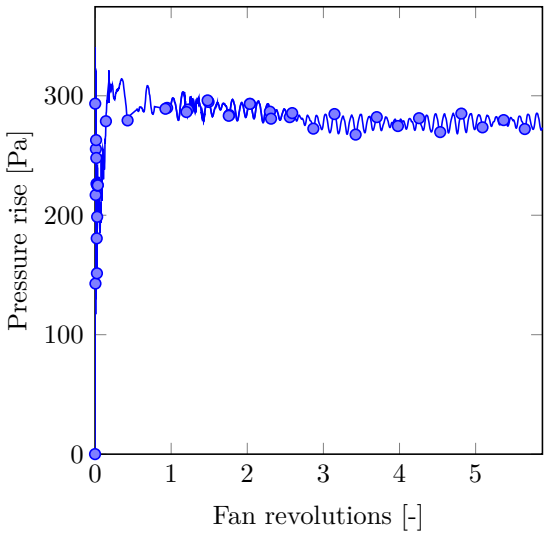

(a) Pressure rise across the fan.

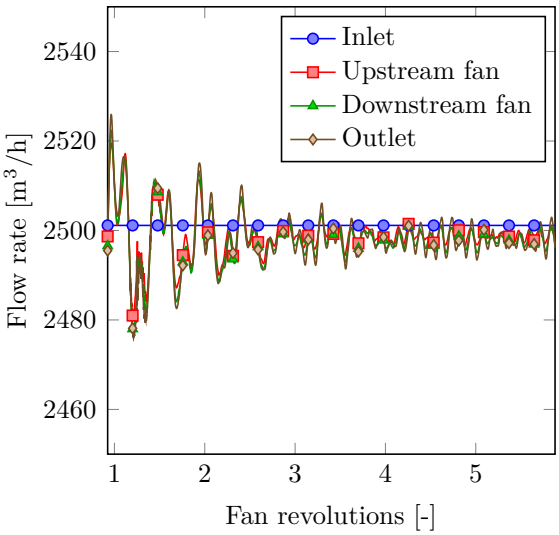

(b) Flow rate.

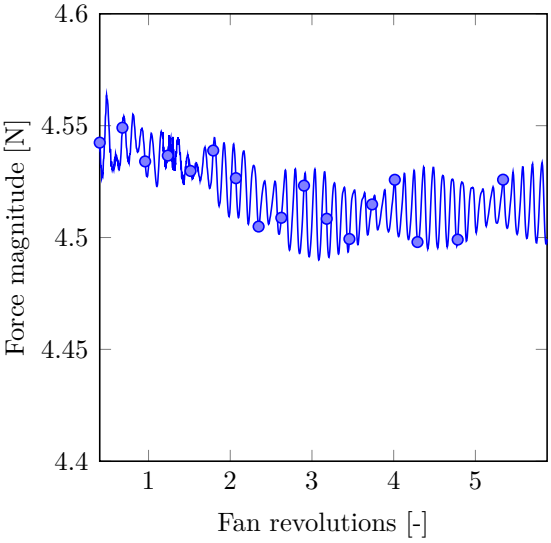

(c) Force applied on the rotor blade.

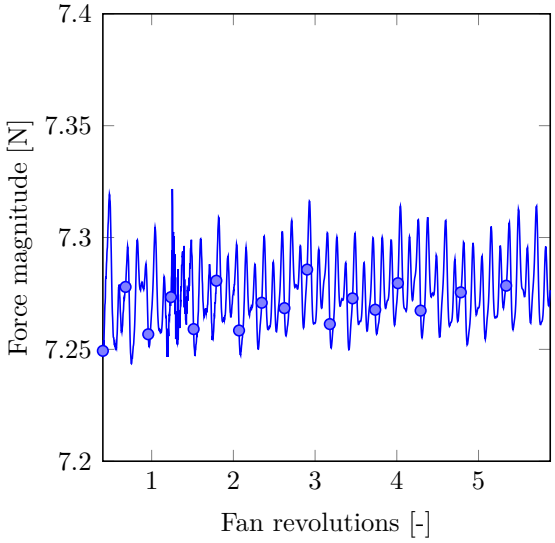

(d) Force applied on the stator vane.

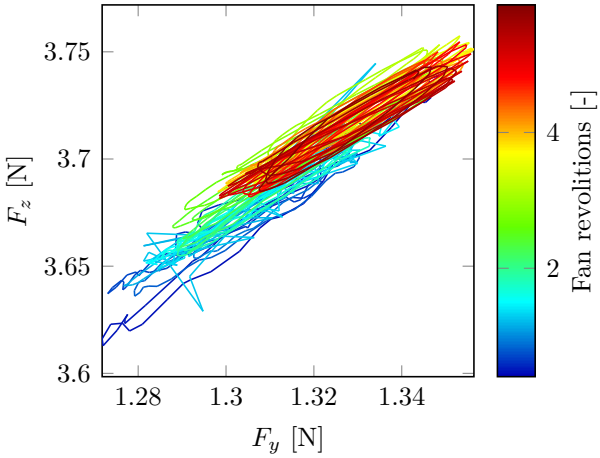

(e) Polar plot of the force applied on the rotor blade.

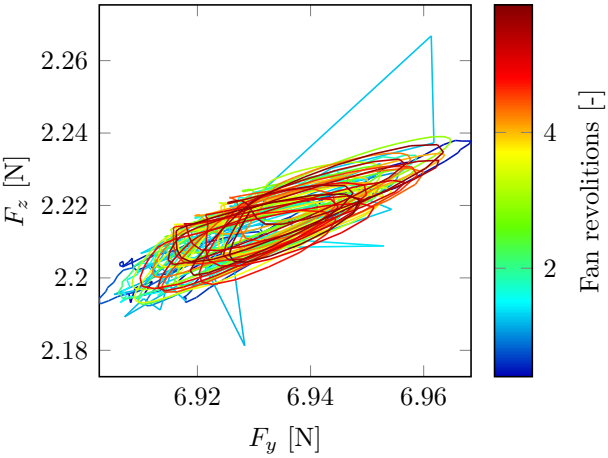

(f) Polar plot of the force applied on the stator vane.

Figure 5.7 *Turb'Flow* convergence.

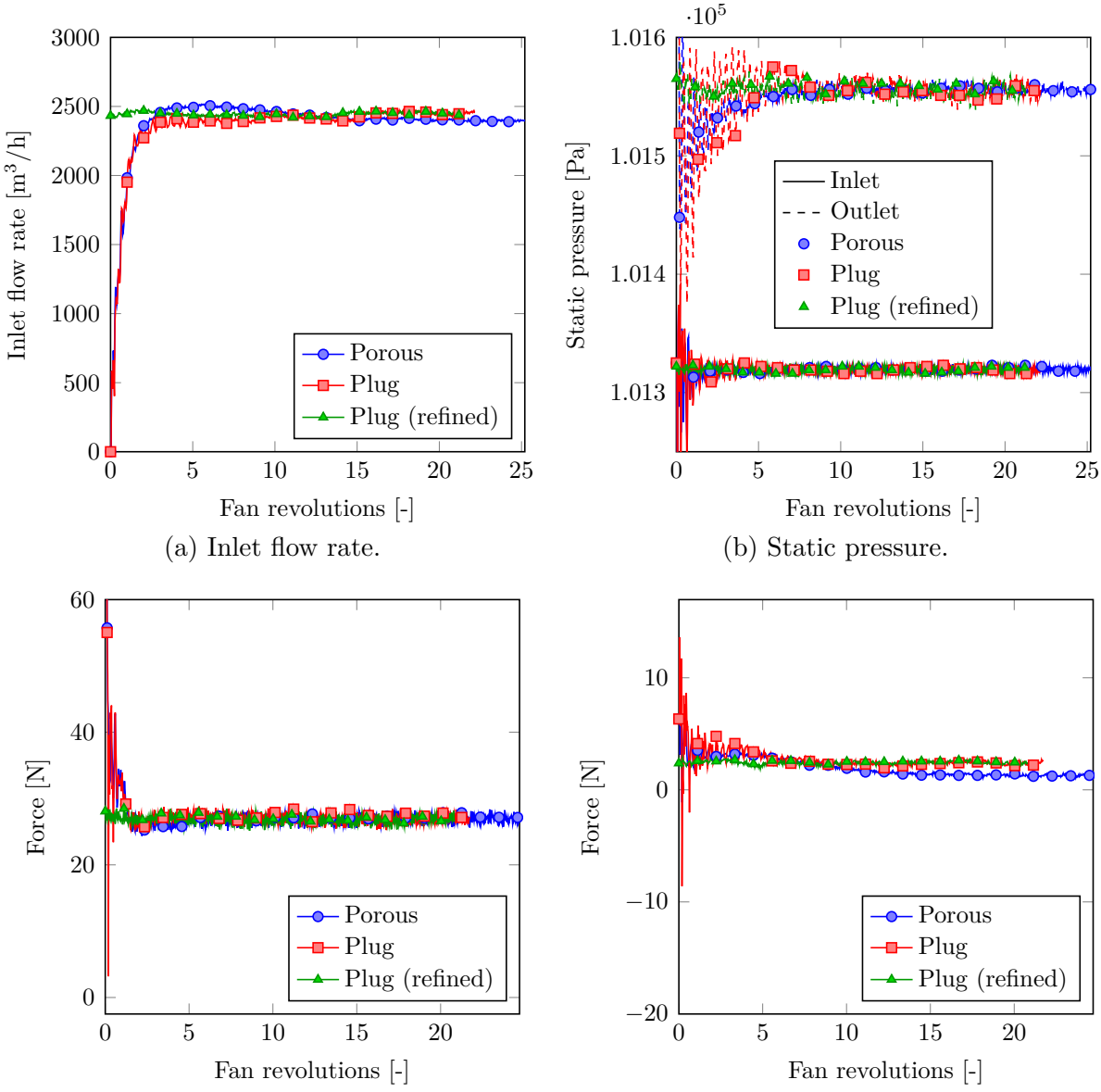

(a) Inlet flow rate.

(b) Static pressure.

(c) Axial force on the rotor.

(d) Axial force on the stator.

Figure 5.8 *PowerFLOW* convergence.

Table 5.2 Experimental result: Effect of the cone opening l on the fan operating condition.

l [mm]	Q [m^3/h]	ΔP_{wall} [Pa]
40	1763.4	321.8
50	2453.0	297.4
60	2700.6	270.6

the ambient pressure (or the inlet pressure in the *Turb'Flow* computation). The results for the two solvers are compared with the experiments in Table 5.3. Both numerical predictions show a good agreement with the measurements, the error being 2.0 and 3.0 % for the *Turb'Flow* and *PowerFLOW* simulations, respectively.

5.4.3 Flow topology

The mean axial velocity in a plane at constant angular position is presented in Figure 5.9. The two simulations show a similar flow topology in the vicinity of the fan. Because of the duct geometry, the fan wake is mostly axial rather than forming an angle with the rotating axis as it was the case in the simulation with the rotor alone (see Figure 4.6). Additionally, the tip-clearance backflow appears to go further upstream, whereas the vertical flow along the wall limited the size of the recirculation when the rotor was flushed-mounted on a plenum. The coherent structures of the flow highlighted in Figure 5.10 confirm this statement.

Similarly to the simulation with the rotor alone, vortices are formed in the tip-clearance recirculation and impinge the blade below the rotating ring. In the *Turb'Flow* simulation (Figure 5.10a), the RANS method predicts very large, coherent structures which cover one blade passage. At the same operating point, the computations with the rotor alone showed two smaller structures per blade passage (see Figure 4.7a). The ducted configuration, as opposed to the rotor flush-mounted on a plenum, likely explains this difference. Despite the finer turbulence structures computed by the *PowerFLOW* simulation (Figure 5.10b), large structures are also observed near the rotating ring, which is also observed in the *Turb'Flow* prediction.

Near the hub, the horseshoe vortex is clearly visible in both simulations. This structure is created by the flow separation occurring at the blade leading edge which convects downstream and spirals around the blade cusp at the trailing edge.

Figure 5.11 presents the phase-averaged static pressure and velocity magnitude at mid-span. It should be noted that the scales on the static pressure plots are different to take into

Table 5.3 Fan performance.

	ΔP_{wall} [Pa]	ϵ [%]
Experiment	297	-
Turb'Flow (URANS)	291	2.0
PowerFLOW (LBM)	288	3.0

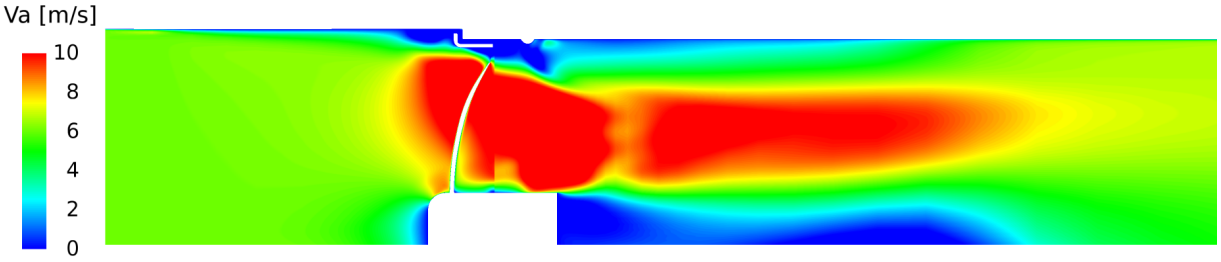

(a) *Turb'Flow* (URANS).

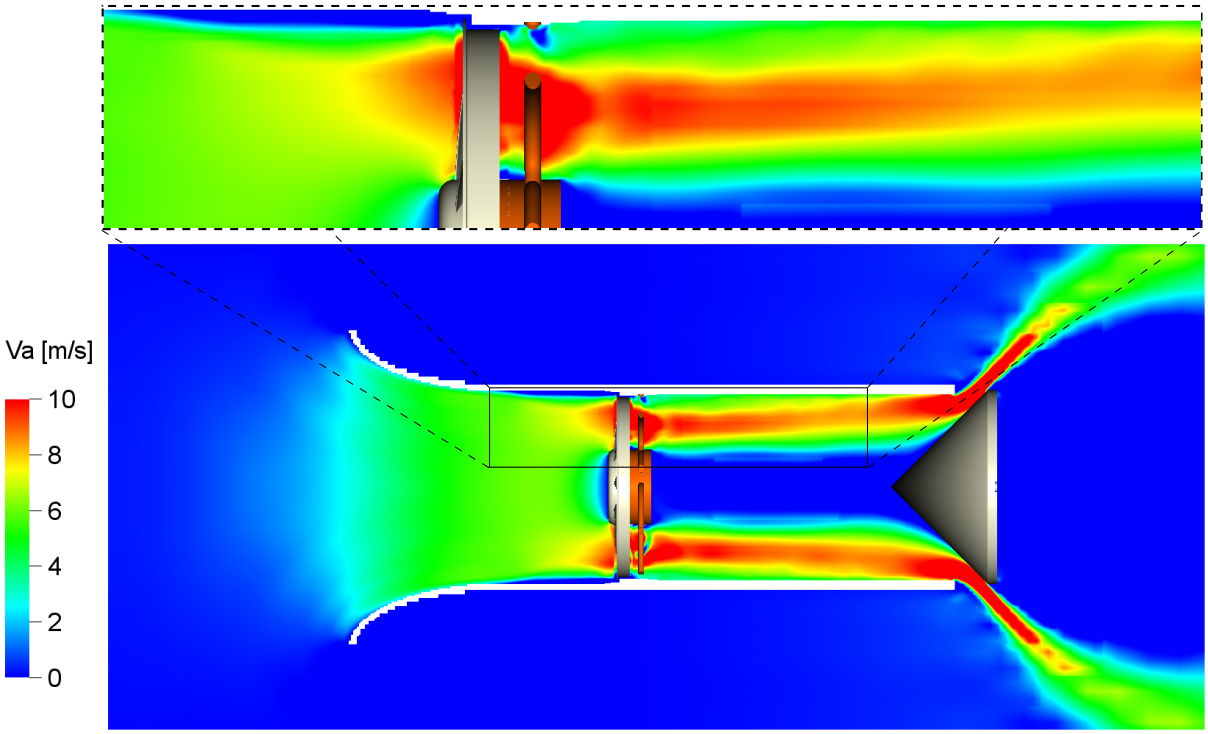

(b) *PowerFLOW* (LBM).

Figure 5.9 Mean axial velocity at constant angular position.

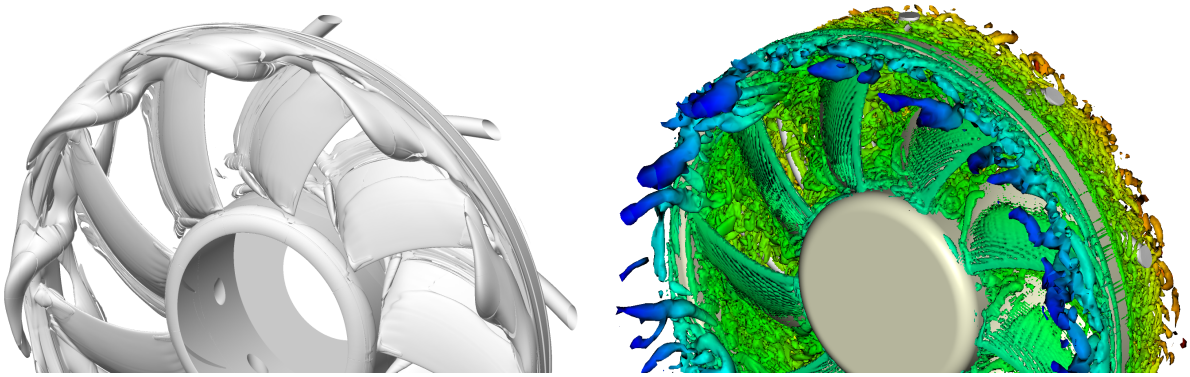

(a) *Turb'Flow* (URANS simulation, Q-factor).

(b) *PowerFLOW* (LBM simulation, λ_2 colored by the axial position).

Figure 5.10 Visualization of the vortex structures around the fan suction side.

account the mean pressure at the fan inlet, but the visualization demonstrates the ability to capture the field characteristics around the fan. The flows computed by the two solvers are in excellent agreement. Moreover, this figure highlights a strong rotor-stator interaction. First, the cylindrical stator vanes create an upstream pressure rise which appears to modify the blade loading. Second, the rotor wake interacts with the vanes, creating a periodic fluctuation of the wall pressure on the stator surface. These results confirm the expected two mechanisms induced by the stator design; hence a strong noise radiation should occur at the BPF.

Overall, an excellent agreement is observed between the two simulations.

5.4.4 Wake analysis

The aerodynamic results from the *Turb'Flow* and *PowerFLOW* simulations are compared in Figure 5.12. The three phase-averaged velocity components were extracted in two different axial planes (B and D). Plane B is at mid-distance between the rotor and the stator, whereas plane D is 15 mm downstream of the stator. Figure 5.13 presents the exact location of the planes relatively to the fan.

In plane B (Figure 5.12a), the two simulations are in very good agreement. The three velocity components show similar levels and patterns over most of the blade span. Close to the rotating ring, some discrepancies are observed between the *Turb'Flow* and *PowerFLOW* simulations. The radial velocity level is highly asymmetrical at high radius in the *Turb'Flow* computation, and the two other velocity components show a thicker annular zone. These differences are the result of the larger, more coherent vortices which are predicted by the RANS method. Consequently, the flow recirculation impacts the blade at a lower radial position under the ring, which generates some discrepancies in the downstream wake topology.

In plane D (Figure 5.12b), the patterns for the three velocity components are in agreement between the two computations, which confirms a similar interaction between the rotor wake and the stator. However, the velocity levels show some small discrepancies, particularly on the axial and radial components. Unlike a conventional stator, the cylindrical vanes do not straighten the flow and their wakes are relatively large. Moreover, the effect of the backflow recirculation on the tangential velocity remains visible in this plane, confirming its impact on the flow downstream of the stator.

The azimuthal-averaged velocity components in the two planes are presented in Figure 5.14. In plane B (solid lines), results are in agreement for the three velocity components. Further

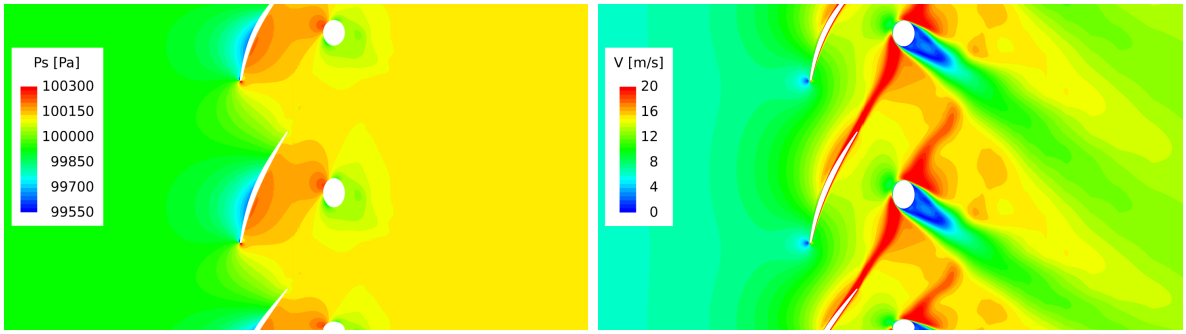

(a) *Turb'Flow* (URANS).

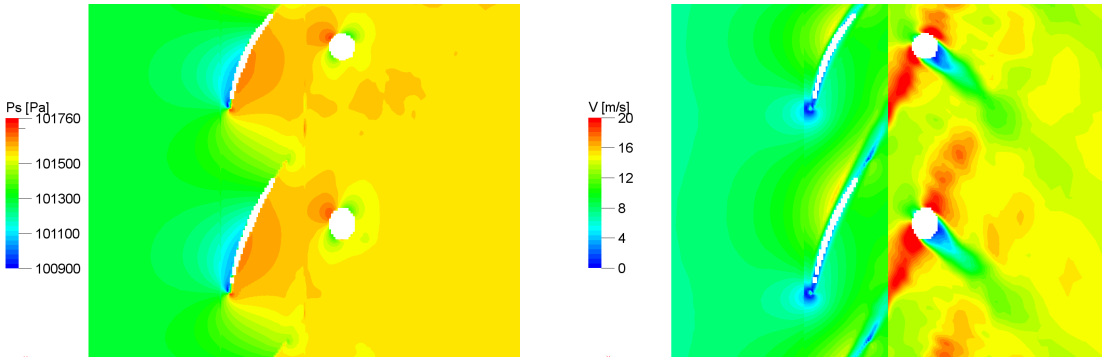

(b) *PowerFLOW* (LBM).

Figure 5.11 Phase-averaged flow at mid-span: static pressure on the left; velocity magnitude on the right (in the *PowerFLOW* simulation, the velocity in the rotor vicinity is computed in the rotating frame of reference).

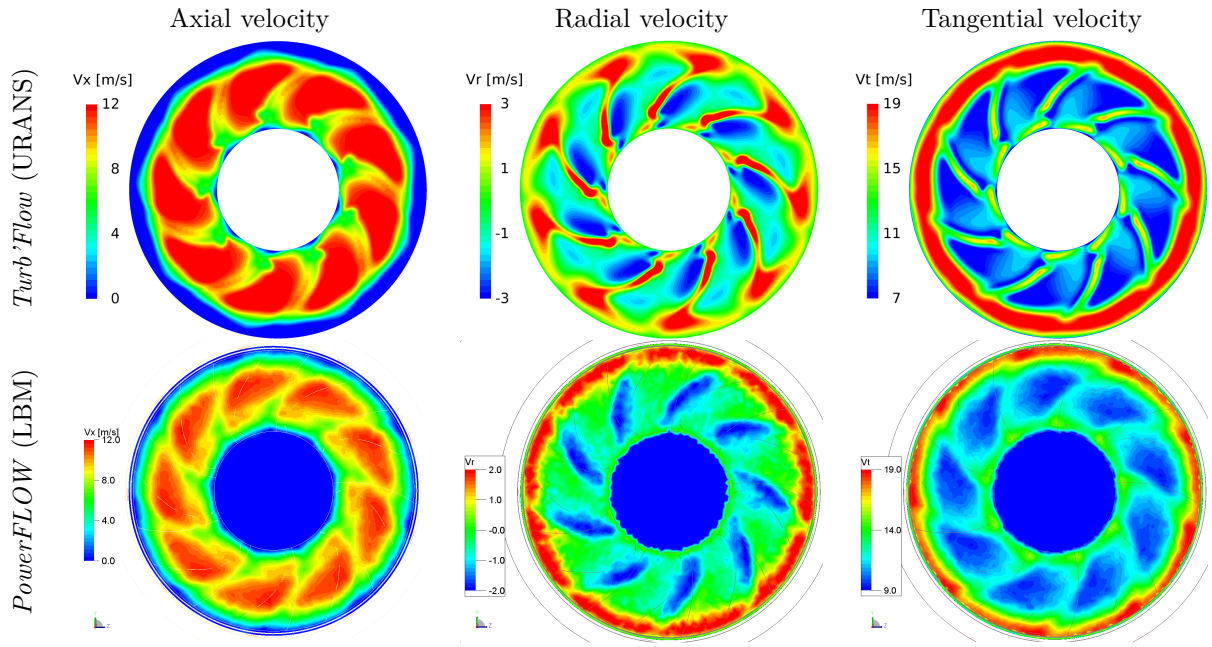

(a) Plane B (mid-distance between the rotor and the stator).

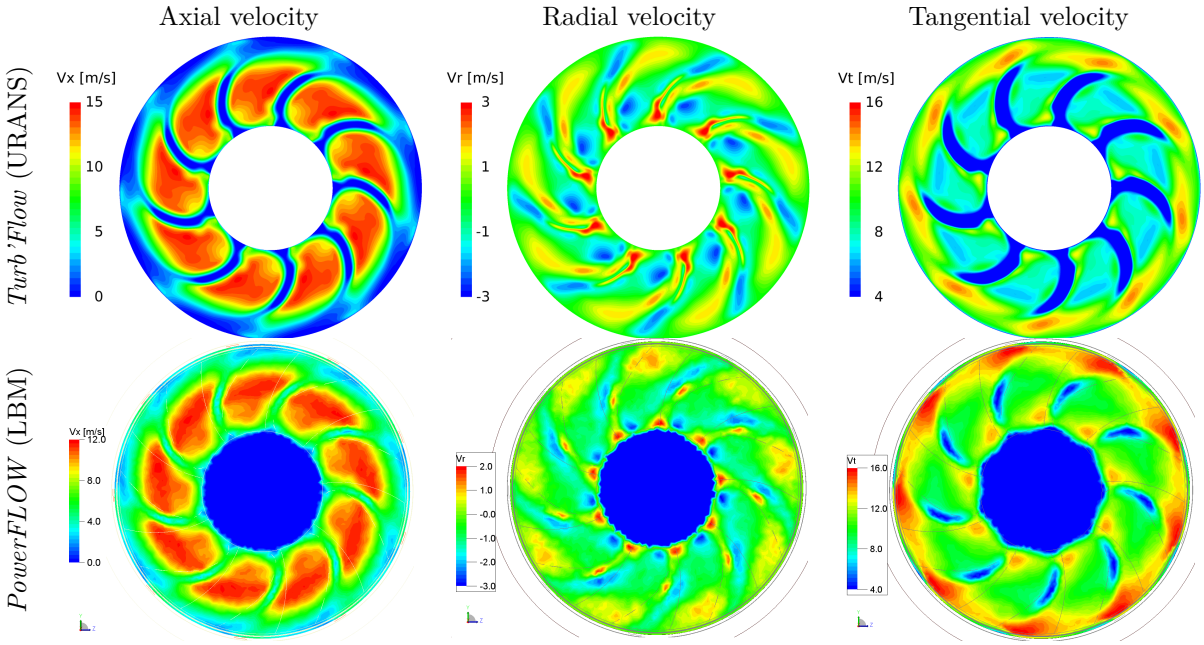

(b) Plane D (15 mm downstream of the stator).

Figure 5.12 Aerodynamic comparison of phase-averaged velocity components.

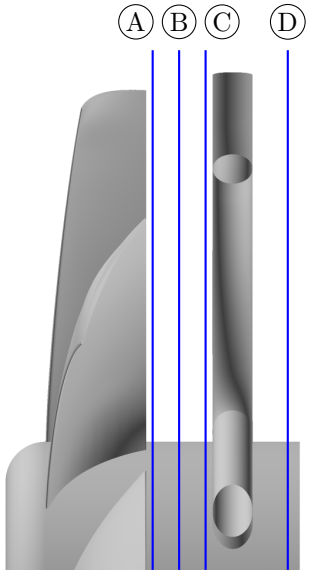

Figure 5.13 Position of the reference axial planes (A to D) used to post-process the aerodynamic data (rotor on the left, stator on the right).

downstream (plane D in dashed lines), a larger radial velocity at mid-span is predicted by *Turb'Flow*. This highlights differences in the rotor-stator interaction at this radius.

Overall, these numerical results from two very different solvers show similar predictions on the flow topology and the aerodynamic interaction between the rotor and the stator. Since the acoustic sources are created by this interaction, these coherent results are important to validate the fan noise analysis.

5.4.5 Acoustic excitation

Tonal noise is mainly caused by surface pressure fluctuations from several flow phenomena. Although the noise spectrum in far field could be used to understand the aeroacoustic mechanisms responsible for the acoustic radiation, a detailed analysis of the excitation can provide important information on these mechanisms.

In the present rotor-stator simulation, two different noise sources are expected: the rotor wake impingement on the stator vanes, and the potential effect of the stator on the rotor blades. Both sources are created by periodic azimuthal non-uniformities of the flow. The latter is induced by a non-uniform pressure whereas the former is the result of a non-uniform velocity profile. In order to identify and characterize the two perturbations, the flow field computed by *Turb'Flow* was recorded in two planes close to the sources (planes A and C in Figure 5.13), and the excitations were extracted at different radial positions.

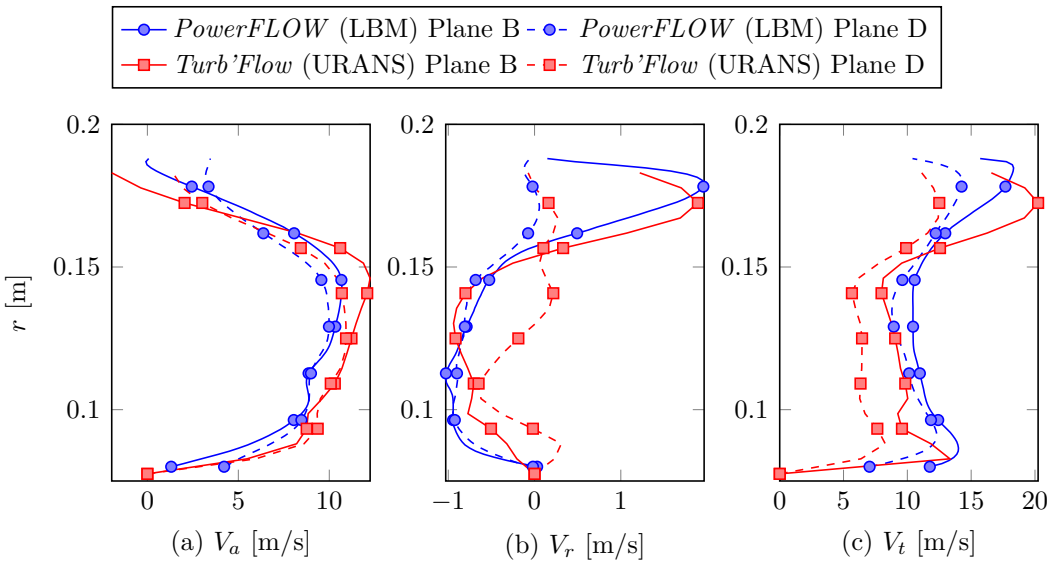

Figure 5.14 Azimuthal-averaged velocity components in planes B (mid-distance between the rotor and the stator) and D (15 mm downstream of the stator): (a) axial velocity, (b) radial velocity, (c) tangential velocity.

For the source located on the rotor (due to the potential effect of the stator), the static pressure was recorded in plane A positioned 2.5 mm downstream of the blade trailing edge and fixed in the stator frame of reference. Then, in order to isolate the potential effect and remove the fluctuations caused by the blades rotation, the pressure was averaged over a finite number of blade passing periods. Finally a circumferential Fourier transform was computed at different spanwise positions. The result shows an almost-perfect sinusoidal profile along the span (Figure 5.15a). This is confirmed by the Fourier transform (Figure 5.15b) which highlights a dominant circumferential mode B as its harmonics are 2 orders of magnitude below the fundamental. However, a higher frequency is also observed close to the ring where a non-negligible $2B$ mode is present. This behavior is certainly caused by the tip-clearance recirculation highlighted in Figure 5.10a which generates higher harmonics by impinging the blades under the ring.

For the source located on the stator (due to the rotor wake), the excitation is created by the non-axisymmetric velocity profile impinging the stator. This time, the velocity magnitude was recorded in plane C located 2.5 mm upstream of the stator leading edge, the plane being fixed in the rotor frame of reference. Then, the fluctuations caused by the stator vanes were removed by averaging the velocity over a finite number of blade passing periods and, finally, a circumferential Fourier transform was performed at different spanwise positions. The result in Figure 5.16 shows the same dominant B circumferential

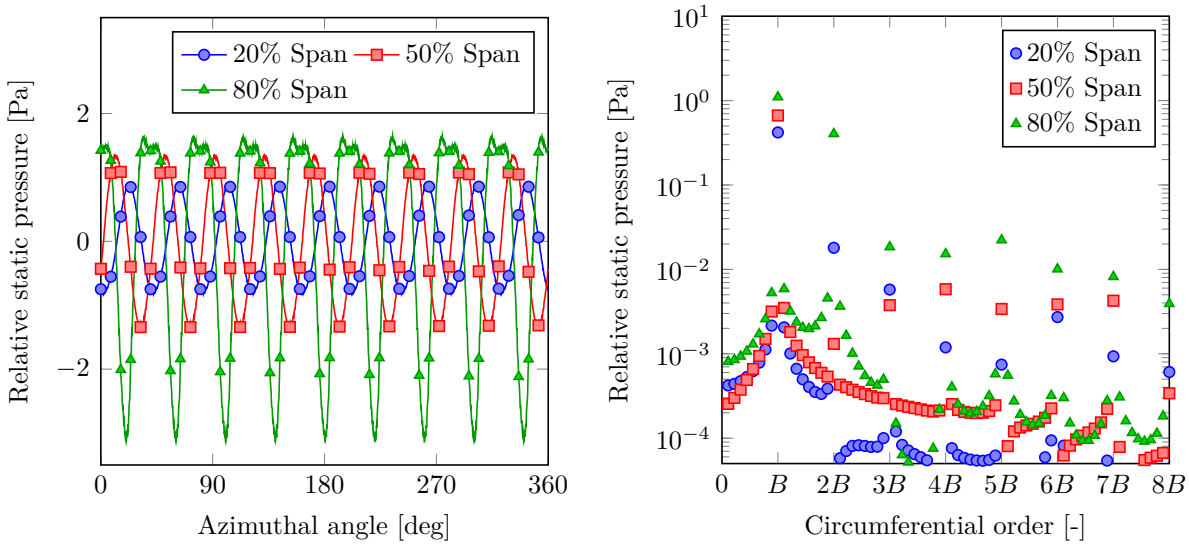

(a) Time-averaged static pressure in the absolute frame of reference, plots at constant spanwise positions.

(b) Circumferential Fourier transform of the time-averaged static pressure (B is the number of blades).

Figure 5.15 Rotor excitation in a plane 2.5 mm downstream of the rotor trailing edge. *Turb'Flow* URANS simulation.

order as for the rotor excitation. However, the impact of the flow recirculation does not appear since the effect of the backflow is largely dissipated before it reaches the stator leading edge.

This excitation analysis confirmed that the strong rotor-stator interaction should generate noise at the BPF, prior to using an acoustic analogy. In order to further characterize the acoustic sources, a study of the wall pressure fluctuations at the BPF is presented in the following section.

5.4.6 Source locations

The acoustic sources at a given frequency can be highlighted by filtering the surface pressure fluctuations. The wall pressure was recorded on the rotor and stator surfaces and a Fourier transform was performed at each point of the surface mesh. The result was then filtered around the BPF, which allows the visualization of the dipolar acoustic sources. *PowerFLOW* and *Turb'Flow* predictions are in good agreement (Figure 5.17).

As discussed in Section 5.4.3, a strong interaction occurs by design. On the rotor, strong sources at the BPF are observed along the blade trailing edge (both suction and pressure sides). This highlights the potential effect of the blunt stator vanes on the rotor. At the

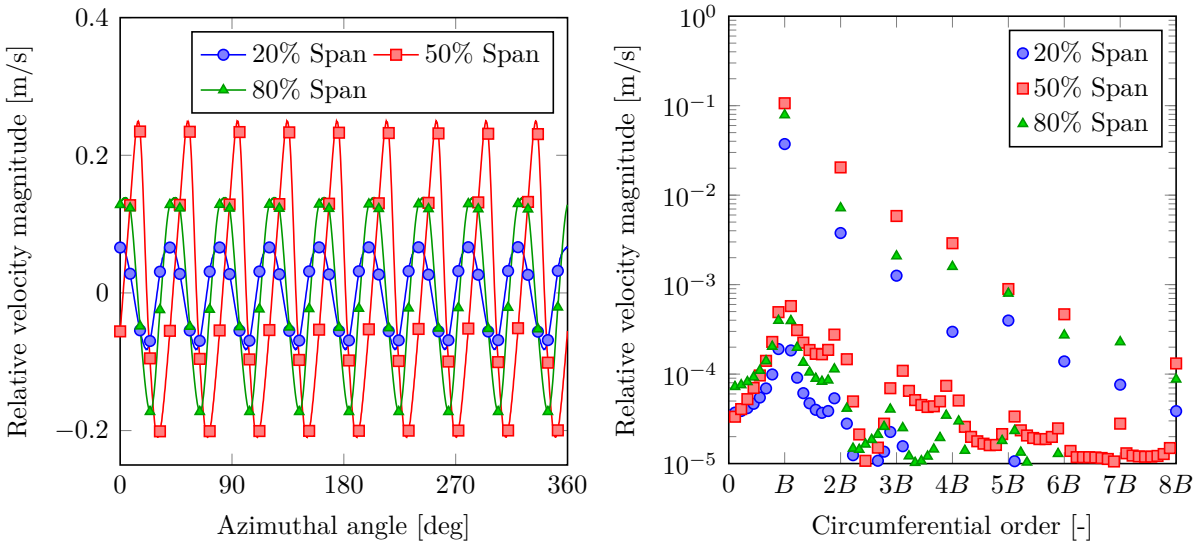

(a) Time-averaged static pressure in the absolute frame of reference, plots at constant spanwise positions.

(b) Circumferential Fourier transform of the time-averaged static pressure (B is the number of blades).

Figure 5.16 Stator excitation in a plane 2.5 mm upstream of the stator leading edge. *Turb'Flow* URANS simulation.

leading edge, some high fluctuation spots are visible in both simulations below the rotating ring. However, this source covers a very small area in the *Turb'Flow* simulation, which makes it barely noticeable in Figure 5.17a. These fluctuations are most likely the trace of the large backflow vortices impinging on the blade.

On the stator, most pressure fluctuations are concentrated at the leading edge of the cylindrical vanes along the whole span. The largest fluctuations are seen at the tip as the rotor wakes are more energetic close to the shroud.

For the *PowerFLOW* solver, it should be noted that these pressure fluctuations are independent of the selected mass flow device as the simulations with porous medium and plug yield the same levels and patterns. Similarly, no difference is found between the two plug refinements, which confirms the mesh convergence.

In summary, the noise sources are localized as expected on both the rotor blades and stator vanes, and the fluctuation spots confirm the flow topology analysis. High levels are present on the rotor and stator surfaces, which suggest that both parts have a significant contribution to the noise generation at the BPF. Moreover, *Turb'Flow* and *PowerFLOW* are in excellent agreement, predicting similar source locations.

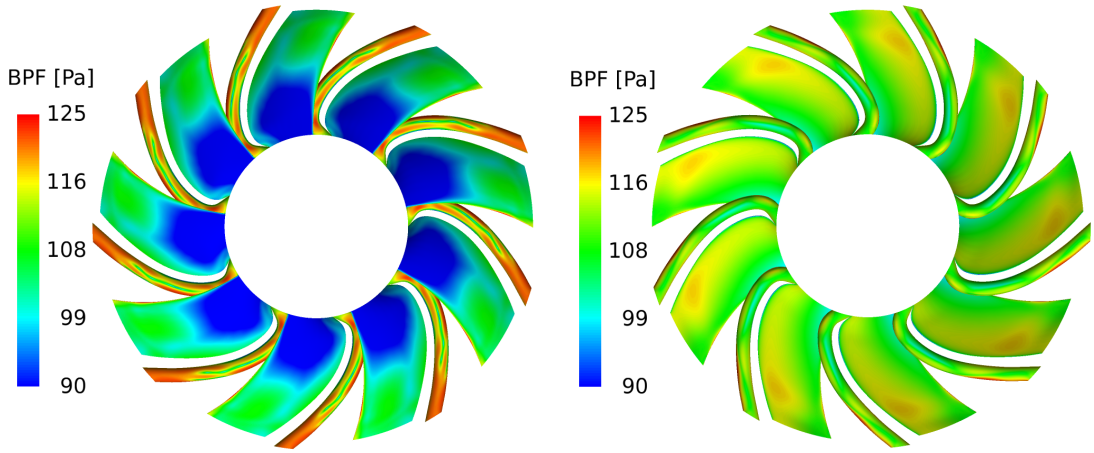

Suction side Pressure side

(a) *Turb'Flow* (URANS).

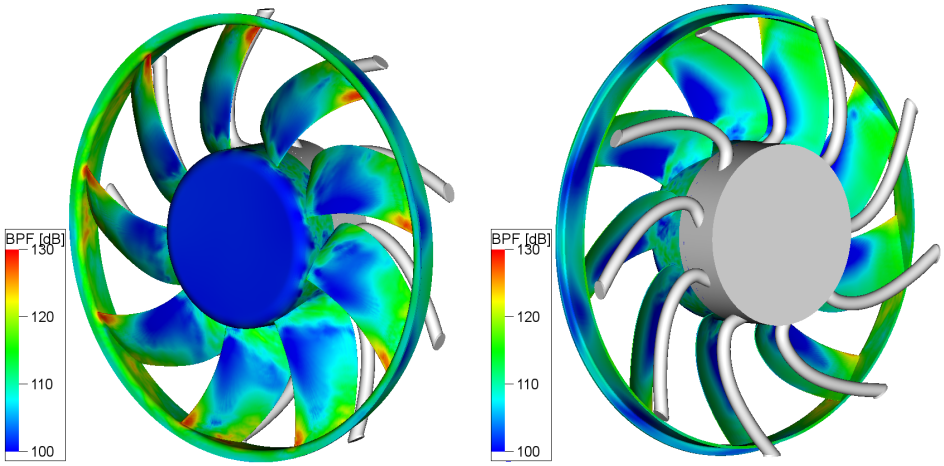

Rotor suction side Rotor pressure side

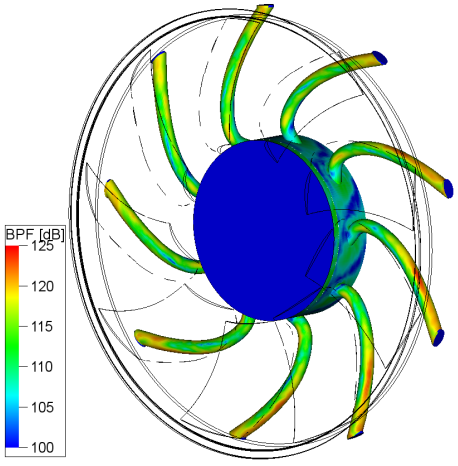

Stator

(b) *PowerFLOW* (LBM).

Figure 5.17 Wall-pressure fluctuations at the BPF on the fan surfaces.

5.5 Acoustic results

5.5.1 Influence of the operating-point control device

Prior to analyzing the fan acoustic signature, the influence of the operating-point control device used in the *PowerFLOW* simulation was investigated. The acoustic results for the three setups are presented in Figure 5.18.

The sound pressure level at the upstream location (Figure 5.18a) shows negligible differences between the three setups. At this probe location, the broadband noise and the BPF tone level are the same. Downstream of the duct (Figure 5.18b), some differences are observed on the broadband noise between the simulations with a conical plug and the one with a porous medium. Contrary to the plug, the porous medium does not deviate the flow at the duct outlet; hence the probe is located inside the air flow, which creates a higher broadband level due to the pseudo-sound captured by the probe.

As for the sound power level (Figure 5.18c), the three simulations show negligible differences. More importantly for the scope of this thesis, the operating-point control device has no influence on the tonal radiation at the BPF, and the two mesh refinements yield the same results. Therefore, the use of the conical plug *without* mesh refinement is validated.

5.5.2 Noise characterization

The main goal of the present chapter was to characterize the noise radiated by the rotor-stator configuration.

In the *Turb'Flow* prediction, the sound power spectrum was computed from the propagation of the dipolar sources using a FW-H acoustic analogy. This hybrid method allowed the separation of the rotor and stator contributions to the noise level. The results are presented in Figure 5.19.

As expected from the excitation analysis (Section 5.4), the total sound power spectrum is dominated by a tone at the BPF. The separate contributions show that the noise radiation at this frequency is dominated by the sources located on the rotor. In other words, the interaction between the rotor and the stator potential effect radiates more than the interaction between the rotor wakes and the stator. This is the result of the blunt cylindrical profile which is located very close to the rotor leading edge. Additionally, total rotor surface is much larger than the stator, which results in a greater contribution to the acoustic radiation.

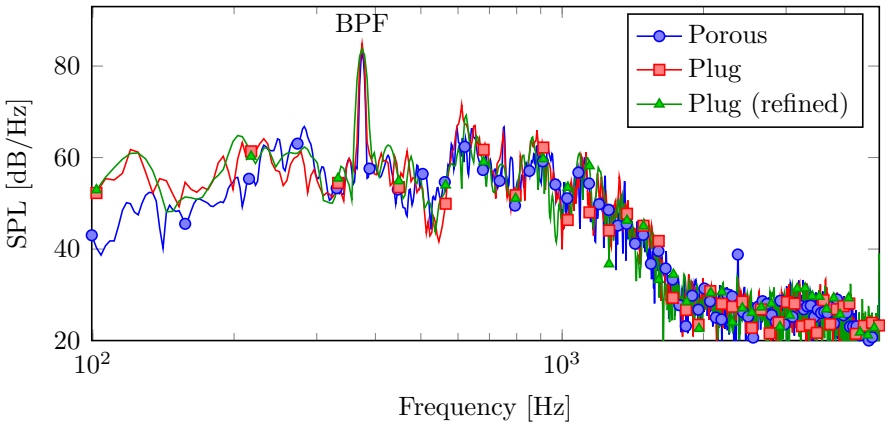

(a) Sound pressure level at the upstream probe on the rotor axis.

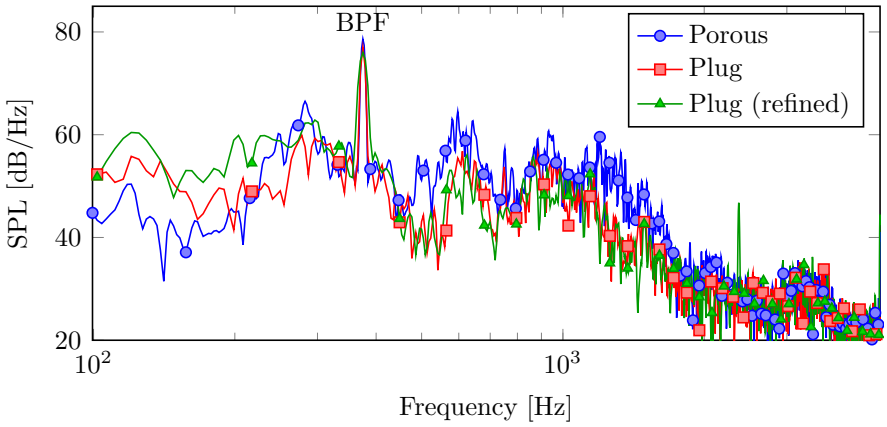

(b) Sound pressure level at the downstream probe on the rotor axis.

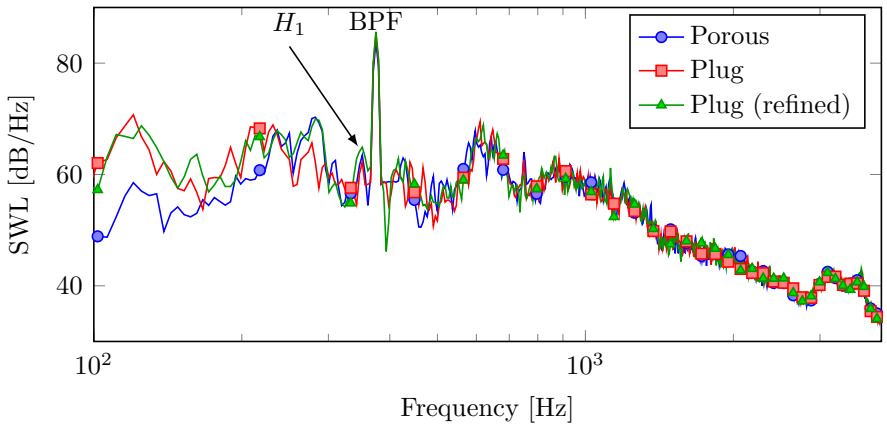

(c) Sound power level.

Figure 5.18 Acoustic comparison between the three *PowerFLOW* (LBM) setups.

Another set of tones also appears in Figure 5.19 at the frequency H_1 and its harmonics H_2, H_3... This tonal noise is generated by the impingement of backflow vortices on the rotor blades. The Q-factor visualizations (see Figure 5.10a) confirmed that the vortices impact the blade at the frequency $H_1 = 350$ Hz. The negligible stator contribution at these frequencies also confirms that the sources are only located on the rotor surfaces.

The sound power level at the BPF and its first harmonic is presented in Table 5.4 for the *Turb'Flow* and *PowerFLOW* predictions. Both simulations are in very good agreement, showing 3- and 2-dB differences at the BPF and its first harmonic, respectively. Since the URANS simulation only models the larger turbulent structures, the *Turb'Flow* spectrum shows a lack of broadband noise and the tones appear to emerge more.

Due to the broadband content captured by *PowerFLOW*, the tone at the frequency H_1 does not appear clearly in the SPL spectra (Figures 5.18a and 5.18b). However, a tone at 350 Hz is clearly visible in the sound power spectrum (Figure 5.18c). Since this frequency H_1 is the same as in the *Turb'Flow* prediction, this confirms that the angular velocity of the backflow vortices is in good agreement between the two numerical methods. Moreover, the backflow vortices are larger and more coherent in the *Turb'Flow* computation (see Figure 5.10). The lower H_1 level predicted by *PowerFLOW* (see Table 5.4) is therefore coherent with the flow visualizations.

Consequently, the design of the stator was appropriate to generate a strong tonal noise at the BPF. Hence, the primary noise of the fan is characterized and theoretically controllable with a static obstruction.

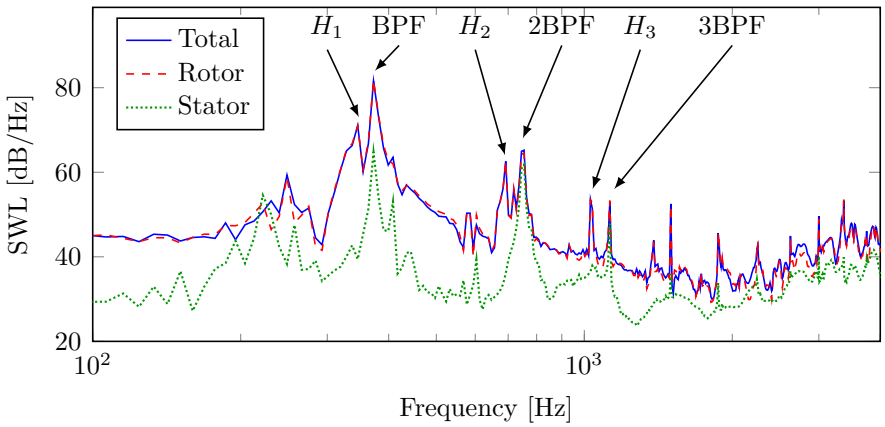

Figure 5.19 *Turb'Flow* (URANS) simulation: sound power level.

Table 5.4 Sound power level at the BPF, its first harmonic, and the frequency H_1.

	BPF [dB]	2×BPF [dB]	H_1 [dB]
Turb'Flow (URANS)	82	63	70
PowerFLOW (LBM)	85	65	65

5.5.3 Primary noise validation

The sound pressure spectrum on the rotor axis for the fan alone is presented in Figure 5.20. The *PowerFLOW* simulation shows a very good agreement with the measurements. For both microphone locations, the amplitude of the BPF tone is very well captured and the broadband noise perfectly matches the experimental results up to 1500 Hz. At this frequency, the local mesh size (64 mm) is approximately equal to the third of a wavelength; hence the acoustic waves are not fully resolved by the mesh and a strong damping occurs beyond this limit. The upstream directivity of the SPL at the BPF (Figure 5.21a) and the overall SPL (OASPL) integrated between 100 and 1000 Hz (Figure 5.21b) confirms this statement. *PowerFLOW* results are in excellent agreement with the experiment, showing only a maximum difference of 2 dB. Furthermore, it can be noted that the directivity exhibits a radiation from a typical compact dipole – as expected at low frequency.

As for the *Turb'Flow* prediction, Figures 5.20 and 5.21a show that the noise radiation at the BPF is underpredicted on the fan axis and in the rotor plane (6- and 10-dB difference, respectively). As expected, the lack of broadband content inherent to the URANS method causes an underprediction of the OASPL (Figure 5.21b).

5.6 Conclusion

In order to enhance the noise radiation at the BPF, a stator was designed and placed downstream of the automotive cooling rotor. Two complete aeroacoustic simulations were performed on this rotor-stator configuration. The first one used the Navier-Stokes solver *Turb'Flow* combined with a FW-H analogy, and the second one consisted of a direct acoustic prediction with the LBM solver *PowerFLOW*. Results were compared to measurements in a fully-anechoic room.

The two codes predicted very similar aerodynamic results which were in good agreement with the experiments. The main differences between the numerical results lay in the simulation domains: a 360° geometry was taken into account in the LBM setup whereas only a single blade passage was computed by the URANS solver. Consequently, the

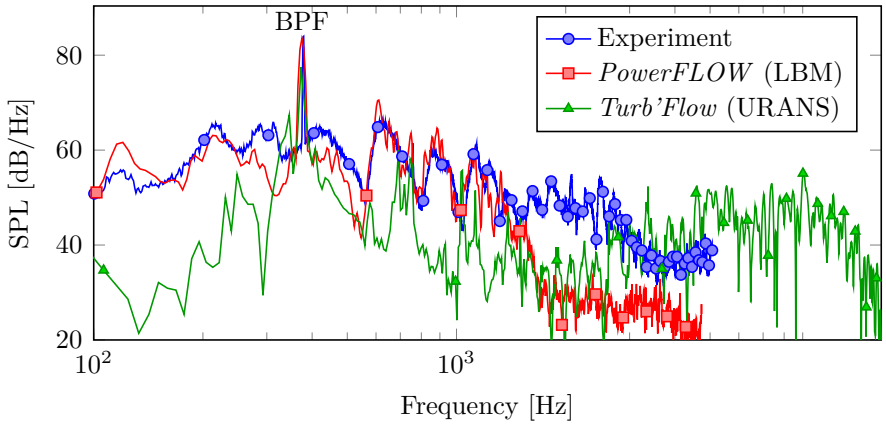

(a) Microphone on the rotor axis.

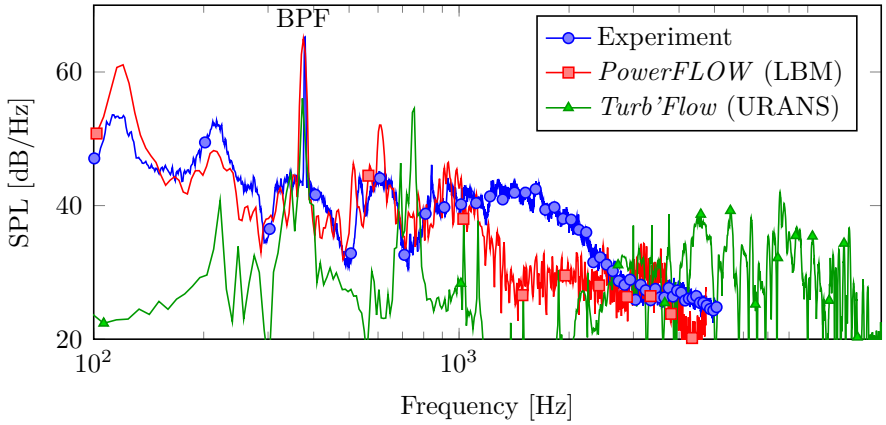

(b) Microphone on the rotor plane.

Figure 5.20 Sound pressure level without obstruction: comparison between experiment and simulation; microphone on the rotor axis, upstream of the fan.

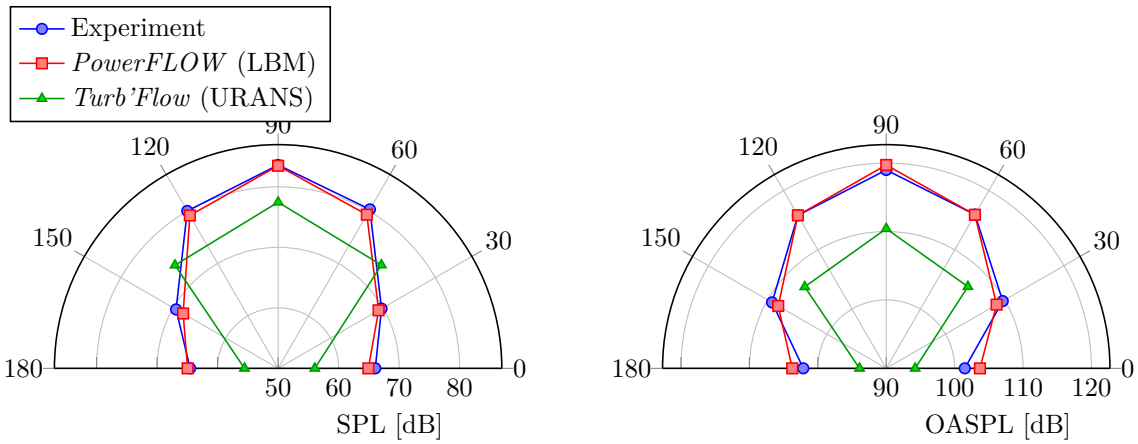

(a) BPF (375 Hz).

(b) OASPL computed over a wide frequency range (100–1000 Hz).

Figure 5.21 Upstream directivity centered on the rotor (90° corresponds to the fan axis).

backflow vortices were found to be larger in the *Turb'Flow* simulation, which had an impact on the velocity field downstream of the rotor.

The aerodynamic results were also used to investigate the rotor and stator acoustic excitation as well as the noise source locations. Two aeroacoustic mechanisms were highlighted: the stator potential effect on the rotor, and the impingement of the rotor wakes on the stator.

The noise predictions confirmed the aerodynamic results. The rotor-stator configuration generates a strong radiation at the BPF and its harmonics. The tonal and broadband content computed by *PowerFLOW* showed an excellent agreement with the microphone measurements. However, *Turb'Flow* results showed the limitations of the URANS method on a single blade passage, as the noise at the BPF was significantly underpredicted.

In conclusion, this complete aeroacoustic study characterized the primary noise radiated by the rotor-stator configuration and confirmed the presence of dominant noise sources at the BPF. This configuration thus allows an investigation of the noise control method using a static obstruction.

CHAPTER 6

TONAL NOISE CONTROL WITH FLOW OBSTRUCTION: AEROACOUSTIC SIMULATIONS AND EXPERIMENTS

In the previous chapter, the investigation of a rotor-stator configuration showed a strong radiation at the BPF. This fan thus appeared to be an ideal canonical case to thoroughly study the noise control method with flow obstruction. The present chapter therefore aims at performing a complete computation of the obstruction-fan interaction to better understand the aeroacoustic mechanisms responsible for the tonal noise reduction. Furthermore, an industrially-applicable numerical methodology is proposed to obtain an optimal obstruction design prior to any prototyping and measurement.

The design methodology is introduced in Section 6.1. Section 6.2 presents the numerical simulations with static and rotating obstructions. Finally, measurements in fully-anechoic conditions are discussed in Section 6.3.

6.1 Design methodology

As stated in Chapter 2, Gérard *et al.* [2008] showed that an additional inlet flow distortion induced by a carefully-shaped obstruction is able to significantly reduce tonal noise from low-speed fans. Such obstructions are cheap and easy to manufacture, and they may have a low impact on the aerodynamic fan performance [Gérard *et al.*, 2009a].

This adaptive-passive control method was first investigated analytically and experimentally. An analytical approach was used to create a simple model of the obstruction-fan interaction, which allowed to test the harmonic content of different obstruction shapes in order to act at a single frequency without affecting the harmonics [Gérard *et al.*, 2009b]. Tests confirmed the feasibility of the method [Gérard *et al.*, 2009a], but measurements have a limited potential to study the aeroacoustic mechanisms responsible for the noise reduction. Additionally, the experimental optimization of the obstruction design and position remains expensive in terms of facilities, human resources and time. As an alternative, the development of a reliable optimization methodology based on numerical simulations may be very beneficial in

an industrial context. Moreover, Pérot *et al.* [2012] showed that LBM numerical simulations were able to capture the obstruction-fan interaction and its impact on the BPF radiation, but the physical interpretation of the noise reduction is still unclear and controversial.

For a given fan, this numerical methodology aims at obtaining a preliminary design of an optimized flow obstruction in order to reduce tonal noise at the frequency $nB\Omega$, where n is an integer defining the harmonic order, B the number of rotor blades, and Ω the rotor speed in Hertz. Given the large computational cost associated with fan simulations (see Chapters 4 and 5), the proposed methodology was developed to design an optimal flow obstruction with a minimal number of simulations. To face industrial time constraints, this methodology relies on the separation of the primary noise radiated by the fan and the secondary noise induced by the flow obstruction. This separation is made possible by rotating the obstruction *in the optimization process*, which shifts the secondary tone (created by the obstruction-fan interaction) in the frequency spectrum [Gérard *et al.*, 2013] and thus allows the characterization of the secondary source with respect to the primary source. Although the methodology is based on aeroacoustic simulations, it should be noted that the same process can also be applied experimentally.

The sinusoidal obstruction geometry – which proved to be the most harmonically selective [Gérard *et al.*, 2009b] – is defined by three parameters (Figure 6.1): the base radius r_1, the mid-lobe radius r_2, and the sinusoidal lobe amplitude A. Depending on the fan type and installation constraints, the obstruction can have either external or internal lobes (see Figures 6.1a and 6.1b, respectively). The former is better suited to axial machines, whereas the latter is easier to implement in centrifugal machines. The number of lobes L is chosen according to the harmonic order n to control. The main tonal radiation is generally due to the circumferential mode nB, leading to $L = nB$. However, modes $nB \pm 1$ or $nB \pm 2$ may also significantly impact the noise at the frequency $nB\Omega$, particularly at locations away from the rotor axis. This behavior appears in the rotating dipole formulation (Equation (3.47)) since the pressure fluctuation at the frequency $mB\Omega$ is directly related to the Bessel function J_{mB-s} which is maximum for the excitation harmonics $s = \{mB, mB \pm 1, mB \pm 2\}$. In this case, a combination of different numbers of lobes may yield a better control, but this possibility is not taken into account in the proposed methodology where only the BPF is targeted.

It should be noted that the maximum obstruction thickness ($|r_2 - r_1| + A/2$) generally ranges from 0.5 to 2 cm. Consequently, the obstruction is acoustically compact for frequencies up to more than 8 000 Hz. In a typical low-speed fan (BPF = 600 Hz), the diffraction on the obstruction surfaces can be considered negligible up to the 13^{th} harmonic of the BPF.

The optimized design for a given obstruction is defined by two parameters:

— $A_{opt}(nB\Omega)$, the radial amplitude of the obstruction which controls the magnitude of the secondary source;

— $\phi_{opt}(nB\Omega)$, the obstruction angular position which controls the phase of the secondary source.

6.1.1 Assumptions

The proposed methodology considers the following assumptions:

— The obstruction-fan distance remains constant and the secondary source level is controlled by the lobe amplitude; [1]

— The obstruction-fan distance is larger than the maximum axial rotor chord in order to neglect the rotor potential effect on the obstruction;

— Obstructions are frequency selective: for each n, the geometrical parameters $\phi(nB\Omega)$ and $A(nB\Omega)$ only have an effect at the frequency $nB\Omega$;

— Around the optimal lobe amplitude A_{opt}, the secondary source level $20\log_{10}(p_s)$ varies linearly with the lobe amplitude (this assumption was verified in the studied configuration);

— The obstruction rotation speed Ω_o should be slow enough to assume a quasi-static flow at each angular position (this assumption is properly addressed in Sections 6.2 and 6.3);

— The physical time computed after convergence is on the order of 10 lobe passing periods LPP $= (nB\Omega_o)^{-1}$.

6.1.2 Methodology description

The overview of the numerical methodology is presented in Figure 6.2. The actions performed (on the left) and the results (on the right) are indicated for each step. The details are presented in the following sections.

Step 1: Primary noise characterization

First, the primary acoustic field $p_p(\boldsymbol{x}, \omega)$ of the fan (without an obstruction) is computed at the locations $\boldsymbol{x}$ where the noise should be controlled. The simulation has to account for the real installation environment in order to accurately capture the flow distortions

1. It should be noted that the same methodology could be applied if the secondary source level was controlled by the obstruction-fan distance and the lobe amplitude remained constant.

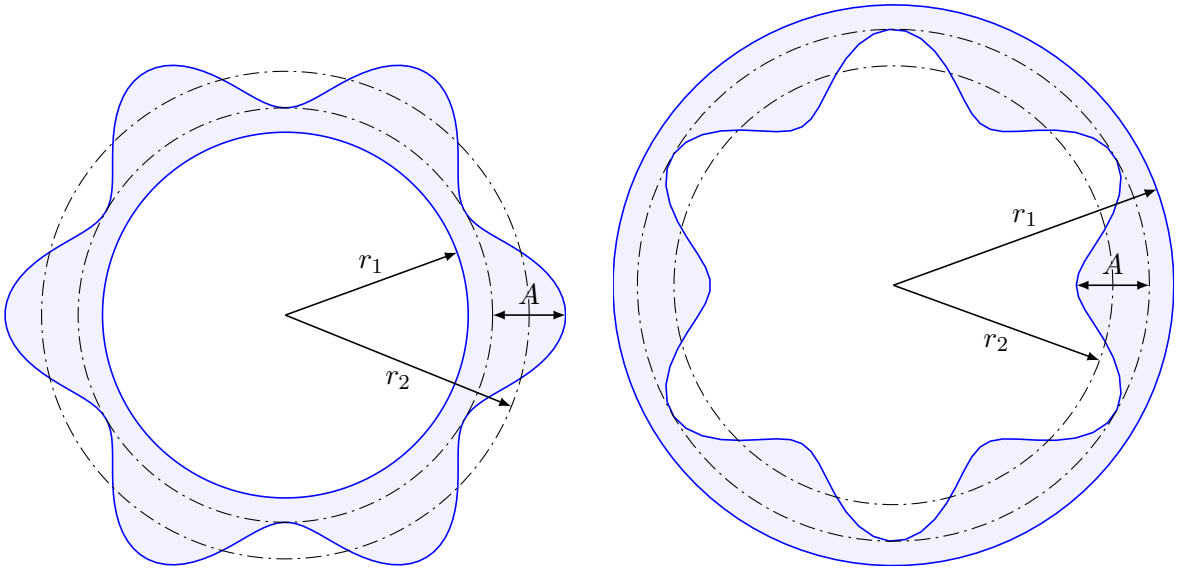

(a) Obstruction with external lobes. (b) Obstruction with internal lobes.

Figure 6.1 Obstruction geometry for $L = 6$.

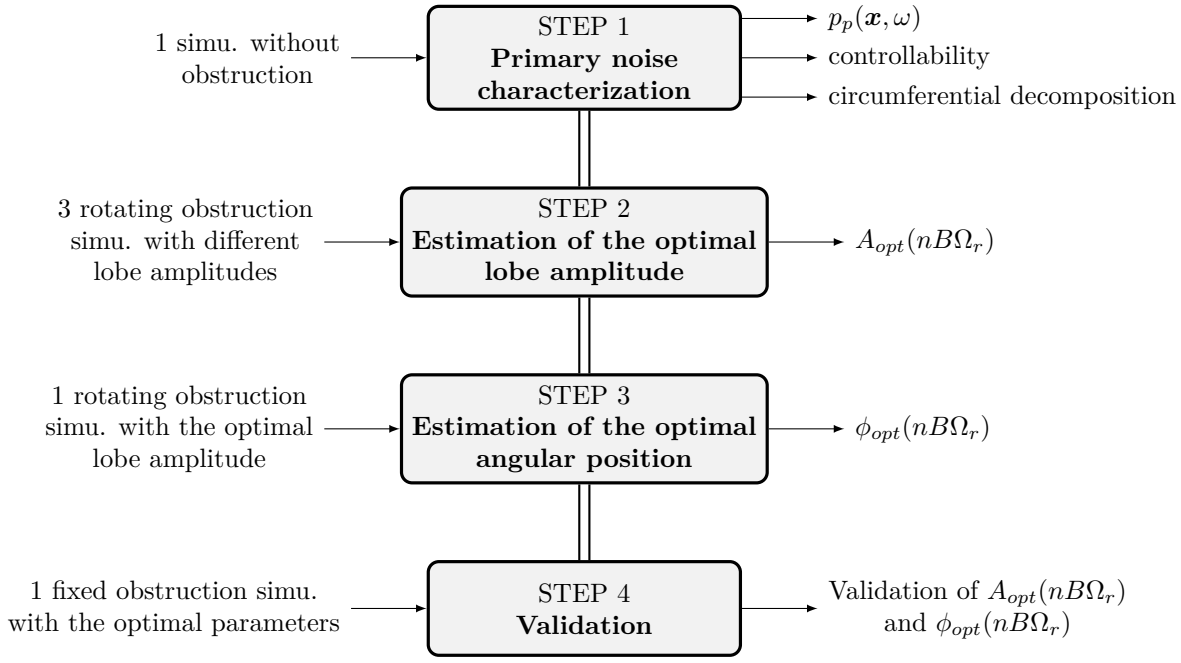

Figure 6.2 Overview of the numerical methodology.

(upstream and downstream of the fan). This step corresponds to the simulations performed in Chapter 5.

At this step, the stationarity of the primary noise can be evaluated by filtering the signal around the frequency $nB\Omega$ and plotting the temporal fluctuations of the Hilbert transform modulus. The stability of the Hilbert transform modulus appears to be a good indicator of the fan controllability [Magne *et al.*, 2014].

Additionally, the mean velocity and pressure fields on a plane upstream or downstream of the fan may be computed. Although this post-processing is not essential for the present methodology, the decomposition of these fields in circumferential modes gives a useful information on the modes responsible for the acoustic radiation. It should be noted that the plane location, the quantity, and the frame of reference in which this quantity is averaged depend on the expected noise mechanisms in the studied configuration:

— For a flow distortion upstream of a rotor, the velocity is time averaged in the absolute frame of reference on a plane close to the rotor leading edge.
— For a rotor-stator wake interaction, the velocity is averaged in the rotor frame of reference on a plane close to the stator leading edge.
— For the stator potential effect on the rotor, the static pressure is averaged in the absolute frame of reference on a plane close to the rotor trailing edge.

Step 2: Estimation of the optimal lobe amplitude

A rotating obstruction is added to the baseline setup (fan alone) and three simulations are performed with different lobe amplitudes A. The computations may be run simultaneously. However, sequentially performing the simulations allows a better adjustment of the lobe amplitude to get closer to the optimal value.

The obstruction rotates at the speed Ω_o in the opposite direction of the rotor; hence it creates a secondary tone at the frequency $\omega = \mathrm{BPF} + \mathrm{LPF} = nB(\Omega + \Omega_o)$, where LPF is the lobe passing frequency. As mentioned in the assumptions (Section 6.1.1), the obstruction speed must be slow enough to assume a quasi-static flow, typically 1 revolution per second. Since the tones of the primary and secondary sources are separated in the acoustic spectrum, the secondary source level $\log_{10}|p_s(\boldsymbol{x}, nB(\Omega + \Omega_o)|$ can be extracted without filtering.

The secondary source level is then plotted as a function of the lobe amplitude and the linear regression is computed (Figure 6.3). Finally, the optimal lobe amplitude $A_{opt}(\boldsymbol{x}, nB\Omega)$ is extracted from the same figure as it corresponds to the primary noise level $\log_{10}|p_p(\boldsymbol{x}, nB\Omega)|$.

At this point, the optimal lobe is obtained for each location $\boldsymbol{x}$. Although the result should not differ greatly from a location to another, an average over several locations can be computed to obtain the global optimal lobe amplitude $A_{opt}(nB\Omega)$.

Step 3: Estimation of the optimal angular position

Using the optimal lobe amplitude $A_{opt}(nB\Omega)$ determined at Step 2, an additional simulation is performed with the obstruction in rotation. If $A_{opt}(nB\Omega)$ happens to be one of the lobe amplitudes computed at Step 2, the estimation of the optimal angular position is simply extracted from the numerical data obtained at the previous step.

Step 3 of the optimization process is based on the time fluctuation of the total amplitude level $|p_t(\boldsymbol{x}, nB\Omega)|$ which is the combination of the primary and secondary sources. To extract $|p_t(\boldsymbol{x}, nB\Omega)|$ as a function of the angular position ϕ (Figure 6.4), the time recorded signal at the location $\boldsymbol{x}$ is first filtered on a bandwidth which includes the tones at the frequencies $nB\Omega$ (primary noise) and $nB(\Omega + \Omega_o)$ (secondary source). The Hilbert transform modulus of the filtered signal is then computed, giving the total amplitude level $|p_t(\boldsymbol{x}, nB\Omega)|$. Since the obstruction has an angular periodicity of $2\pi/nB$, the time segments of length $\Omega_o/(nB)$ are averaged, which results in Figure 6.4.

The optimal angle $\phi_{opt}(\boldsymbol{x}, nB\Omega)$ corresponds to the minimum of the mean total amplitude level (Figure 6.4). However, this angle may differ from the optimal angle with a static obstruction due to the wake deviation induced by the rotation. For this reason, the following correction is proposed.

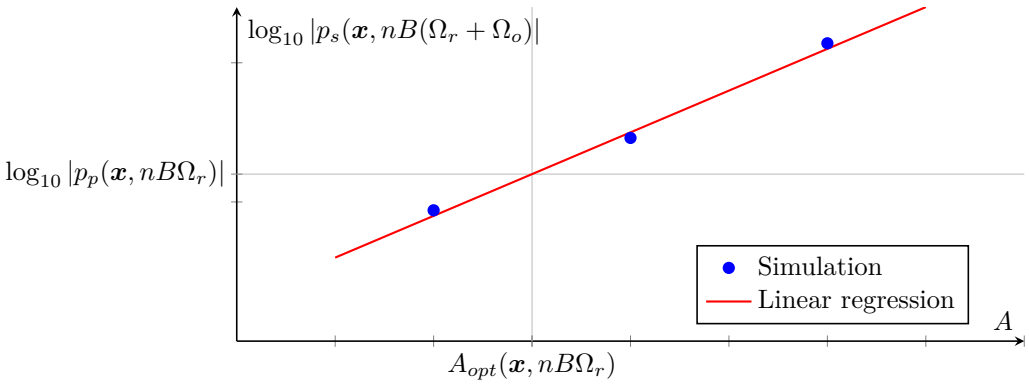

Figure 6.3 Secondary source level as a function of the lobe amplitude and its linear regression.

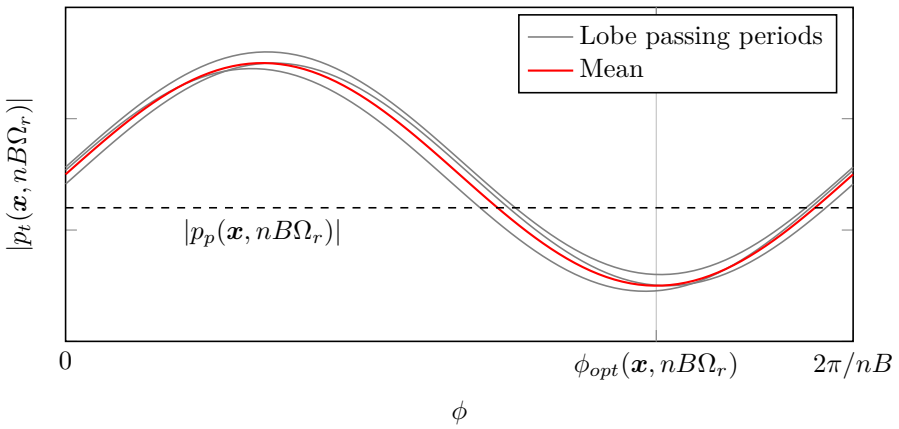

Figure 6.4 Total sound level as a function of the obstruction angular position (primary sound level is plotted as a reference to highlight the amplification and reduction zones).

Since the obstruction is in rotation, the obstruction wake angle relative to the rotation axis may be approximated by

$$\alpha = \arctan \frac{2\pi\,\Omega_o r}{V_\infty}, \tag{6.1}$$

where r is the radius position and V_∞ is the mean upstream axial velocity.[2] Additionally, for a given radius r, the angle correction Φ_c can be approximated by

$$\Phi_c = \frac{D \tan \alpha}{r}, \tag{6.2}$$

where D is the distance between the obstruction and the rotor. The angle correction is thus written

$$\Phi_c = \frac{2\pi\,\Omega_o D}{V_\infty}. \tag{6.3}$$

Therefore, the corrected optimal angle is given by

$$\phi_{opt,c}(\boldsymbol{x}, nB\Omega) = \phi_{opt}(\boldsymbol{x}, nB\Omega) - \Phi_c. \tag{6.4}$$

As for the optimal lobe amplitude, an average over several locations may be performed to obtain a global optimal angular position $\phi_{opt,c}(nB\Omega)$.

2. The pre-rotation of flow at the rotor inlet is not taken into account in this equation.

Step 4: Validation

A last simulation is performed to validate the optimal obstruction design. The obstruction is static and the design parameters are taken from Steps 3 and 4: $\phi_{opt,c}(nB\Omega)$ and $\phi_{opt,c}(nB\Omega)$.

In addition to the validation of the expected noise reduction level with the design, this step may also confirm that the angle correction Φ_c introduced at Step 3 is correct.

Overall, with a *maximum* of six numerical simulations, the proposed methodology aims at designing a flow obstruction which controls the tonal noise of a given fan, and gives an estimation of the expected noise reduction.

6.2 Numerical investigation

The numerical study of the obstruction-fan interaction was carried out on the automotive cooling fan used in the previous two chapters. The acoustic signature of the rotor alone was found to be dominated by a subharmonic tonal noise created by backflow vortices (Chapter 4). Since this noise could not be controlled with a *static* obstruction, the radiation at the BPF was enhanced by adding a stator downstream of the rotor (Chapter 5). The additional aeroacoustic mechanisms were highlighted by two methods: a direct acoustic prediction with the LBM solver *PowerFLOW*, and a hybrid method using a *Turb'Flow* unsteady RANS simulation to feed a FW-H acoustic analogy computed by *FoxWHawk*. This allowed the characterization of the primary noise radiated by the fan which corresponds to Step 1 of the proposed methodology (see Figure 6.2).

The purpose of this canonical study is to: (1) give a better understanding of the aeroacoustic mechanisms responsible for the tonal noise reduction with a flow obstruction; (2) apply and validate the numerical methodology to design an optimal flow obstruction which was introduced in Section 6.1.

6.2.1 Simulation setups

As stated above, the configuration and the fan geometry were the same as for the rotor-stator computations (see details in Section 5.1). The fan was placed in a short duct, and the operation point matched the design condition of the rotor (2500 m^3/h and 2500 rpm).

Numerical results without an obstruction showed a strong noise at the BPF. The obstructions were therefore chosen to control the tonal radiation at this frequency ($n = 1$), and the number of external lobes was equal to the number of rotor blades ($L = B$). The inner

radius corresponded to the rotor hub radius ($r_1 = 70$ mm) and the thickness of the base ($r_2 - A/2 - r_1$) was set to 10 mm. The magnitude of the secondary source was adjusted by varying the lobe amplitude A, while the obstruction-fan distance remained constant (50 mm between the obstruction and the rotor leading edge). The reference angular position $\phi = 0°$ was arbitrarily chosen when the obstruction lobes were aligned with the stator vanes at mid-lobe radius r_2.

Turb'Flow

The *Turb'Flow* simulation was based on the rotor-stator setup (see Section 5.2.1). The multi-block structured mesh was modified to include the obstruction geometry. The use of a non-collocative interface [3] between the obstruction and the rotor reduced the number of points and the mesh complexity. The final mesh contained 9.3 million nodes (17 % more points than the rotor-stator configuration). The simulation was performed on 144 cores, giving a speed of 172 h/BPP (equivalent to 1035 days/BPP on a single core) on the Mammoth Series II cluster (see technical properties in Appendix B).

Considering the *Turb'Flow* computational time shown in Chapters 4 and 5, only one simulation with a static obstruction could be performed. The lobe amplitude A and the angular position ϕ were set to 30 mm and 0°, respectively.

PowerFLOW

The *PowerFLOW* simulations were also based on the rotor-stator setup (see Section 5.2.2). The only differences lay in the addition of the obstruction geometry. The finest refinement volume was extended upstream to include the obstruction, and a new rotating interface was set around the obstruction.

Since the plug was shown to be the optimal device to control the operating point (see Section 5.4), the computations with an obstruction were performed in this configuration. The mesh totalized 81.5 M cells, which led to a simulation speed of 77 min/BPP on 240

3. A non-collocative interface inside a computational mesh separates two domains with non-coincident nodes at the boundary.

Table 6.1 Solver performances for simulations with an obstruction.

	Cells	Cores	Time/BPP	Time/BPP for 1 core
Turb'Flow (URANS)	9.3 M	144	172 hr	1035 days
PowerFLOW (LBM)	81.5 M	240	77 min	13.8 days

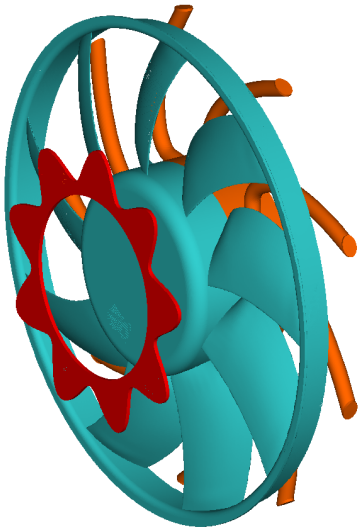

Figure 6.5 Fan and obstruction geometry: obstruction in red with a 30-mm lobe amplitude, rotor in blue, and stator in orange.

cores (equivalent to 13.8 days/BPP on a single core) on the Mammoth Parallel II cluster (see technical properties in Appendix B).

The relatively low computational cost allowed a complete numerical investigation of the design methodology. Five simulations with a rotating obstruction were performed: one computation with a lobe amplitude $A = 30$ mm at the angular speed $\Omega_o = 300$ rpm; and four computations with $A = 20$ mm and the rotational speeds $\Omega_o = 30$, 60, and 120 rpm. Additionally, eight simulations were carried out with a static obstruction ($A = 20$ mm) at various angular positions to validate the results in rotation.

6.2.2 Convergence study

The convergence of the simulations was checked by monitoring the flow rate and the pressure rise across the fan.

In the *Turb'Flow* simulation (Figure 6.6), flow rate and pressure oscillations are still visible after four fan revolutions, but they are regular after two revolutions. These fluctuations at the frequency $S_1 = 245$ Hz are the result of a pressure wave created at the initialization of the computation and reflected at the duct extremities. Since more than a year was necessary to reach the current state of the simulation, a better convergence could not be achieved. The *Turb'Flow* results presented in this chapter were thus processed from data collected after one fan revolution.

The convergence of the *PowerFLOW* simulation with a static obstruction is presented in Figure 6.7 – all the other simulations showed the same flow rate and static pressure evolution. As with the rotor-stator configuration (see Section 5.4.1), converged flow conditions are obtained after ten fan revolutions, and stabilized results are even achieved after five revolutions. The aerodynamic and acoustic results presented in this chapter were thus processed from data collected after the end of the transient period.

6.2.3 Fan performance

As in the experiments, the pressure rise across the fan was measured between the inside duct wall, 150-mm downstream of the stator plane, and the ambient pressure. The numerical and experimental results are reported in Table 6.2.

The *Turb'Flow* and *PowerFLOW* predictions are in good agreement with the experiment, showing a maximum of 4-% difference with an obstruction lobe amplitude $A = 30$ mm. Additionally, the performance loss caused by the obstruction upstream of the fan is well predicted by *PowerFLOW* and slightly overestimated by *Turb'Flow*.

These results confirm the relatively small influence of the obstruction on the fan performance (3%-loss for $A = 20$ mm) and are coherent with the previously reported predictions [Gérard *et al.*, 2009a; Magne *et al.*, 2013].

6.2.4 Obstruction-fan interaction

Numerical simulations are a great way to analyze physical phenomena which are difficult to measure or visualize experimentally. In the case of the obstruction-fan interaction, the flow topology and the wall-pressure fluctuations extracted from the computations provided important information which had never been captured by experimental studies.

Table 6.2 Fan performance.

	Turb'Flow (URANS)		*PowerFLOW* (LBM)		Experiment	
	ΔP_{wall} [Pa]	Loss [%]	ΔP_{wall} [Pa]	Loss [%]	ΔP_{wall} [Pa]	Loss [%]
No obs.	291	-	288	-	297.4	-
$A = 20$ mm			279	3.1	287.1	3.4
$A = 30$ mm	272	6.5	273	4.8	284.6	4.3

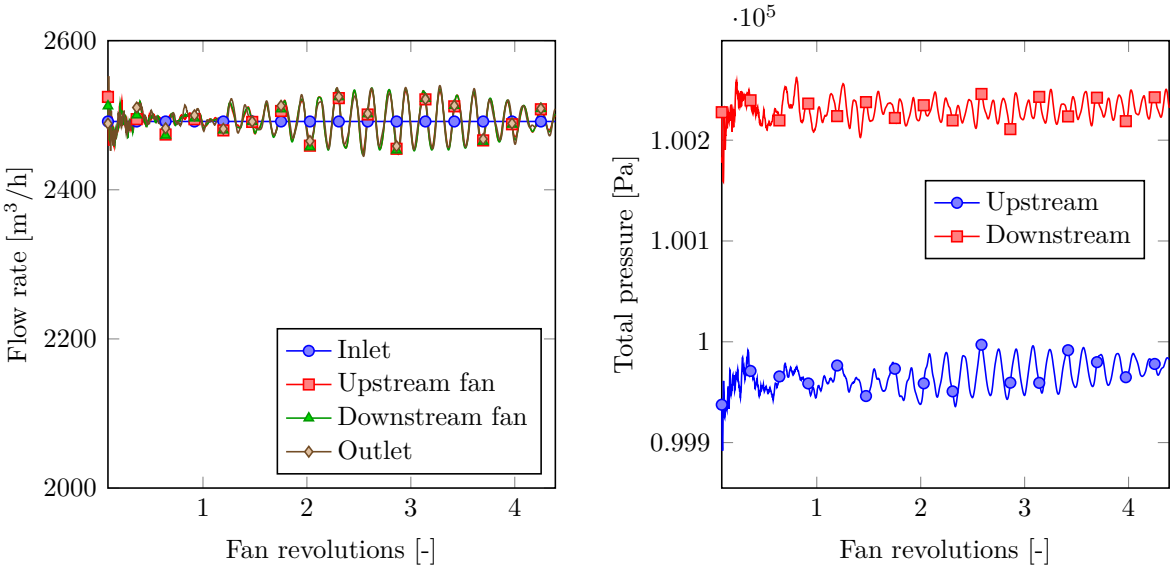

(a) Flow rate. (b) Pressure rise across the fan.

Figure 6.6 *Turb'Flow* (URANS) convergence.

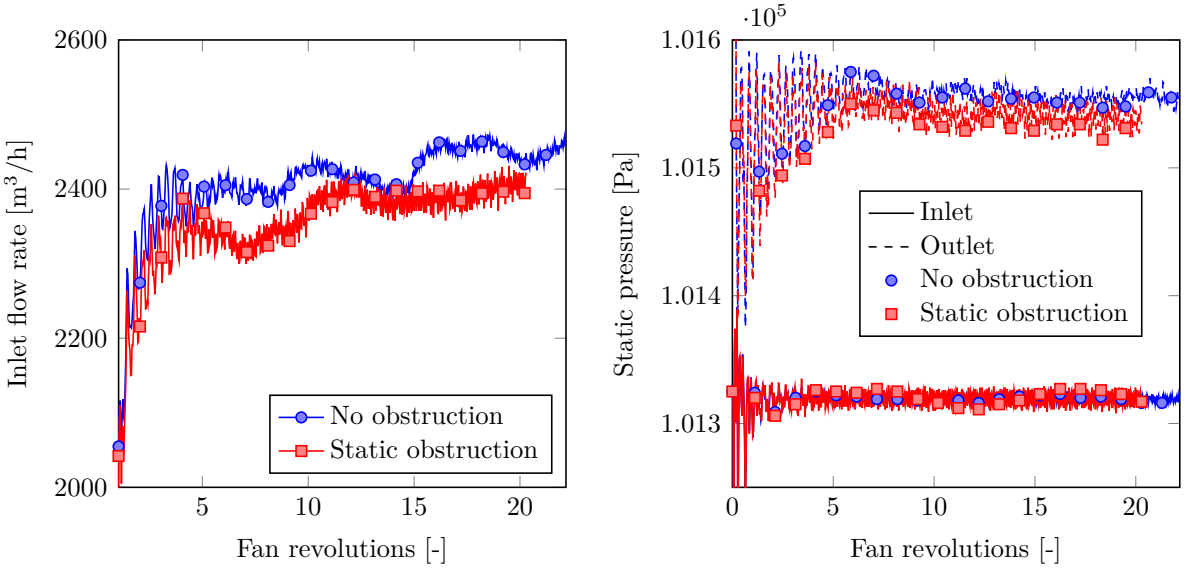

(a) Inlet flow rate. (b) Static pressure.

Figure 6.7 *PowerFLOW* (LBM) convergence.

Flow topology

The vortex structures in the simulations with a static obstruction ($A = 30$ mm) are presented in Figure 6.8 for the two solvers. Both methods predict a similar flow topology. Large backflow vortices are observed near the rotor ring, as it was the case in the simulations without an obstruction (see Figure 5.10). However, two coherent structures per blade passage are predicted by the *Turb'Flow* simulation when only one structure was observed previously. As for the obstruction wake, both simulations highlight vortex rings formed around the lobes and convected downstream to the fan blade. This aerodynamic phenomena creates a velocity deficit downstream of the obstruction lobes and therefore generates a non-uniform circumferential velocity profile. Similarly to a stator-rotor interaction, this azimuthal non-uniformity induces a periodic fluctuation of the blade load and thus an additional tonal noise source.

This observation is confirmed by the velocity field at mid-lobe radius presented in Figure 6.9 for a static and a rotating obstruction. A large velocity deficit is formed downstream of the obstruction lobe, which creates a non-uniform velocity profile in the rotor plane. Moreover, it should be noted that the obstruction rotation generates a deviation of the lobe wakes with respect to the rotating axis (see white arrow in Figure 6.9c). This confirms the need to correct the obstruction angular position when post-processing the acoustic data obtained with a rotating obstruction, as it was proposed in Section 6.1.2 (see the angle correction Φ_c defined in Equation (6.3)).

The correction angle Φ_c was estimated in the simulation from the deviation angle α for several obstruction rotational speeds Ω_o. Figure 6.10 presents the results compared with the theoretical correction angle calculated from Equation (6.3). An excellent agreement is found, confirming the validity of the angle correction introduced in Section 6.1.2.

Acoustic source locations

The wall pressure fluctuations at the BPF confirm the previous statements (Figure 6.11).

On the rotor (Figure 6.11a), the high fluctuation spot at the blade leading edge near the ring is similar to what was observed with the rotor-stator configuration (see Figure 5.17). However, an additional acoustic source is located in the lower half of the blade. This dominant source is generated by the interaction between the obstruction lobe wakes and the rotor.

On the stator (Figure 6.11b), the sources are also affected when compared with the numerical results without an obstruction. The same sources caused by the rotor wakes are

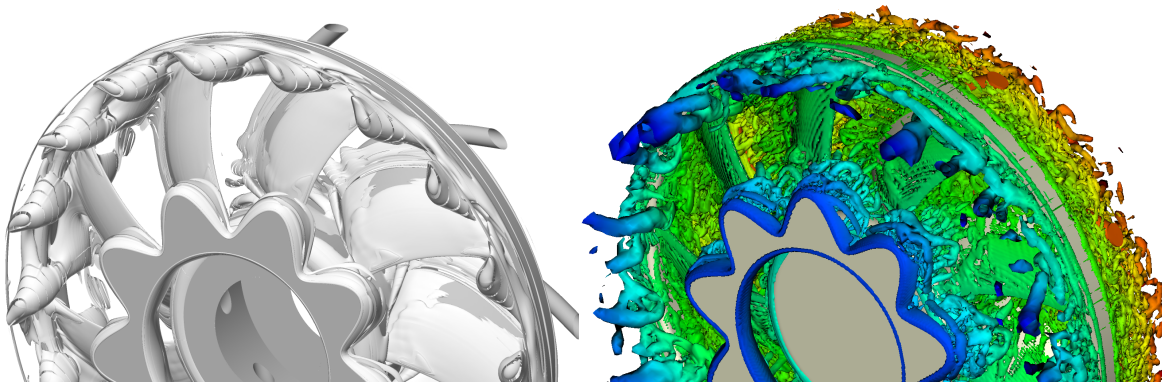

(a) *Turb'Flow* (URANS, Q-factor). (b) *PowerFLOW* (LBM, λ_2 colored by the axial position).

Figure 6.8 Visualization of the vortex structures in the simulations with a static obstruction ($A = 30$ mm).

found in the upper half of the vanes, but an additional source is present in the lower half. After being chopped by the rotor, the obstruction wakes are thus convected downstream to create a significant acoustic source on the stator.

The pressure fluctuations on the obstruction surfaces show much smaller amplitudes (Figures 6.11c and 6.11d), presumably created by the rotor potential effect on the downstream side of the obstruction. The noise sources located on the obstruction are negligible in comparison with the sources on the fan. Therefore, the obstructions are not only acoustically transparent (negligible diffraction), but they also do not generate significant noise themselves.

Source contributions to far-field noise

In the *Turb'Flow* simulation, a FW-H analogy is used to propagate the acoustic sources in the far field. Unlike a direct acoustic propagation, this hybrid method allows the separation of different surface contributions to the far-field noise.

The sound power spectrum predicted from the *Turb'Flow* simulation with a static obstruction ($L = 30$ mm, $\phi = 0°$) is shown in Figure 6.12. The separate contributions of the rotor, the stator, and the obstruction are presented along the total frequency spectrum.

Compared with the acoustic spectrum without an obstruction (Figure 5.19), the radiation at the BPF shows an 8-dB amplification, which confirms the effect of the obstruction at this frequency but indicates that the obstruction design and position are not optimal. As predicted from the wall-pressure fluctuations, the obstruction contribution appears to be negligible relatively to the rotor and stator contributions.

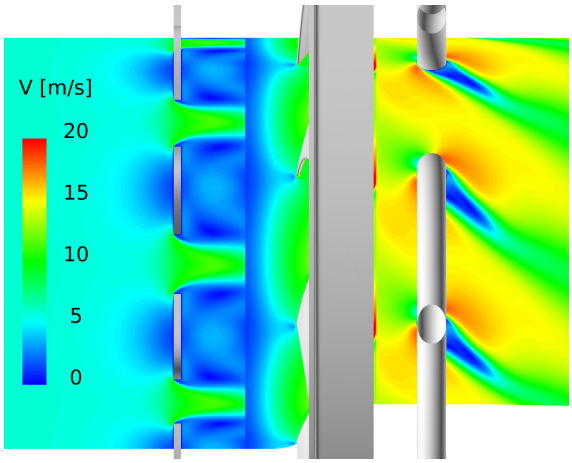

(a) *Turb'Flow* (URANS) result with a static obstruction (mean velocity magnitude).

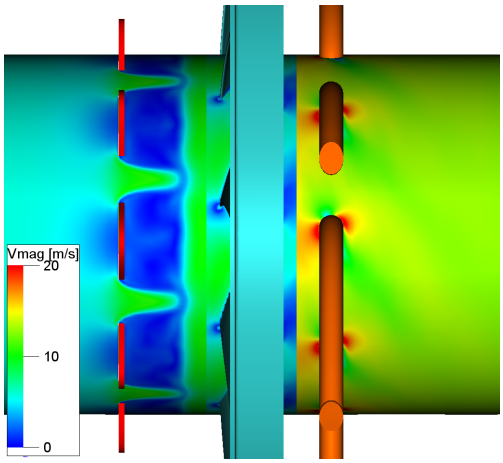

(b) *PowerFLOW* (LBM) result with a static obstruction (mean velocity magnitude).

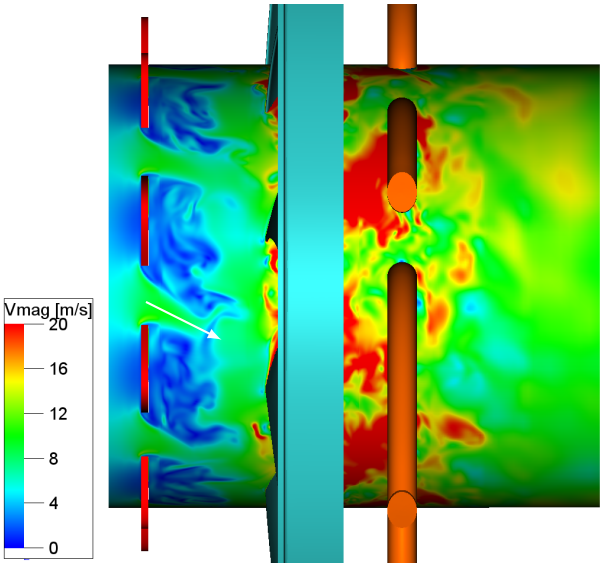

(c) *PowerFLOW* (LBM) result with a rotating obstruction ($\Omega_o = 300$ rpm, instantaneous velocity magnitude). The white arrow shows the wake deviation.

Figure 6.9 Velocity magnitude at mid-lobe radius $r_2 = 87.5$ mm ($A = 30$ mm).

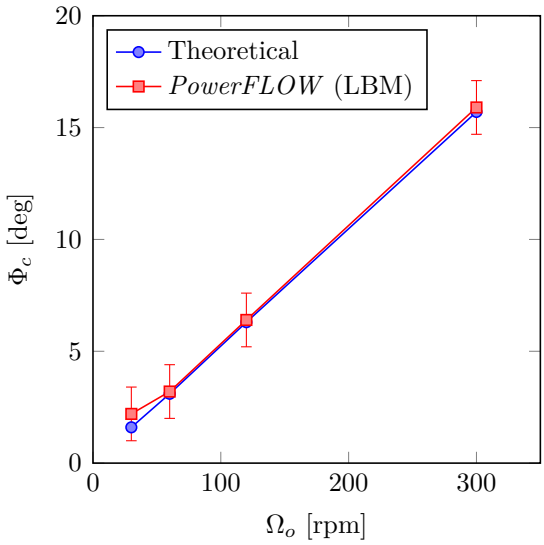

Figure 6.10 Correction angle Φ_c as a function of the obstruction rotational speed: theoretical angle from Equation (6.3) and estimation from wake deviation in *PowerFLOW* visualizations.

Q-factor visualizations highlighted that the backflow vortices are differently structured in presence of an obstruction (see Section 6.2.4). Two coherent structures are observed per blade passage, which translates into a strong radiation at the frequency H_2 (frequency of interaction between the backflow vortices and the rotor blade).

Two energetic tones at the frequency $S_1 = 245$ Hz and its third harmonic S_4 are also observed. This noise is the result of the transient pressure wave identified in the convergence study (see Section 6.2.2). Since the wave passes through all the simulation domain, all the surfaces contribute to this acoustic radiation.

Despite the absence of this spurious wave in the *PowerFLOW* simulations, results with this solver exhibit a similar acoustic signature (Figure 6.12). The tonal noise prediction is in relatively good agreement with *Turb'Flow*, showing a 6- and 4-dB difference at the BPF and its fist harmonic, respectively (Table 6.3). Moreover, the subharmonic radiation caused by the backflow interaction with the rotor is also visible, but the lower levels at the frequencies H_1 and H_2 confirm that the vortices are less coherent in the *PowerFLOW* computation (see visualizations in Figure 6.8).

Although the *Turb'Flow* simulation was used to further investigate the obstruction-fan interaction, the high computational cost ruled out the use of this code to validate the numerical methodology presented in Section 6.1. Only *PowerFLOW* results are thus presented in the rest of this chapter.

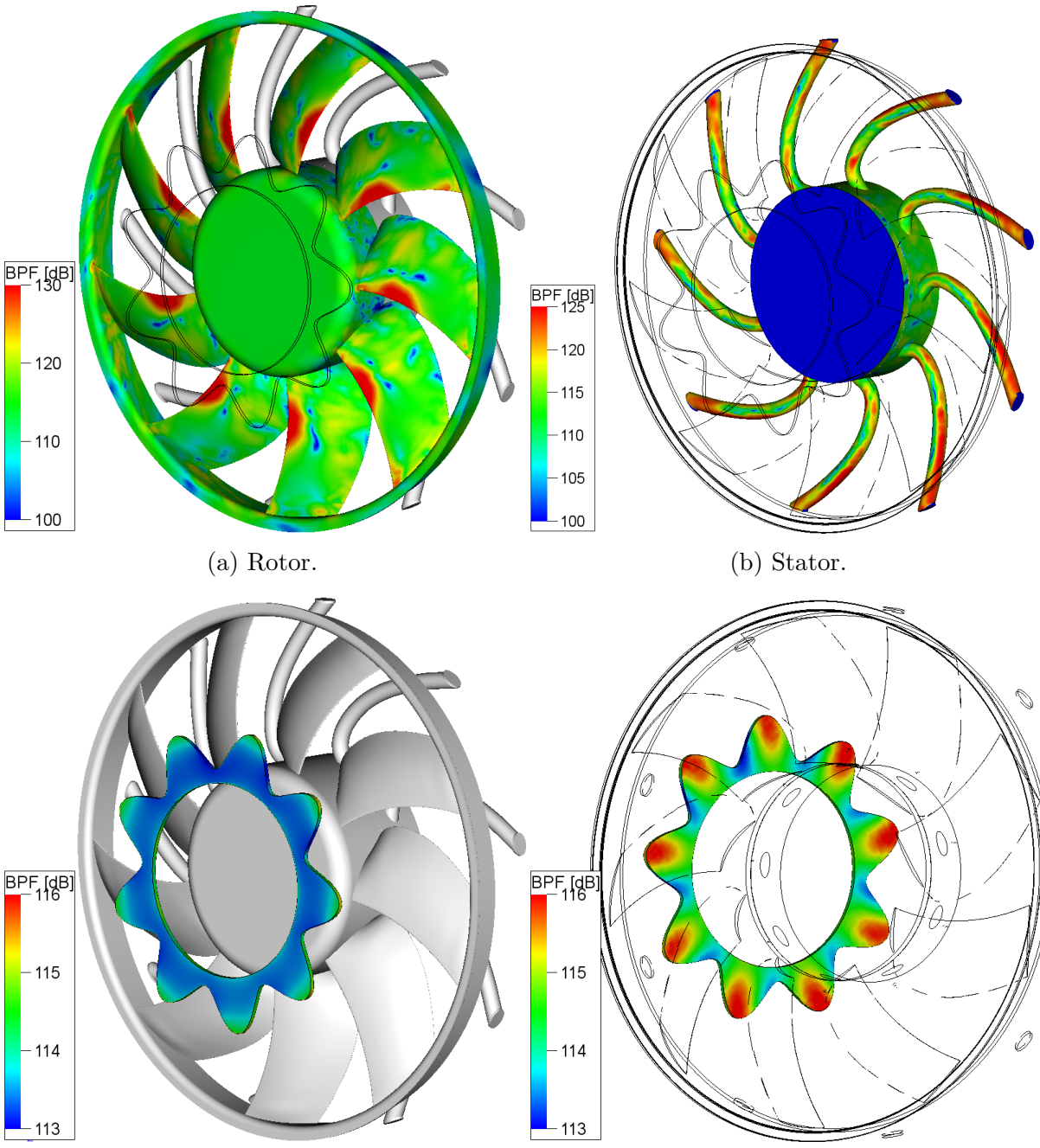

(a) Rotor.

(b) Stator.

(c) Obstruction (upstream side).

(d) Obstruction (downstream side).

Figure 6.11 Sources localization in the *PowerFLOW* (LBM) simulation with a static obstruction (static pressure fluctuations at the BPF on the solid surfaces).

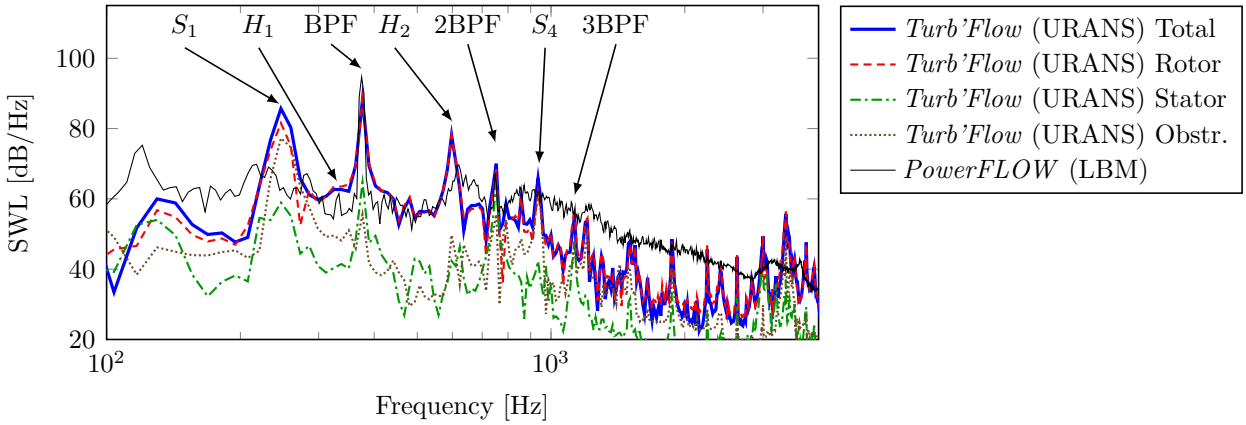

Figure 6.12 Sound power level with a static obstruction ($A = 30$ mm, $\phi = 0°$).

Table 6.3 Comparison of the sound power level at different frequencies.

	BPF [dB]	2×BPF [dB]	H_1 [dB]	H_2 [dB]
Turb'Flow (URANS)	88	71	64	78
PowerFLOW (LBM)	94	67	61	69

6.2.5 Numerical design of the obstruction

After presenting a detailed study of the obstruction-fan interaction, the design methodology is validated using *PowerFLOW*.

Estimation of the optimal lobe amplitude

As detailed in Section 6.1.2, the optimal lobe amplitude is estimated by performing simulations with rotating obstructions.

The first simulation was performed prior to the experiments. Therefore, the lobe amplitude A and the obstruction rotation speed Ω_o were arbitrarily set to 30 mm and 300 rpm, respectively. The acoustic prediction from this simulation is presented in Figure 6.13. In comparison with the rotor-stator computation, this simulation shows a similar tone amplitude at the BPF and an additional tone at the frequency BPF+LPF which corresponds to the secondary noise created by the rotating obstruction. In terms of levels, this secondary tone is higher than the BPF tone, which implies that the obstruction effect is too strong.

Consequently, a second simulation was performed with a smaller obstruction lobe amplitude ($A = 20$ mm). The rotation speed was also changed ($\Omega_o = 120$ rpm) to evaluate its influence. In this configuration, the secondary tone occurred at a lower frequency due to the smaller rotation speed, and its level was found to be the same as the level at the

BPF (see Figure 6.13). Therefore, the optimal lobe amplitude predicted numerically was $A_{opt} = 20$ mm.

Although the methodology indicated that three simulations were necessary to predict the optimal lobe amplitude (see Section 6.1.2), it should be noted that, in the present study, only two simulations sufficed. This was simply due to a serendipitous second choice of lobe amplitude.

Estimation of the optimal angular position

From the numerical results with an obstruction in rotation, the post-processing described in Section 6.1.2 was used to extract the total amplitude level $|p_t|$ as a function of the angular position ϕ. Figure 6.14 presents the BPF amplification ($|p_t| - |p_p|$) as a function of the corrected angular position ϕ_c which takes into account the angle correction introduced in Equation (6.3). Four different obstruction speeds are presented ($\Omega_o = 30$, 60, 120, and 300 rpm), and groups of probes are highlighted in different colors to better demonstrate the directivity effect.

A good agreement is found between the obstruction rotational speeds $\Omega_o = 30$ and 60 rpm (Figures 6.14a and 6.14b). All the probes show a similar attenuation as a function of the obstruction angular position, yielding the optimal angle $\phi_{c,opt} = 16°$.

Above $\Omega_o = 120$ rpm (Figures 6.14c and 6.14d), the greater the obstruction rotating speed is, the stronger the differences between the probes are. First, an angular shift is observed for the probes located in the rotor plane (pink). Because of the large sweep angle of the rotor blades, this shift may be caused by the different impact angle of the obstruction wake which modifies the orientation of the dipolar sources on the fan. Second, two groups of probes (blue and red) located in the outlet jet show large discrepancies. The reason of these differences is yet to be found. All these differences at higher rotational speed have a strong impact on the optimal angle prediction.

Validation of the optimal angular position

To validate the results estimated from the simulations with a rotating obstruction, eight computations with a static obstruction at different angular positions were performed. The amplitude of the BPF tone as a function of the angular position is presented in Figure 6.15. The optimal position appears to be around $\phi_{opt} = 15°$, which is in excellent agreement with the prediction from the simulation in rotation (16°). Moreover, the acoustic reduction at the BPF is similar to the one predicted with a rotating obstruction. Finally, since the noise attenuation is identical for all the microphones, a similar reduction of the sound

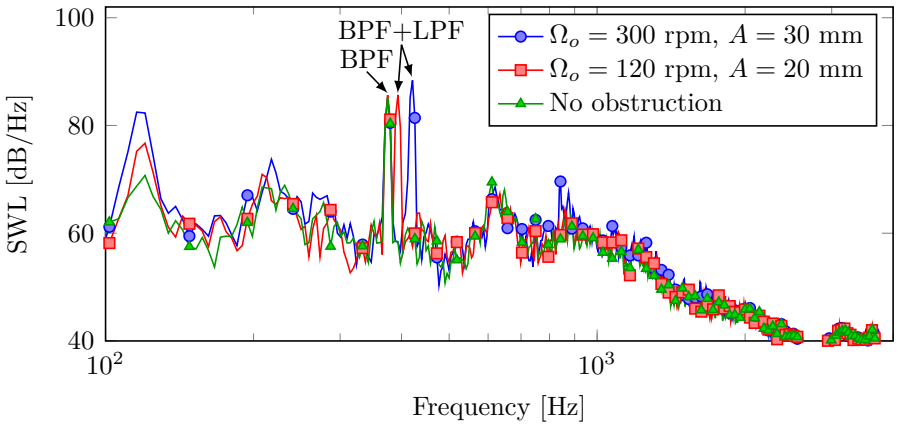

Figure 6.13 Comparisons of sound power levels for two simulations with a rotating obstruction and the simulation without obstruction. *PowerFLOW* (LBM) solver.

power level is expected. In this configuration, the obstruction does not show a significant directivity effect.

Overall, this study demonstrated the ability to capture numerically the aeroacoustic phenomena responsible for the tonal noise reduction, and showed the potential of the proposed methodology. These results are compared with measurements in the following section.

6.3 Experimental study

The experimental analysis aims at validating the numerical results and further investigate the methodology. Since *Turb'Flow* could not be used to validate the numerical methodology, measurements will only be compared with numerical results obtained with the LBM solver *PowerFLOW*.

6.3.1 Experimental setup

The obstructions were added to the experimental setup described in Section 5.3. They were held by aluminium rods which were connected to a step motor (see Figure 6.16). The relatively large and heavy structure supporting these parts is visible in yellow in Figure 5.4.

The step motor controlled the obstruction angular position for measurements with static obstructions and the rotation speed for measurements with rotating obstructions. In all the tests, the obstructions had the same design parameters as in the simulations: B external lobes, $r_1 = 70$ mm (internal radius), $r_2 - A/2 - r_1 = 10$ mm (base thickness).

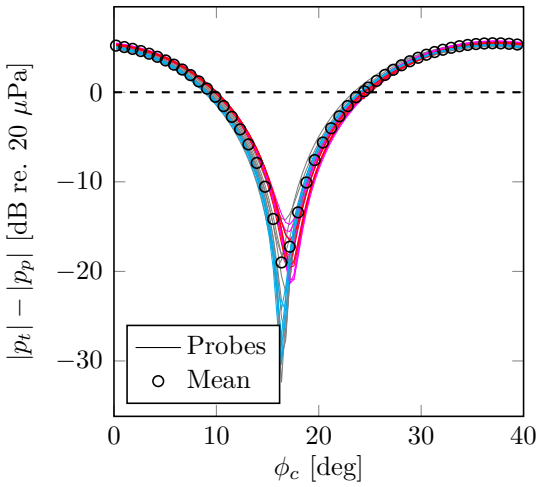

(a) $\Omega_o = 30$ rpm.

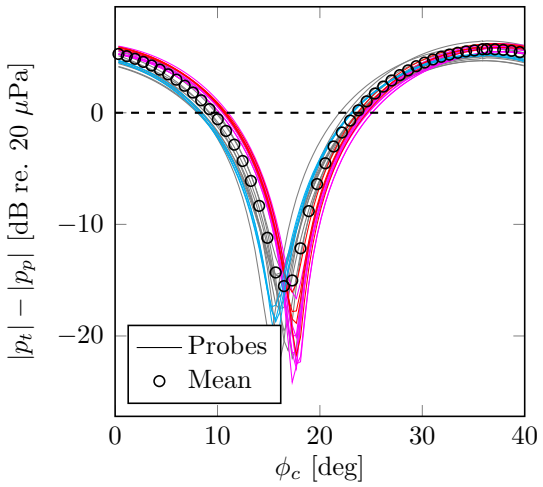

(b) $\Omega_o = 60$ rpm.

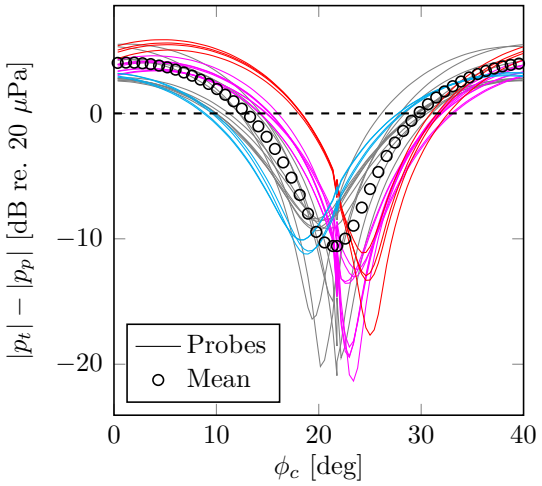

(c) $\Omega_o = 120$ rpm.

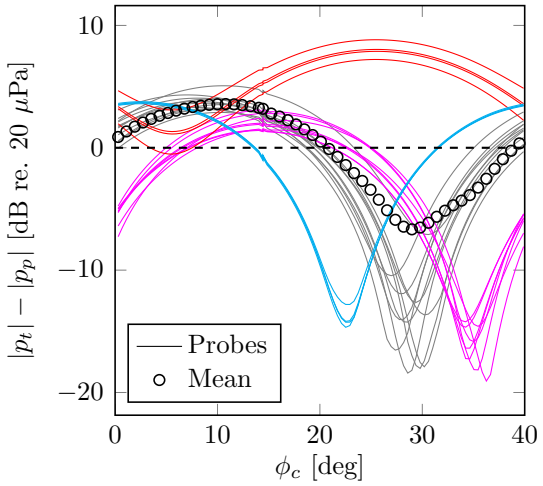

(d) $\Omega_o = 300$ rpm.

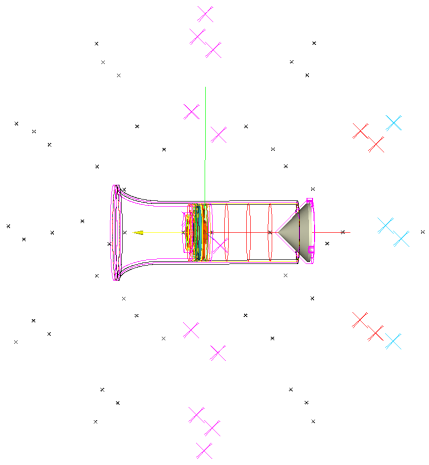

(e) Corresponding probe locations.

Figure 6.14 *PowerFLOW* (LBM) simulations with a rotating obstruction ($A = 20$ mm): BPF amplification as a function of the corrected obstruction angular position ϕ_c; solid line colors in (a), (b), (c), and (d) correspond to the probe locations in (e).

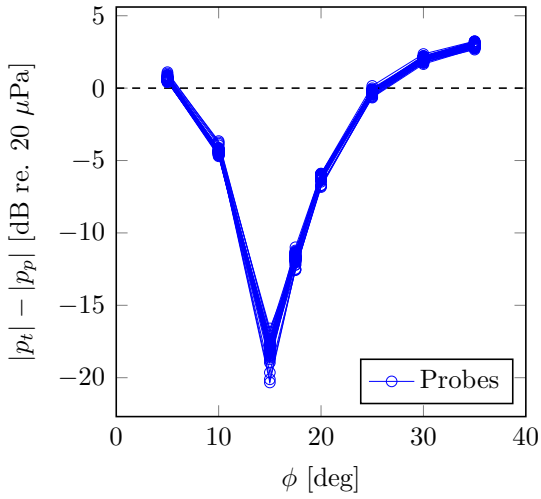

Figure 6.15 *PowerFLOW* (LBM) results with a static obstruction: BPF amplification as a function of the obstruction angular position for all the probe locations.

Aerodynamic and acoustic measurements were performed with the same equipment and acquisition parameters described in Section 5.3.

6.3.2 Aerodynamic results

The effect of the obstruction on the pressure rise is presented in Table 6.4. The compression loss due to the obstruction varies between 0.9 and 4.3 % for a lobe amplitude of 10 and 30 mm, respectively. These values are in agreement with previous studies [Magne *et al.*, 2013] and shows an excellent agreement with the numerical results presented in Section 6.2.3.

Table 6.4 Effect of the obstruction lobe amplitude A on the fan performance.

A [mm]	ΔP_{wall} [Pa]	Loss [%]
No obs.	297.4	-
10	294.8	0.9
15	289.7	2.6
20	287.1	3.4
25	285.8	3.9
30	284.6	4.3

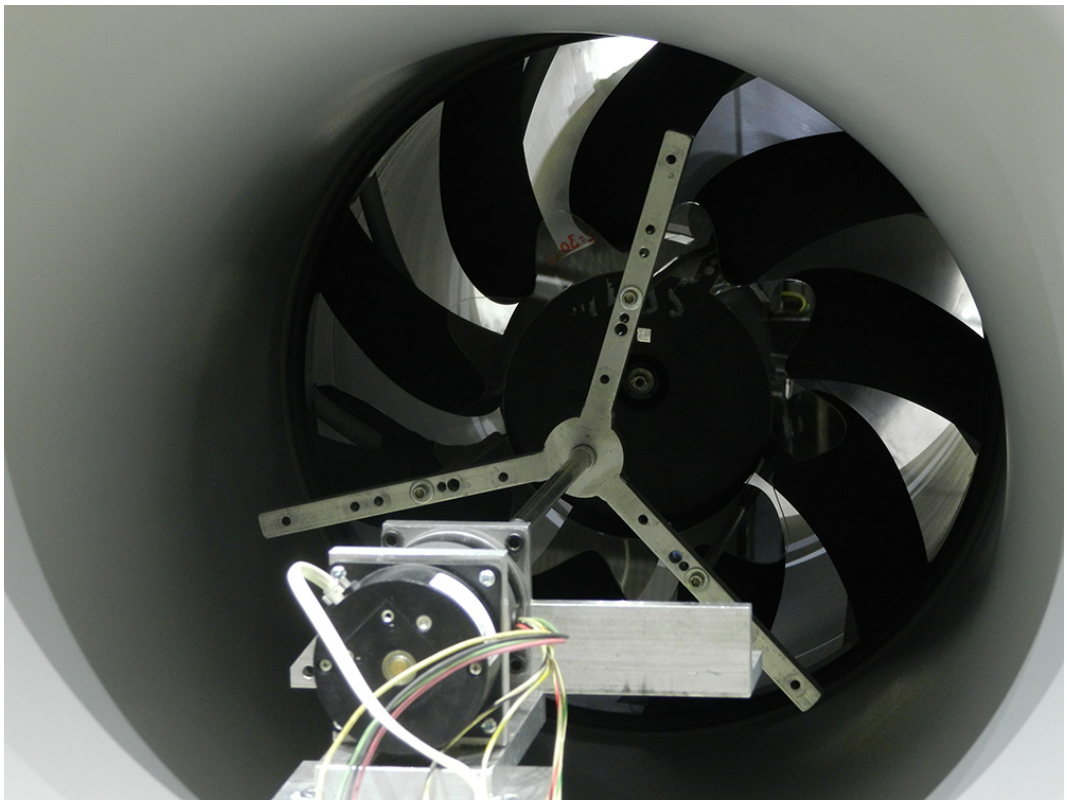

Figure 6.16 Photograph of the experimental jig holding the transparent obstruction in front of the black rotor (the step motor is visible in the foreground).

6.3.3 Acoustic results

As discussed in Section 5.4.2, the following results were obtained for the opening $l = 50$ mm which corresponds to the simulated operating point (2500 rpm, 2500 m^3/h). Since the microphone locations were chosen to study the noise directivity in the horizontal plane and in the upstream direction only, no sound power spectra could be extracted from the measurements. Comparisons with simulations were thus based on sound pressure levels.

Installation effect

Adding a relatively large structure at the inlet of a fan creates an inlet flow distortion which may have a significant impact on the acoustic spectrum and particularly on the tonal noise. Figure 6.17 presents the effect of the jig which was used to hold the obstruction in front of the fan (see the jig in front of the duct inlet in Figure 5.4). For the two microphone locations, the jig has no impact on the acoustic signature, neither on the broadband nor on the tonal noise. This confirms the low disturbance of the inlet flow and thus validates the use of the obstruction jig.

Estimation of the optimal lobe amplitude

For the estimation of the optimal lobe amplitude the obstruction was rotating at 120 rpm, which separated the secondary tone from the BPF. Therefore, the obstruction effect occurred at 393 Hz which corresponds to the addition of the blade passing frequency BPF $= B\,\Omega = 375$ Hz and the lobe passing frequency LPF $= B\,\Omega_o = 18$ Hz. The effect of the obstruction lobe amplitude is presented in Figure 6.18.

Firstly, it should be noted that the broadband noise level and the BPF amplitude are invariant (Figure 6.18a). This confirms the frequency selectivity of the obstruction. Secondly, the secondary source level varies linearly with the lobe amplitude (Figure 6.18b), which confirms one of the assumptions of the methodology (see Section 6.1.1). Finally, the optimal lobe amplitude is found to be $A_{opt} = 20$ mm, which exactly matches the numerical prediction. The same results were found for the other microphone locations (not presented here). Therefore, the numerical results presented in Section 6.2.5 are validated.

Additionally, the secondary source level predicted by *PowerFLOW* at the same location is in good agreement with the measurements (Figure 6.18b). A 2-dB difference is observed, but the numerical results follow a similar trend. However, another simulation with a different lobe amplitude would have been necessary to conclude on this statement.

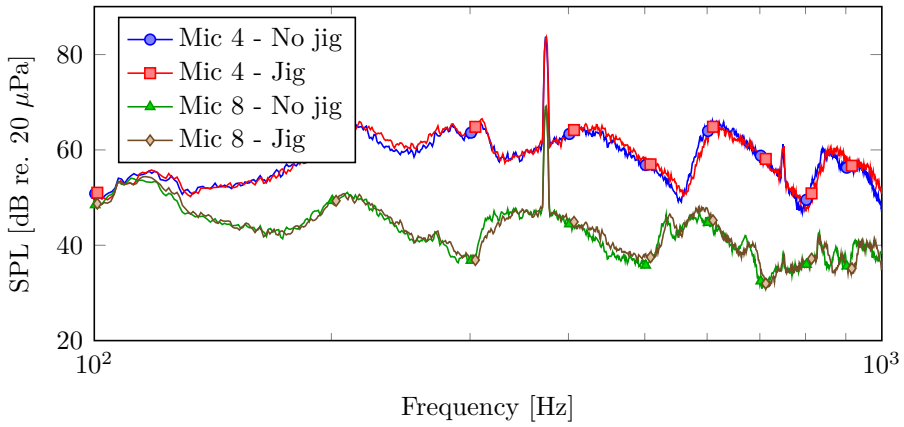

Figure 6.17 Sound pressure level measurements for the fan alone: installation effect with and without the obstruction jig (no obstruction is used); the microphone 4 is on the rotor axis, upstream of the fan, and the microphone 8 is on the rotor plane.

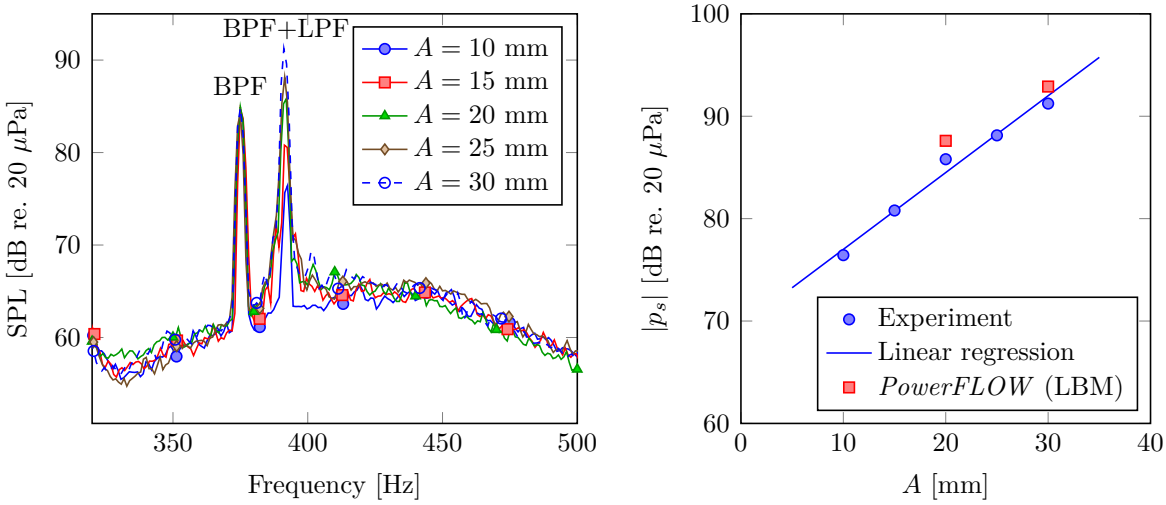

(a) Sound pressure level ($\Omega_o = 120$ rpm).

(b) Secondary source level as a function of the lobe amplitude (experimental results with $\Omega_o = 120$ rpm; *PowerFLOW* results with $\Omega_o = 120$ and 300 rpm).

Figure 6.18 Effect of the lobe amplitude with a rotating obstruction (microphone on the rotor axis, upstream of the fan).

Estimation of the optimal angular position

Following Step 3 of the methodology (see Figure 6.2), measurements with a rotating obstruction were performed. The lobe amplitude was set to the estimated optimal lobe amplitude $A_{opt} = 20$ mm.

As described in Section 6.1.2, the optimal angular position was extracted from the microphone time signals. The signals were filtered on a bandwidth which included the primary and secondary sources, then the signal amplitudes were computed from the Hilbert transform and averaged in time segments that corresponded to a lobe passing period. In the present experimental study, the rotation of the obstruction was driven by a step motor, which implied small variations of the rotating speed. As a result, an averaging based on a constant rotation speed led to time segments which were out of phase (Figure 6.19a). In order to synchronize the segments, a tachometer probe was added to the setup (Figure 6.20a). The probe signal gave a reference pulse per rotation which was used to extract the time segments, resulting in synchronized segments and a better averaging (Figure 6.19b).

In the present measurements, five obstruction speeds Ω_o are tested: 60, 80, 100, 120, and 140 rpm. Figure 6.21 presents total amplitude levels as a function of the angular position for a microphone in the rotor plane. As observed previously in the simulations (see Figure 6.9), the rotation induces a deviation of the obstruction wake. When the obstruction angle ϕ is not corrected (Figure 6.21a), the rotation speed has an effect on the optimal angular position (curve minimum) because of the wake deviation. However, Figure 6.21b shows that the angle correction Φ_c introduced in Section 6.1.2 perfectly compensates the wake deviation, resulting in similar optimal angles for all the rotation speeds. Since similar results were found for all the microphones, the angle correction was validated.

Figure 6.22 presents the noise amplification at the BPF as a function of the corrected angular position, for all the microphones. A small angular shift can be observed between the microphones in the rotor plane (1, 7, and 8) and the others. This behavior is similar to what was observed in the numerical results presented in Section 6.2.5. As shown in Figure 6.22b, a greater obstruction speed results in a larger angle shift between the two groups of microphones, which is coherent with the aforementioned hypothesis of a different angle between the obstruction wake and the rotor. Therefore, a low obstruction speed should be preferred in order to avoid this prediction dissimilarities between the microphones.

From these results, the optimal angular position (curves minimum) is found to be $\phi_{c,opt} = 14°$ in the present configuration, which is in good agreement with the numerical prediction

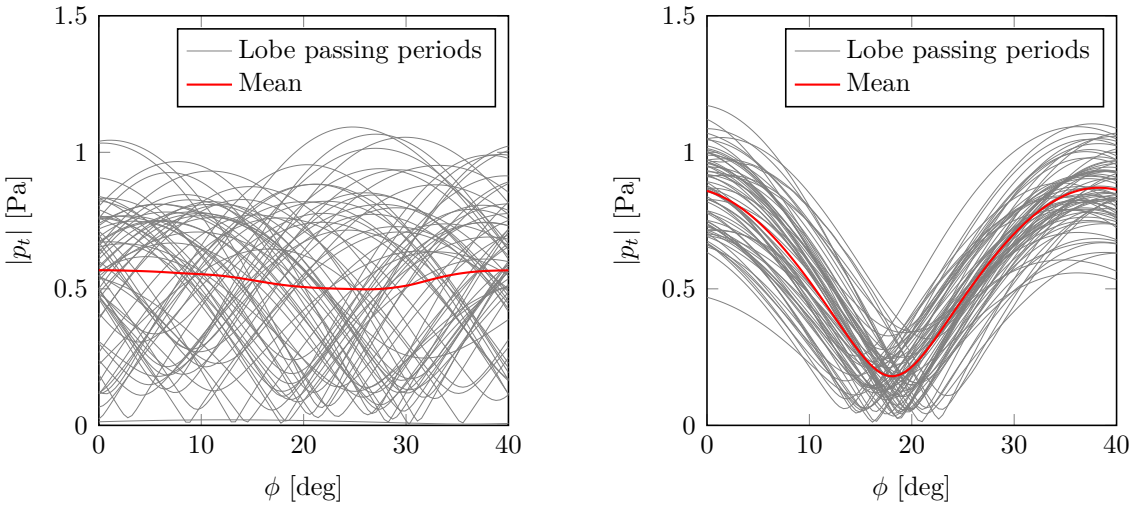

(a) Without tachometer synchronization. (b) With tachometer synchronization.

Figure 6.19 Measurements with the obstruction in rotation: effect of the tachometer synchronization for a microphone on the rotor axis.

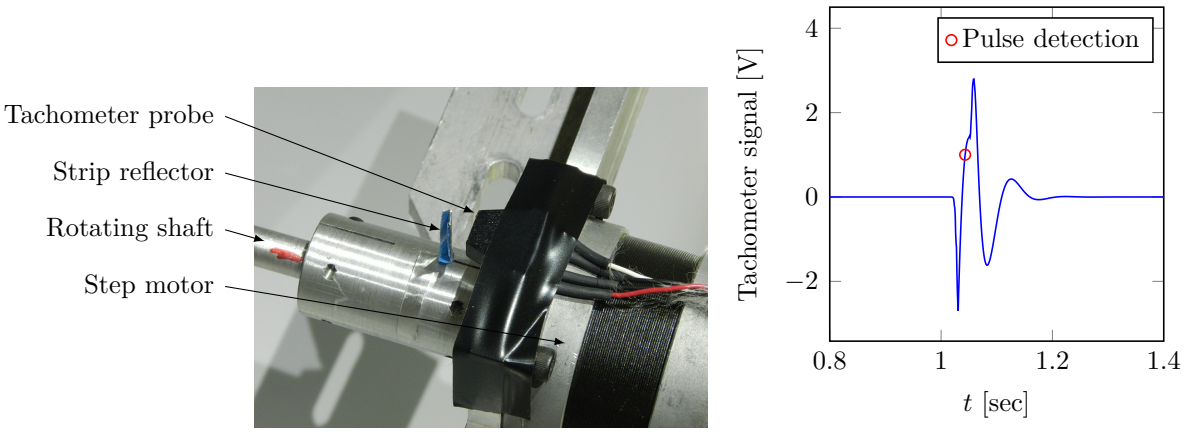

(a) Tachometer setup. (b) Tachometer signal.

Figure 6.20 Tachometer probe.

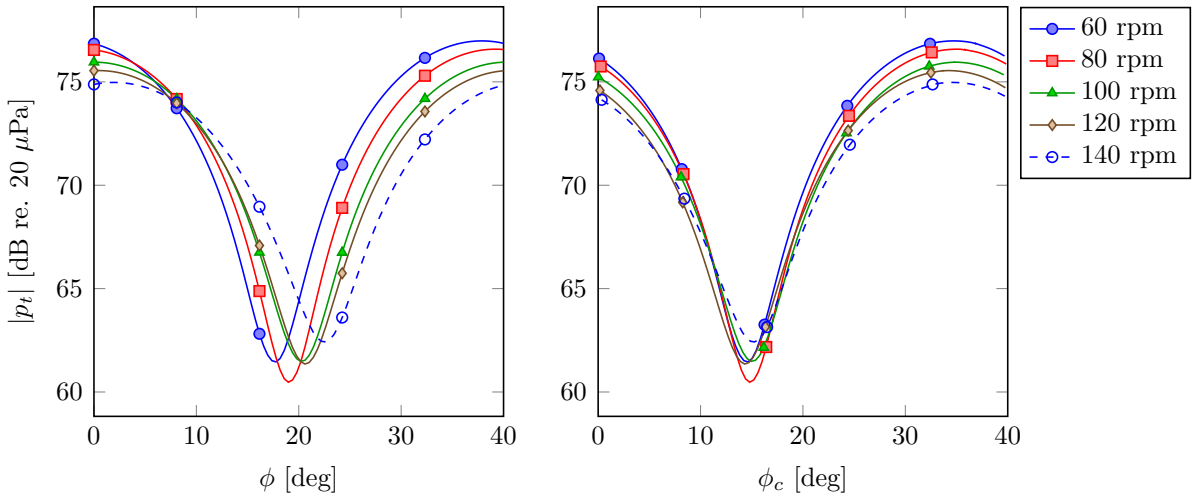

(a) Non corrected angular position ϕ. (b) Corrected angular position ϕ_c.

Figure 6.21 Measurements with a rotating obstruction: Total amplitude level as a function of the angular position for different obstruction rotation speeds Ω_o; microphone in the rotor plane.

(16°). However, the reference angle ($\phi = 0°$) is assumed to coincide with the tachometer pulse, yet the pulse detection was chosen to be as stable as possible, resulting in a detection at +1 V on a rising edge (see Figure 6.20b). Given the time between the first falling edge and the chosen detection, an error up to 6° may be observed on the reference angle. Consequently, the optimal angular position may be expected up to 20° ($\phi_{c,opt} + 6°$).

Although a tachometer was found to be essential to post-process the time signals with a rotating obstruction, its setup highlighted some issues that may induce significant discrepancies in the results. Therefore, paying meticulous attention to the tachometer setup is strongly recommended in order to extract the reference angle precisely. Alternatively, the use of a rotary encoder appears to be a better option.

Validation of the optimal angular position

Measurements with a static obstruction at different angular positions were performed to validate the optimal design. The angular position varied between 0 and 45° with a 1^circ step. The attenuation at the BPF as a function of the angular position is presented in Figure 6.23.

A similar behavior is found for all the microphones, and the curves have, as expected, a 40° periodicity ($360/L = 40°$). From these results, the optimal angular position is estimated at $\phi_{opt} = 20°$, which shows a 6° difference with prediction made with the rotating obstruction.

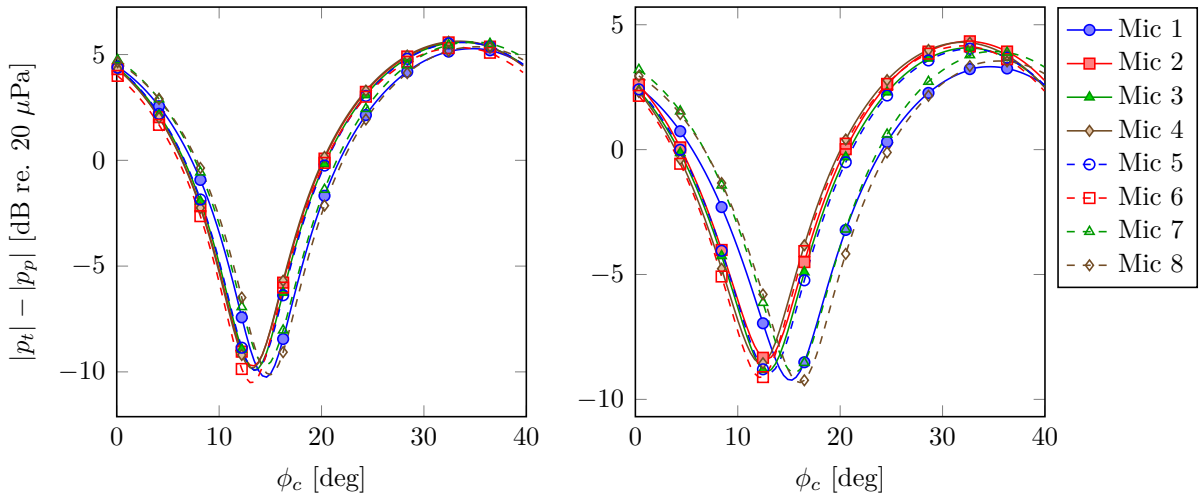

(a) $\Omega_o = 60$ rpm. (b) $\Omega_o = 140$ rpm.

Figure 6.22 Measurements with a rotating obstruction: Amplification at the BPF as a function of the corrected angular position for all the microphones.

Given the uncertainty of the reference angular position in the measurements with a rotating obstruction (see Section 6.3.3), this optimal value agrees with the previous result.

When compared with the numerical results, a 4 to 5° difference is observed with the optimal angle computed from simulations (see Sections 6.2.5 and 6.2.5). It should be noted that an additional uncertainty may come from the *visual* alignment of the obstruction in the reference position ($\phi = 0°$). This may explain the small discrepancy found between experimental and numerical results.

6.4 Conclusion

In this chapter, a complete investigation of the tonal noise control with flow obstruction has been successfully conducted.

First, an industrially-applicable numerical methodology was proposed to obtain an optimal obstruction design for a given fan geometry and operating condition. In the optimization process, simulations of rotating obstructions allow the separation of the fan and obstruction contributions to the noise (primary and secondary noise). As a result, the optimal lobe amplitude and optimal angular position can be predicted with a maximum of six simulations.

Second, two computational approaches were used to predict the noise in the far field: a hybrid method using the unsteady RANS solver *Turb'Flow* coupled with a FW-H analogy;

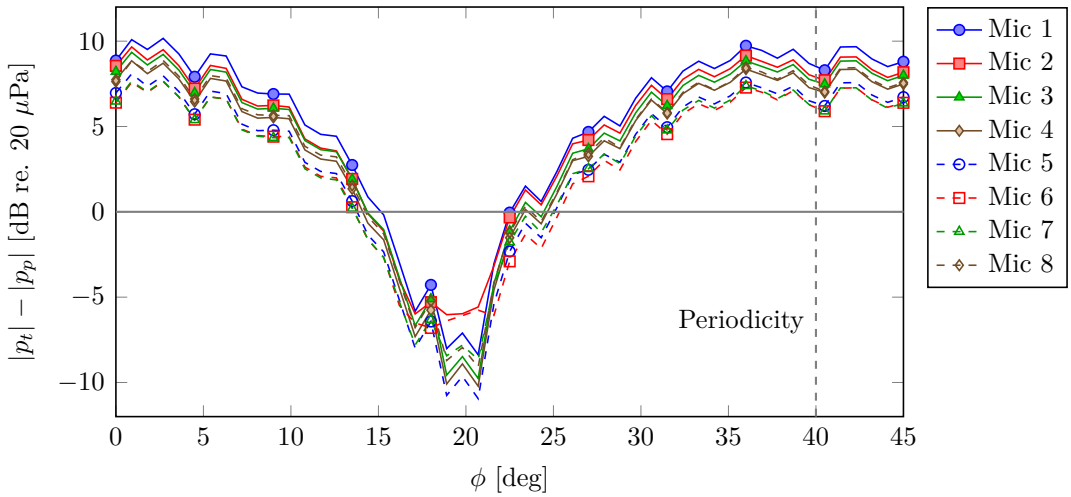

Figure 6.23 Measurements with a static obstruction: Amplification at the BPF as a function of the obstruction angular position.

and a direct acoustic propagation method using the LBM solver *PowerFLOW*. The obstruction-fan interaction was thoroughly investigated with both approaches. Simulations highlighted vortex rings formed at the obstruction lobes and convected downstream to the fan. These structures create an azimuthal variation of the velocity profile which generates a periodic fluctuation of the blade load. As a result, the main acoustic sources induced by the obstruction is located on the fan surfaces, and the radiation coming from the obstruction itself is negligible. Then, a numerical validation of the proposed design methodology was carried out. Given the computational cost associated with the *Turb'Flow* simulations, this study was only conducted with *PowerFLOW*. Two simulations with rotating obstructions sufficed to estimate the optimal lobe amplitude $A_{opt} = 20$ mm. Then four simulations at different obstruction rotational speed were performed to investigate the influence of the speed on the acoustic radiation. Results showed that strong discrepancies between the microphones appear for obstruction speeds above 60 rpm. However, simulations at the slowest speeds ($\Omega_o = 30$ and 60 rpm) were in excellent agreement, predicting an optimal obstruction angular position $\phi_{c,opt} = 16°$. Eight additional simulations with a static obstruction at different angular positions were performed to validate the optimal angular position. The optimal angle and the noise reduction were in excellent agreement with the prediction based on the the simulations with a rotating obstruction.

Finally, an experimental investigation was conducted in the fully-anechoic room of the Université de Sherbrooke. The aerodynamic and acoustic results of this study were in very good agreement with the numerical predictions. The estimation of the flow rate and the pressure rise across the fan showed that the *PowerFLOW* simulations accurately predicted

the fan performance and the loss due to the addition of an upstream flow obstruction. Additionally, the acoustic measurements were in excellent agreement with the numerical results. The broadband noise showed the same frequency modulations up to the mesh cut-off; and the tonal noise level was very well predicted, which was the most important for this study. With a rotating obstruction, the measurements performed at several speeds validated the angular correction introduced in the methodology to account for the obstruction wake deviation. Moreover, the experiments validated the methodology to design the obstruction. The excellent agreement between the numerical and experimental results showed that simulations were able to capture effectively the aeroacoustic mechanisms responsible for the primary noise, in addition to the effect of obstruction-fan interaction on the tonal noise. This led to similar predictions of the optimal lobe amplitude for the given installation and operating condition. As for the optimal angular position, the tests confirmed that the results are strongly influenced by an excessive obstruction rotation speed which leads to large discrepancies between the microphones. This validated the similar behavior observed in the simulations, which implies that the obstruction speed should be kept as low as possible. Additionally, the measurements with a rotating obstruction highlighted the high sensitivity of the reference angle detection ($\phi = 0°$) and suggested that an extra care was necessary to obtain a good estimation of the optimal angular position. The comparisons with the simulations showed a good agreement with a rotating obstruction and a small angular shift with a static obstruction.

Overall, the present study laid the foundation for future numerical investigations and for the development of industrial tools to reduce tonal noise from low-speed fans.

CHAPTER 7

CONCLUSION AND PERSPECTIVES

As presented in Chapter 2, the noise radiated by low-speed fans comes from several complex aeroacoustic mechanisms. Although broadband noise has a significant contribution to the sound power level of the fan, tonal noise creates a harsh acoustic signature and therefore is of prime interest for fan manufacturers. As a result, numerous techniques have been developed to mitigate tonal noise. Among those, the adaptive passive control with flow obstruction is a simple yet efficient method based up to now on a modification of the fan installation to create an additional acoustic source of same amplitude but opposite phase of the primary noise. Despite the research conducted on this technique, the understanding of the obstruction-fan interaction was based on simplified analytical models and far-field acoustic measurements. Consequently, the aeroacoustic mechanisms could not be clearly identified. Moreover, the optimization of the obstruction design relied on extensive experimental tests which could not be applied in an industrial context.

Using a numerical approach, the present study aimed at better understanding tonal noise control of low-speed fans with flow obstruction. Additionally, this project had for objective to develop a industrially-applicable numerical methodology in order to optimize the obstruction size and shape.

To achieve these objectives, Chapter 3 presented several computational techniques used to predict the noise radiated by a rotating machine. From the source generation to the sound propagation, each of them are tailored to a specific problem. Given the flow characteristics and the geometry of the fan, two suitable aeroacoustic methods were chosen:

- a hybrid approach combining a compressible Navier-Stokes solver, *Turb'Flow*, to compute the acoustic sources and an acoustic analogy, *FoxWHawk*, to predict the noise at different observer locations in the far field;
- a direct approach using a LBM code, *PowerFLOW*, which resolves the flow in the vicinity of the fan and propagates the acoustic waves to far-field locations.

Before applying these methods to the purpose of the thesis, the two approaches were validated on a test case – the noise radiated by the flow past a cylinder. The precision and the speed of the different codes were assessed, and the results were compared with

data found in the literature. The good agreements confirmed the validity of the acoustic predictions.

Prior to the simulation of the obstruction-fan interaction, the primary acoustic signature of a fan had to be characterized. For this purpose, Chapter 4 presented a numerical investigation of the tonal noise radiated by a low-speed ring fan in uniform inlet flow. Unsteady RANS simulations highlighted upstream vortices formed in the tip-clearance recirculation. These structures interact with the blade leading edge and, due to their own rotation, create a periodic fluctuation of the blade load at lower frequency than the BPF. Based on the wall-pressure data, the resulting subharmonic acoustic radiation was successfully predicted using a FW-H analogy in the time domain and a compact rotating dipole formulation in the frequency domain – 1 to 6-dB difference on the sound power level. However, the main radiation occurring at a different frequency than the BPF, this configuration was not suitable to study the noise reduction using static flow obstructions.

Consequently, a new configuration was developed in Chapter 5 to enhance the noise at the BPF. A stator with blunt, cylindrical vanes was placed downstream of the rotor, which created additional acoustic sources at the BPF from two mechanisms:

— the interaction between the rotor wakes and the stator which induces a periodic fluctuation of the vane wall pressure;
— the stator potential effect on the rotor which generates a periodic fluctuation of the blade load.

In addition to the computational simulations performed with *Turb'Flow* and *PowerFLOW*, an experimental mock-up was designed and built in order to validate the numerical results. To simplify the tests, the fan was placed in a short duct rather than flush-mounted on a plenum, as it was the case for the rotor alone. In this new rotor-stator configuration, the aerodynamic results predicted by the two codes were in good agreement with the measurements, but the single-blade passage computational domain used in the *Turb'Flow* simulation led to very large structures upstream of the rotor which were not visible in the *PowerFLOW* simulation. An investigation of the acoustic sources showed that the stator potential effect created the dominant noise radiated by the fan. In the far field, the broadband noise prediction from the LBM code was in excellent agreement with the experiment and, more importantly for the scope of this thesis, the acoustic radiation at the BPF was also very well predicted with a maximum difference of 2 dB on the SPL in different directions. However, *Turb'Flow* significantly underpredicted the radiated noise, showing the limitation of a single-blade-passage computational domain for this particular setup. Overall, simulations and measurements characterized the aeroacoustic mechanism

responsible for the acoustic radiation in this rotor-stator configuration – also called primary noise – and set the baseline to investigate the tonal noise reduction method using flow obstruction.

In Chapter 6, a numerical methodology to design the flow obstruction was first proposed. Based on a minimal number of simulations, this methodology aims at obtaining an optimal shape and position of the obstruction for a given fan configuration. To succeed, the first step consists in characterizing the primary noise radiated by the fan. Based on these results, the number of obstruction lobes is chosen to act on the dominant radiation. The first three simulations with a flow obstruction evaluate the optimal magnitude of the secondary noise radiated by the obstruction (controlled by the lobe amplitude or the distance to the fan depending on the configuration). This is achieved by rotating the obstruction in front of the fan, which separates the primary and secondary noise in the frequency spectrum. In a third step, a fourth simulation is performed with the optimal lobe amplitude to determine the optimal angular position. At this stage, even if the obstruction speed is slow enough to assume a quasi-static flow at each angular position, the rotation creates an angle between the obstruction wake and the fan axis. To compensate for this deviation, a correction angle was proposed. The fourth step of the methodology consists in a last simulation with a static obstruction to validate the estimated sound reduction with the optimal design. Overall, the complete characterization of the fan noise and the development of an optimal obstruction is achieved with a maximum of six simulations.

To validate this methodology and further investigate the obstruction-fan interaction, the optimization process was applied to the canonical rotor-stator configuration introduced in Chapter 5. Complete aeroacoustic simulations were performed with *Turb'Flow* and *PowerFLOW* to better understand the effect of the obstruction on the aerodynamic field which leads to the creation of the secondary acoustic sources. Both codes predicted the same flow topology around the obstruction. Vortex rings are created at the base of the lobes and convected downstream to the fan blades. This mechanism generates an azimuthal fluctuation of the velocity in the fan plane. Similarly to a stator-rotor interaction, the periodic wall-pressure fluctuations form the secondary source of tonal noise which controls the noise radiated by the fan. A study of the source locations confirmed this statement. Since the rotating obstruction generates sources at a different frequency than the BPF, the analysis of wall-pressure fluctuations at the corresponding frequency confirmed the location of the sources. Furthermore, the acoustic sources located on the obstruction appeared to be negligible with respect of the sources located on the fan, even in a configuration where the obstruction-fan distance was very small – less than a rotor chord.

Given the large computational cost needed to perform a full simulation with *Turb'Flow*, the design methodology was applied and validated using *PowerFLOW*. Two simulations with rotating obstructions sufficed to predict the optimal lobe amplitude – the second chosen amplitude was serendipitously found to be optimal. Using the optimal lobe amplitude, four additional simulations characterized the influence of the obstruction rotational speed on the optimal angle prediction. Consistent results were found for the two lowest speeds (30 and 60 rpm), but, despite the correction angle introduced in the methodology, results at 120 and 300 rpm differed. At these speeds, large discrepancies were observed between the probe locations, which suggests that the obstruction wake deviation is large enough to influence the secondary acoustic sources. Additionally, the assumption of a quasi-steady state may not be verified at these speeds. Finally, several simulations at different angular positions confirmed the optimal angular position of the obstruction with only a 1° difference. Moreover, the noise reductions predicted with a static and rotating obstruction were in excellent agreement (approximately 20 dB on the sound pressure level for this canonical case).

To validate the numerical design, a complete experimental study was carried out in a fully-anechoic chamber. Using the same setup presented in Chapter 5, the obstruction was held by aluminum rods and driven by a step motor. First, flow-rate and wall-pressure measurements inside the duct characterized the fan aerodynamic performance and the loss induced by the obstruction. Second, sound pressure measurements at eight locations provided the necessary information to estimate the optimal lobe amplitude. Five obstruction lobe amplitudes were tested and results were found in excellent agreement with the simulations. The optimal lobe amplitude was perfectly predicted (20 mm), which confirmed that the simulations were able to capture the aeroacoustic phenomena responsible for the secondary acoustic source. As for the estimation of the optimal angular prediction, five obstruction speeds were tested (between 60 and 140 rpm). Although the predicted optimal angle at each microphone was the same for all the speeds, the microphones in the rotor plane showed some discrepancies which increased with the obstruction speed – a 1° difference at 60 rpm and up to a 5° difference at 140 rpm. These discrepancies were also observed in the *PowerFLOW* results, which supports the assumption that the obstruction wake has a significant impact on the secondary acoustic sources. With the lowest obstruction speed, the optimal angular position was found in good agreement with the numerical prediction – 14° in the experiment and 16° in the simulation. However, the measurements with a static obstruction at different angular position led to an optimal angle of 20°. Two uncertainties can explain this small discrepancy:

1. the visual alignment of the obstruction to match the reference angle $\phi = 0°$ (estimated to 5°);
2. the pulse detection of the tachometer output (estimated to 6°).

Overall, the numerical and experimental results obtained in this study were in excellent agreement. The simulations allowed a better understanding of the aeroacoustic mechanisms responsible for the noise reduction, and an industrially-applicable methodology was developed and validated in order to obtain an optimal obstruction design prior to any measurement.

Perspectives

The extensive numerical work presented in this thesis shed some light on the tonal noise reduction method using a flow obstruction and validated a numerical methodology to obtain an optimal obstruction design and position for a given fan configuration. Despite the results obtained, several points are worth being the center of attention in future investigations:

1. It was demonstrated that the magnitude of the secondary acoustic source (in dB) varies linearly with the obstruction lobe amplitude. Therefore, knowing the slope of this function for a given configuration will allow the prediction of the optimal lobe amplitude from a single simulation – instead of three in the proposed methodology.
2. The obstruction speed appears to have a significant influence on the noise directivity and the optimal angular position. A better understanding of the obstruction-fan interaction at high obstruction speed will certainly be beneficial to asses the maximum speed which agrees with results obtained in a static configuration.
3. Test results highlighted the importance of the obstruction reference angle ($\phi = 0°$) and its impact on the optimal angular position predicted from the measurements. For this reason, it is strongly recommended to use a rotary encoder on the obstruction axis for any experimental work involving rotating obstructions.

Additionally, it should be emphasized that the studied configuration was closer to a canonical case than a real industrial fan. The primary acoustic radiation was dominated by the interaction between the stator and the rotor, which led to very coherent sources and a tonal content concentrated at the BPF. In a real configuration, the acoustic signature may exhibit additional harmonics. Consequently, the noise reduction method may benefit from combining different obstruction profiles to obtain a significant noise reduction (e.g., a nine-lobe profile to target the BPF and an 18-lobe profile to target its first harmonic).

The proposed methodology could thus be developed to design obstructions with a more complex geometry.

To further reduce the computational cost of the obstruction, the numerical study could be divided into two simulations. Assuming that the fan has no significant effect on the aerodynamic mechanisms in the vicinity of the obstruction, a simulation with the obstruction alone could first aim at predicting the transient, periodic velocity profile at the fan inlet. At this stage, a further investigation of the impact of the obstruction geometry on the velocity profile could help identify the influence of each parameter (lobe amplitude, base thickness, obstruction profile) and correlate the results with the Gaussian approximation used by Gérard *et al.* [2009b]. Second, the computed velocity profile could be injected into a simulation with the fan alone to predict the impact on the noise reduction. Furthermore, a good knowledge of the obstruction wake could help develop analytical models to predict the influence of a particular design on the acoustic radiation, which may greatly reduce the computational cost of the methodology.

Finally, the present study focused on the noise reduction of an axial fan. Although flow obstructions have already been used to reduce tonal noise radiated by centrifugal fans [Magne *et al.*, 2013; Oddo *et al.*, 2013], it should be noted that the aeroacoustic mechanisms responsible for the tonal noise are notably different in this configuration (interaction between the rotor blades and the volute tongue). For this reason, it would be interesting to carry out a validation of the proposed numerical methodology on a centrifugal fan and assess the performance of the predicted design.

APPENDIX A
COMPACT ROTATING DIPOLE ANALOGY

THIS appendix presents the derivation of the compact rotating dipole analogy presented in Section 3.4.4.

A.1 Time Domain

Lowson's formulation of the noise radiated by a point fluctuating force F_i in arbitrary motion is given by [Lowson, 1970]:

$$p'(\boldsymbol{x},t) = \left[\frac{(x_i - y_i)}{(1-M_t)c_0 R'}\frac{\partial}{\partial t}\left(\frac{F_i}{4\pi R'(1-M_t)}\right)\right], \tag{A.1}$$

where $p'(\boldsymbol{x},t)$ is the acoustic pressure fluctuation at the observer position $\boldsymbol{x}$ and the time t, $\boldsymbol{y}$ the source location, c_0 the speed of sound, R' is the source-observer distance, $M_t = \Omega\, R_0\, c_0^{-1}$ the tangential Mach number at the radius R_0 (see sketch in Figure A.1). Bold characters symbolize vectors, and brackets denote the evaluation at the retarded time t_e which verifies the equation:

$$t_e - t + \frac{R'}{c_0} = 0 \tag{A.2}$$

where

$$R' = |\boldsymbol{x} - \boldsymbol{y}(t_e)| = |\boldsymbol{R} - \boldsymbol{R_0}(t_e)| = \sqrt{(\boldsymbol{R} - \boldsymbol{R_0}(t_e))^2} \tag{A.3}$$

Given the coordinates of $\boldsymbol{R}$ and $\boldsymbol{R_0}(t_e)$

$$\boldsymbol{R} = \left|\begin{array}{l} R\sin\theta\,\cos\varphi \\ R\sin\theta\,\sin\varphi \\ R\cos\theta \end{array}\right. \qquad \boldsymbol{R_0}(t_e) = \left|\begin{array}{l} R_0\,\cos(\Omega t_e) \\ R_0\,\sin(\Omega t_e) \\ 0 \end{array}\right. , \tag{A.4}$$

we obtain:

$$|\boldsymbol{x} - \boldsymbol{y}(t_e)| = \left(R^2 - 2\boldsymbol{R}\boldsymbol{R_0} + R_0^2\right)^{1/2} \tag{A.5}$$

$$= R\left(1 - 2\sin\theta\cos\varphi\frac{R_0}{R}\cos(\Omega t_e) + \sin\theta\sin\varphi\frac{R_0}{R}\sin(\Omega t_e) + \left(\frac{R_0}{R}\right)^2\right)^{1/2} \tag{A.6}$$

$$= R\left(1 - 2\sin\theta\frac{R_0}{R}\cos(\Omega t_e - \varphi) + \left(\frac{R_0}{R}\right)^2\right)^{1/2} \tag{A.7}$$

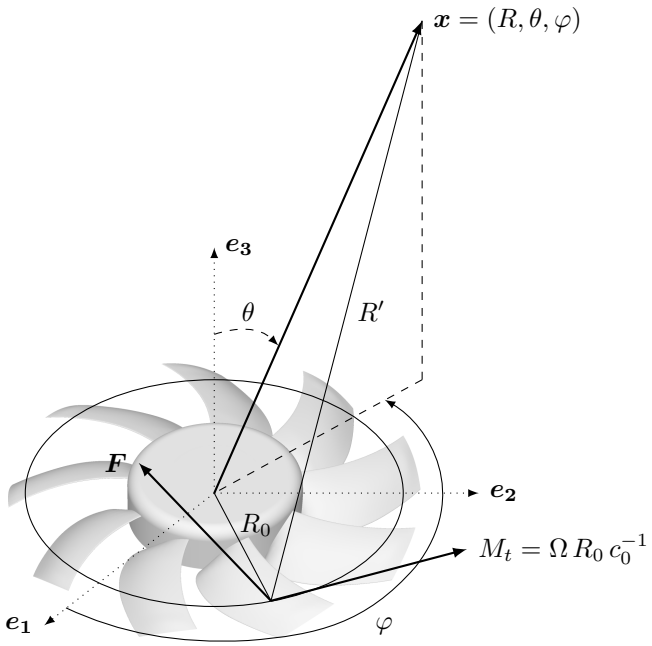

Figure A.1 Sketch of the compact rotating dipole analogy.

Consequently, the resolution is difficult at the retarded time, but necessary to study time based mechanisms, such as the *beating* noise of a helicopter rotor. For any other purpose, the formulation transformed in the frequency domain appears more convenient.

A.2 Frequency Domain

The Fourier transform $\tilde{F}(\omega)$ of a signal $F(t)$ and its inverse are obtained with the following relations:

$$\tilde{F}(\omega) = \frac{1}{2\pi}\int_{-\infty}^{+\infty} F(t)e^{i\omega t}dt \qquad\qquad F(t) = \int_{-\infty}^{+\infty} \tilde{F}(\omega)e^{-i\omega t}d\omega \tag{A.8}$$

The acoustic pressure in the frequency domain is therefore written:

$$\tilde{p}(\boldsymbol{x},\omega) = \frac{1}{2\pi}\int_{-\infty}^{+\infty} -\frac{1}{4\pi}\left[\frac{R'_i}{R'^2 c_0(1-M_r)}\cdot\frac{\partial}{\partial t'}\left(\frac{F_i}{1-M_r}\right)\right]_{t'=t_e} e^{i\omega t}dt, \tag{A.9}$$

where $R'_i = (x_i - y_i)$ and $R' = |\boldsymbol{x} - \boldsymbol{y}|$. Using the variable changes $\tau = t_e$ and $\Delta = 1 - M_r$, we obtain:

$$\tau = t + \frac{R'(\tau)}{c_0} = 0 \qquad dt = d\tau\left(1 - \frac{V'(\tau)}{c_0}\right) = d\tau(1-M_r) = \Delta d\tau \tag{A.10}$$

Thus, we can write:

$$\tilde{p}(\boldsymbol{x},\omega) = \frac{1}{2\pi c_0}\int_{-\infty}^{+\infty} -\frac{1}{4\pi}\left[\frac{R_i'}{R'^2\Delta}\cdot\frac{\partial}{\partial\tau}\left(\frac{F_i}{\Delta}\right)\right]_\tau e^{i\omega(\tau-R'(\tau)/c_0)}\Delta d\tau \tag{A.11}$$

And, using an integration by parts:

$$\tilde{p}(\boldsymbol{x},\omega) = -\frac{1}{8\pi^2 c_0}\left\{\underbrace{\left[\frac{R_i'}{R'^2}e^{i\omega(\tau-R'(\tau)/c_0)}\frac{F_i}{\Delta}\right]_{-\infty}^{+\infty}}_{\text{tends towards 0 at the infinity}} - \int_{-\infty}^{+\infty}\frac{\partial}{\partial\tau}\left(\frac{R_i'}{R'^2}e^{i\omega(\tau-R'(\tau)/c_0)}\right)\frac{F_i}{\Delta}d\tau\right\} \tag{A.12}$$

$$= \frac{1}{8\pi^2 c_0}\int_{-\infty}^{+\infty}\left[\underbrace{\frac{\partial}{\partial\tau}\left(\frac{R_i'}{R'^2}\right)e^{i\omega(\tau-R'(\tau)/c_0)}}_{\text{negligible in the far field}} + \frac{R_i'}{R'^2}\frac{\partial}{\partial\tau}\left(e^{i\omega(\tau-R'(\tau)/c_0)}\right)\right]\frac{F_i}{\Delta}d\tau \tag{A.13}$$

$$= \frac{1}{8\pi^2 c_0}\int_{-\infty}^{+\infty}\frac{F_i R_i'}{R'^2\Delta}i\omega\Delta e^{i\omega(\tau-R'(\tau)/c_0)}d\tau \tag{A.14}$$

$$= \frac{i\omega}{8\pi^2 c_0}\int_{-\infty}^{+\infty}\frac{F_i R_i'}{R'^2}e^{i\omega(\tau-R'(\tau)/c_0)}d\tau \tag{A.15}$$

In cylindrical and Cartesian coordinates, the force is respectively:

$$\boldsymbol{F} = \left|\begin{array}{ll} F_R & \text{(Radial)} \\ F_T & \text{(Tangential)} \\ F_A & \text{(Axial)} \end{array}\right. \qquad \boldsymbol{F} = \left|\begin{array}{l} F_R\cos(\Omega t_e) - F_T\sin(\Omega t_e) \\ F_R\sin(\Omega t_e) - F_T\cos(\Omega t_e) \\ F_A \end{array}\right. \tag{A.16}$$

Therefore, we can write:

$$F_i R_i = \boldsymbol{F}\cdot\boldsymbol{R}' = \boldsymbol{F}\cdot(\boldsymbol{R}-\boldsymbol{R}_0) = [F_R\cos(\Omega\tau) - F_T\sin(\Omega\tau)] - \underbrace{F_R R_0}_{\text{negligible }(R_0\ll R)} + F_A R\cos\theta \tag{A.17}$$

Moreover, we have:

$$R'^2 = R^2 - 2RR_0\sin\theta\cos(\Omega\tau-\varphi) + R_0^2 \approx R^2 \tag{A.18}$$

$$R' \approx R - R_0\sin\theta\cos(\Omega\tau-\varphi) \tag{A.19}$$

We thus obtain:

$$\tilde{p}(\boldsymbol{x},\omega) = \frac{1}{8\pi^2 c_0}\int_{-\infty}^{+\infty} R\left[\frac{\sin\theta\Big(F_R\cos(\Omega\tau-\varphi) - F_T\sin(\Omega\tau-\varphi)\Big) + F_A\cos\theta}{R^2}\right] \times e^{i\omega\left[\tau-\frac{1}{c_0}\left(R-R_0\sin\theta\cos(\Omega\tau-\varphi)\right)\right]}d\tau \tag{A.20}$$

$$\tilde{p}(\boldsymbol{x},\omega) = \frac{i\omega e^{i\omega R/c_0}}{8\pi^2 c_0 R}\int_{-\infty}^{+\infty}\int_{-\infty}^{+\infty} e^{i\left[(\omega-\omega')\tau - \frac{\omega R_0}{c_0}\sin\theta\cos(\Omega\tau-\varphi)\right]} \times \left[\tilde{F}_R(\omega')\sin\theta\cos(\Omega\tau-\varphi) - \tilde{F}_T(\omega')\sin\theta\sin(\Omega\tau-\varphi) + \tilde{F}_A(\omega')\cos\theta\right] d\omega' d\tau \tag{A.21}$$

Using the definition

$$e^{-ia\cos X} = \sum_{n=-\infty}^{+\infty}(-i)^n J_n(a) e^{-inX}, \tag{A.22}$$

the expression becomes:

$$\tilde{p}(\boldsymbol{x},\omega) = \frac{i\omega e^{i\omega R/c_0}}{8\pi^2 c_0 R}\int_{-\infty}^{+\infty}\left[\tilde{F}_R(\omega')\sin\theta\cdot I_1 - \tilde{F}_T(\omega')\sin\theta\cdot I_2 + \tilde{F}_A(\omega')\cos\theta\cdot I_3\right] d\omega', \tag{A.23}$$

where

$$I_3 = \int_{-\infty}^{+\infty} e^{i\left[(\omega-\omega')\tau - \frac{\omega R_0}{c_0}\sin\theta\cos(\Omega\tau-\varphi)\right]} d\tau \tag{A.24}$$

$$= \frac{2\pi}{\Omega} e^{-i\varphi\frac{\omega'-\omega}{\Omega}} \sum_{n=-\infty}^{+\infty}(-i)^n J_n\left(\frac{\omega R_0\sin\theta}{c_0}\right)\delta\Big(n+\tfrac{\omega'-\omega}{\Omega}\Big) \tag{A.25}$$

$$I_1 = \int_{-\infty}^{+\infty} e^{i\left[(\omega-\omega')\tau - \frac{\omega R_0}{c_0}\sin\theta\cos(\Omega\tau-\varphi)\right]}\cos(\Omega\tau-\varphi) d\tau \tag{A.26}$$

$$= \frac{2\pi}{\Omega} e^{-i\varphi\frac{\omega'-\omega}{\Omega}} \sum_{n=-\infty}^{+\infty}(-i)^n J_n'\left(\frac{\omega R_0\sin\theta}{c_0}\right)\delta\Big(n+\tfrac{\omega'-\omega}{\Omega}\Big) \tag{A.27}$$

$$I_2 = \int_{-\infty}^{+\infty} e^{i\left[(\omega-\omega')\tau - \frac{\omega R_0}{c_0}\sin\theta\cos(\Omega\tau-\varphi)\right]}\sin(\Omega\tau-\varphi) d\tau \tag{A.28}$$

$$= -\frac{2\pi}{\Omega} e^{-i\varphi\frac{\omega'-\omega}{\Omega}} \sum_{n=-\infty}^{+\infty}(-i)^n \frac{nc_0}{\omega R_0\sin\theta} J_n\left(\frac{\omega R_0\sin\theta}{c_0}\right)\delta\Big(n+\tfrac{\omega'-\omega}{\Omega}\Big) \tag{A.29}$$

Moreover,

$$\delta\Big(n+\tfrac{\omega'-\omega}{\Omega}\Big) = \Omega\,\delta\Big(\omega'-(\omega-n\Omega)\Big), \tag{A.30}$$

and, for $\omega' = \omega - n\Omega$,

$$\int_{-\infty}^{+\infty}\tilde{F}(\omega')e^{-i\varphi\frac{\omega'-\omega}{\Omega}}\delta\Big(\omega'-(\omega-n\Omega)\Big)d\omega' = \tilde{F}(\omega-n\Omega)e^{in\varphi}. \tag{A.31}$$

Therefore,

$$\begin{aligned}\tilde{p}(\boldsymbol{x},\omega) =&\frac{i\omega e^{i\omega R/c_0}}{4\pi c_0 R}\sum_{n=-\infty}^{+\infty}(-i)^n e^{in\varphi}\Bigg[\tilde{F}_R(\omega-n\Omega)\sin\theta J_n'\left(\frac{\omega R_0\sin\theta}{c_0}\right)\\&+\left(\tilde{F}_A(\omega-n\Omega)\cos\theta-\tilde{F}_T(\omega-n\Omega)\frac{nc_0}{\omega R_0}\right)J_n\left(\frac{\omega R_0\sin\theta}{c_0}\right)\Bigg].\end{aligned}\tag{A.32}$$

Besides,

$$\tilde{F}(\omega)=\frac{1}{2\pi}\int_{-\infty}^{+\infty}\sum_{s=-\infty}^{+\infty}F_s e^{is\Omega t}e^{i\omega t}dt \tag{A.33}$$

$$=\sum_{s=-\infty}^{+\infty}F_s\left(\frac{1}{2\pi}\int_{-\infty}^{+\infty}e^{i(\omega-s\Omega)t}dt\right) \tag{A.34}$$

$$=\sum_{s=-\infty}^{+\infty}F_s\,\delta(\omega-s\Omega) \tag{A.35}$$

and

$$(-i)^n=\left(e^{-i\pi/2}\right)^n=e^{-in\pi/2} \tag{A.36}$$

Consequently,

$$\begin{aligned}\tilde{p}(\boldsymbol{x},\omega) =&\frac{i\omega e^{i\omega R/c_0}}{4\pi c_0 R}\sum_{n=-\infty}^{+\infty}e^{in\left(\varphi-\frac{\pi}{2}\right)}\sum_{s=-\infty}^{+\infty}\Bigg[\tilde{F}_{R_s}\sin\theta J_n'\left(\frac{\omega R_0\sin\theta}{c_0}\right)\\&+\left(\tilde{F}_{A_s}\cos\theta-\tilde{F}_{T_s}\frac{nc_0}{\omega R_0}\right)J_n\left(\frac{\omega R_0\sin\theta}{c_0}\right)\Bigg]\delta\big(\omega-(s+n)\Omega\big).\end{aligned}\tag{A.37}$$

With $N=n+s$:

$$\begin{aligned}\tilde{p}(\boldsymbol{x},\omega)=&\sum_{N=-\infty}^{+\infty}\sum_{s=-\infty}^{+\infty}\frac{i\omega e^{i\omega R/c_0}}{4\pi c_0 R}e^{i(N-s)\left(\varphi-\frac{\pi}{2}\right)}\Bigg[\tilde{F}_{R_s}\sin\theta J_{N-s}'(NM_t\sin\theta)\\&+\left(\tilde{F}_{A_s}\cos\theta-\tilde{F}_{T_s}\frac{N-s}{NM_t}\right)J_{N-s}(NM_t\sin\theta)\Bigg]\delta(\omega-N\Omega)\end{aligned}\tag{A.38}$$

$$=\sum_{N=-\infty}^{+\infty}p_N(\boldsymbol{x})\delta(\omega-N\Omega) \tag{A.39}$$

$$\begin{aligned}\text{with}\quad p_N(\boldsymbol{x})=&\frac{iN\Omega e^{iN\Omega R/c_0}}{4\pi c_0 R}\sum_{s=-\infty}^{+\infty}e^{i(N-s)\left(\varphi-\frac{\pi}{2}\right)}\Bigg[\tilde{F}_{R_s}\sin\theta J_{N-s}'(NM_t\sin\theta)\\&+\left(\tilde{F}_{A_s}\cos\theta-\tilde{F}_{T_s}\frac{N-s}{NM_t}\right)J_{N-s}(NM_t\sin\theta)\Bigg]\end{aligned}\tag{A.40}$$

All the previous development is true for a single blade. For a B-blade rotor, the acoustic pressure can be written

$$p_{\text{rotor}} = \sum_{j=1}^{B} p_j(\boldsymbol{x}, t) \tag{A.41}$$

$$= \sum_{j=1}^{B} p(\boldsymbol{x}, t + \tfrac{\alpha_j}{\Omega}), \tag{A.42}$$

where α_j is the angle between the blade j and $j+1$. In the frequency domain, the expression is:

$$\tilde{p}_{\text{rotor}} = \sum_{j=1}^{B} \frac{1}{2\pi} \int_{-\infty}^{+\infty} p(\boldsymbol{x}, t + \tfrac{\alpha_j}{\Omega}) e^{i\omega t} dt \tag{A.43}$$

Considering the variable changes $t' = t + \frac{\alpha_j}{\Omega}$ and $dt' = dt$, one can obtain:

$$\tilde{p}_{\text{rotor}} = \sum_{j=1}^{B} e^{i\omega \frac{\alpha_j}{\Omega}} \cdot \underbrace{\frac{1}{2\pi} \int_{-\infty}^{+\infty} p(\boldsymbol{x}, t + \tfrac{\alpha_j}{\Omega}) e^{i\omega t'} dt'}_{\tilde{p}(\boldsymbol{x}, \omega)} \tag{A.44}$$

$$= \sum_{N=-\infty}^{+\infty} \tilde{p}_{\text{rotor},N}\, \delta(\omega - N\Omega) \tag{A.45}$$

where

$$\tilde{p}_{\text{rotor},N} = \sum_{j=1}^{B} e^{i\alpha_j N} p_N(\boldsymbol{x}) \tag{A.46}$$

For B blades equally spaced $\alpha_j = j \cdot \frac{2\pi}{B}$, yielding a geometric sequence:

$$\sum_{j=1}^{B} \left(e^{i\frac{2\pi N}{B}} \right)^j \begin{cases} = B & \text{if } N = mB \\ = 0 & \text{if } N \neq mB \end{cases} \tag{A.47}$$

Therefore $N = mB$ and

$$\begin{aligned} \tilde{p}_{\text{rotor},mB}(\boldsymbol{x}) = & \frac{imB^2\Omega e^{imB\Omega R/c_0}}{4\pi c_0 R} \sum_{s=-\infty}^{+\infty} e^{i(mB-s)\left(\varphi - \frac{\pi}{2}\right)} \Bigg[\tilde{F}_{R_s} \sin\theta J'_{mB-s}(mBM_t \sin\theta) \\ & + \left(\tilde{F}_{A_s} \cos\theta - \tilde{F}_{T_s} \tfrac{mB-s}{mBM_t} \right) J_{mB-s}(mBM_t \sin\theta) \Bigg] \end{aligned} \tag{A.48}$$

APPENDIX B
COMPUTATIONAL SERVERS

SPECIFICATIONS of the two cluster used for all the computations are reported in Table B.1. Mammoth Series II was used for *Turb'Flow* computations whereas Mammoth Parallel II was used for *PowerFLOW* simulations.

Table B.1 Computational servers specifications (MS is Mammoth Series II; MP is Mammoth Parallel II).

	MS	MP
Nodes	308	1632
Cores per nodes	8	24
Processors	Intel Xeon E5462	AMD Opteron 6172
Cores per CPU	4	12
CPU frequency	2.8 GHz	2.1 GHz
CPU cache memory	12 Mb	12 Mb
Node memory	16 or 32 Gb	32 Gb
Network	InfiniBand DDR	InfiniBand QDR

LIST OF REFERENCES

Andersson, A. O. (1997). Active control of tone noise in engine ducts. US Patent 5,692,702.

Bedout, J. M. D., Franchek, M. A., Bernhard, R. J. and Mongeau, L. (1997). Adaptative-Passive Noise Control with Self-Tuning Helmholtz Resonators. *Journal of Sound and Vibration*, volume 202, number 1, pp. 109–123.

Bhatnagar, P., Gross, E. and Krook, M. (1954). A Model for Collision Processes in Gases. I. Small Amplitude Processes in Charged and Neutral One-Component Systems. *Physical Review*, volume 94, number 3, pp. 511–525.

Bogey, C., Bailly, C. and Juvé, D. (2002). Computation of flow noise using source terms in linearized Euler's equations. *AIAA Journal*, volume 40, number 2, pp. 235–243.

Bommes, L., Grundmann, R., Klaes, K. and Kramer, C. (1995). Effects of blade design on centrifugal fan noise and performance. *Noise Control Engineering*, volume 43, number 4, pp. 91–101.

Boudet, J. (2003). *Approches numériques pour la simulation du bruit à large bande en vue de l'application aux turbomachines*. Ph.D. thesis, École Centrale de Lyon.

Brentner, K. S. and Farassat, F. (1998). An analytical comparison of the acoustic analogy and Kirchhoff formulation for moving surfaces. *AIAA Journal*, volume 36, number 8, pp. 1379–1386.

Brès, G., Pérot, F. and Freed, D. (2009). Properties of the Lattice-Boltzmann Method for Acoustics. In *15th AIAA/CEAS Aeroacoustics Conference*. Miami, Florida, USA, May 11–13. Paper AIAA-2009-3395.

Buisson, M., Ferrand, P., Soulat, L., Aubert, S., Moreau, S., Rambeau, C. and Henner, M. (2013). Optimal design of an automotive fan using the Turb'Opty meta-model. *Computers & Fluids*, volume 80, pp. 207–213.

Caro, S. and Moreau, S. (2000). Aeroacoustic modelling of low pressure axial flow fans. In *6th AIAA/CEAS Aeroacoustic Conference*. Lahaina, Hawaii, USA, June 12–14. Paper AIAA-2000-2049.

Carolus, T. and Beiler, M. (1997). Skewed blades in low pressure fans - a survey of noise reduction mechanisms. In *3rd AIAA/CEAS Aeroacoustics Conference*. Atlanta, Georgia, USA, May 12–14. Paper AIAA-97-1591.

Carolus, T. H., Schneider, M. and Reese, H. (2007). Axial flow fan broad-band noise and prediction. *Journal of Sound and Vibration*, volume 300, number 1-2, pp. 50–70.

Casalino, D. (2002). *Analytical and Numerical Methods in Vortex-Body Aeroacoustics*. Ph.D. thesis, Politecnico di Torino and École Centrale de Lyon.

Casalino, D. (2003). An advanced time approach for acoustic analogy predictions. *Journal of Sound and Vibration*, volume 261, number 4, pp. 583–612.

Casalino, D. (2009). FoxWHawk (computer software).

Casalino, D., Moreau, S. and Roger, M. (2010). One, no one and one hundred thousand methods for low-speed fan noise prediction. *International Journal of Aeroacoustics*, volume 9, number 3, pp. 307–327.

Cattanei, A., Ghio, R. and Bongiovi, A. (2007). Reduction of the tonal noise annoyance of axial flow fans by means of optimal blade spacing. *Applied Acoustics*, volume 68, number 11-12, pp. 1323–1345.

Chapman, D. R. (1979). Computational Aerodynamics Development and Outlook. *AIAA Journal*, volume 17, number 12, pp. 1293–1313.

Chen, S. and Doolen, G. D. (1998). Lattice Boltzmann Method for Fluid Flows. *Annual Review of Fluid Mechanics*, volume 30, number 1, pp. 329–364.

Choi, H. and Moin, P. (2012). Grid-point requirements for large eddy simulation: Chapman's estimates revisited. *Physics of Fluids*, volume 24, number 1, p. 011702.

Coggiola, E., Dessale, B., Moreau, S. and Broberg, R. (1998). On the Use of CFD in the Automotive Engine Cooling Fan System Design. In *36th Aerospace Sciences Meeting & Exhibit*. Reno, Nevada, January 12–15. Paper AIAA-98-0772.

Colonius, T. and Lele, S. (2004). Computational aeroacoustics: progress on nonlinear problems of sound generation. *Progress in Aerospace Sciences*, volume 40, number 6, pp. 345–416.

Curle, N. (1955). The Influence of Solid Boundaries upon Aerodynamic Sound. *Royal Society of London Proceedings Series A*, volume 231, pp. 505–514.

de Bedout, J. M. (1996). *Adaptative-Passive Noise Control with Self-Tuning Helmholtz Resonators*. Ph.D. thesis, Purdue University.

De Laborderie, J. (2013). *Approches analytiques et numériques pour la prédiction du bruit tonal et large bande de soufflantes de turboréacteurs*. Ph.D. thesis, Université de Sherbrooke.

De Laborderie, J., Soulat, L. and Moreau, S. (2014). Prediction of Noise Sources in Axial Compressor from URANS Simulation. *Journal of Propulsion and Power*, volume 30, number 5, pp. 1257–1271.

DeFauw, R. H. and Murley, R. G. (1974). Automotive fan shroud. US Patent 3,832,085.

Difrancescantonio, P. (1997). A New Boundary Integral Formulation for the Prediction of Sound Radiation. *Journal of Sound and Vibration*, volume 202, number 4, pp. 491–509.

Dixon, S. L. and Hall, C. A. (2010). *Fluid Mechanics and Thermodynamics of Turbomachinery*, sixth edition. Elsevier, Burlington, Massachusetts, USA.

Dobrzynski, W. (1993). Propeller noise reduction by means of unsymmetrical blade-spacing. *Journal of Sound and Vibration*, volume 163, number 1, pp. 123–136.

Duncan, P. and Dawson, B. (1974). Reduction of interaction tones from axial flow fans by suitable design of rotor configuration. *Journal of Sound and Vibration*, volume 33, number 2, pp. 143–154.

European Parliament and Council (2002). Directive 2002/49/EC relating to the assessment and management of environmental noise.

European Union (2008). Practitioner Handbook for Local Noise Action Plans - Recommendations from the SILENCE project. `http://www.silence-ip.org/site/`.

Exa Corporation (2012). PowerFLOW (computer software). Burlington, Massachusetts, USA, `http://www.exa.com/powerflow.html`.

Fares, E. (2006). Unsteady flow simulation of the Ahmed reference body using a lattice Boltzmann approach. *Computers & Fluids*, volume 35, number 8-9, pp. 940–950.

Farrel, K. J. and Gearhart, W. S. (2002). Technique for reducing acoustic radiation in turbomachinery. US Patent 6,375,416 B1.

Ffowcs Williams, J. E. and Hawkings, D. L. (1969). Sound Generation by Turbulence and Surfaces in Arbitrary Motion. *Philosophical Transactions of the Royal Society of London. Series A, Mathematical and Physical Sciences*, volume 264, number 1151, pp. 321–342.

Foss, J. F., Neal, D., Henner, M. and Moreau, S. (2001). Evaluating CFD Models of Axial Fans by Comparisons with Phase-Averaged Experimental Data. In *Vehicle Thermal Management Systems 5*. Nashville, Tennessee, USA, May 14–17. Paper 01VTMS-89.

Fournier, G., Huard, J. and Pérucchini, J. (1994). Noise reduction of fans by control of flow distortion. In *Inter-Noise*. Yokohama, Japan, August 29–31. pp. 519–522.

Frisch, U., Hasslacher, B. and Pomeau, Y. (1986). Lattice-Gas Automata for the Navier-Stokes Equation. *Physical Review Letters*, volume 56, number 14, pp. 1505–1508.

Fukano, T., Takamatsu, Y. and Kodama, Y. (1986). The effects of tip clearance on the noise of low pressure axial and mixed flow fans. *Journal of Sound and Vibration*, volume 105, number 2, pp. 291–308.

Gérard, A. (2006). *Bruit de raie des ventilateurs axiaux : Estimation des sources aéroacoustiques par modèles inverses et méthodes de contrôle*. Ph.D. thesis, École Supérieure d'Ingénieurs de Poitiers.

Gérard, A., Berry, A. and Masson, P. (2005a). Control of tonal noise from subsonic axial fan. Part 1: reconstruction of aeroacoustic sources from far-field sound pressure. *Journal of Sound and Vibration*, volume 288, number 4-5, pp. 1049–1075.

Gérard, A., Berry, A. and Masson, P. (2005b). Control of tonal noise from subsonic axial fan. Part 2: active control simulations and experiments in free field. *Journal of Sound and Vibration*, volume 288, number 4-5, pp. 1077–1104.

Gérard, A., Berry, A., Masson, P. and Gervais, Y. (2008). Method and apparatus for controlling tonal noise from subsonic axial fans. European Patent 1,995,470 A2.

Gérard, A., Berry, A., Masson, P. and Gervais, Y. (2009a). Experimental validation of tonal noise control from subsonic axial fans using flow control obstructions. *Journal of Sound and Vibration*, volume 321, number 1-2, pp. 8–25.

Gérard, A., Berry, A., Masson, P. and Gervais, Y. (2009b). Modelling of tonal noise control from subsonic axial fans using flow control obstructions. *Journal of Sound and Vibration*, volume 321, number 1-2, pp. 26–44.

Gérard, A., Berry, A., Masson, P. and Moreau, S. (2013). Use of a beat effect for the automatic positioning of flow obstructions to control tonal fan noise: Theory and experiments. *Journal of Sound and Vibration*, volume 332, number 19, pp. 4450–4460.

Gérard, A. and Besombes, M. (2008). Psychoacoustic impact of tonal noise control from fans. In SIA, *Automotive & Railroad Comfort Congress*. Le Mans, France, November 19–20.

Goldstein, M. (1976). *Aeroacoustics*. McGraw-Hill Inc., New York.

Gorny, L. and Koopmann, G. H. (2009). Axial fan blade tone cancellation using optimally tuned quarter wavelength resonators. *Journal of Vibration and Acoustics*, volume 131, number 2, p. 021002.

Goth, Y., Besombes, M., Chassaignon, C. and Gérard, A. (2012). Fan Tonal Noise Reduction Using Calibrated Obstructions in the Flow: An Experimental Approach. In *Fan Noise*. Senlis, France, April 18–20.

Guo, Z., Zheng, C. and Shi, B. (2002). Discrete lattice effects on the forcing term in the lattice Boltzmann method. *Physical Review E*, volume 65, number 4, p. 046308.

Henderson, R. D. (1995). Details of the drag curve near the onset of vortex shedding. *Physics of Fluids*, volume 7, number 9, pp. 2102–2104.

Henner, M., Moreau, S., Stanciu, M., Aubert, S. and Ferrand, P. (2000). Unsteady Rotor-Stator Interactions in Automotive Engine Cooling Fan Systems. In *9th ISUAAAT Symposium*. Lyon, France, September 4–8.

Hersh, A. S., Walker, B. E. and Heidelberg, L. (2001). Active control source cancellation and active control Helmholtz resonator absorption of axial fan rotor-stator interaction noise. US Patent 6,201,872 B1.

Hong, T. and Savage, J. R. (2009). Cooling fan using Coandă effect to reduce recirculation. US Patent 7,478,993.

Huang, L. (2003). Characterizing Computer Cooling Fan Noise. *Journal of the Acoustical Society of America*, volume 114, number 6, pp. 3189–3200.

Huang, L. and Wang, J. (2005). Acoustic analysis of a computer cooling fan. *Journal of the Acoustical Society of America*, volume 118, number 4, pp. 2190–2200.

Inoue, O. and Hatakeyama, N. (2002). Sound generation by a two-dimensional circular cylinder in a uniform flow. *Journal of Fluid Mechanics*, volume 471, pp. 285–314.

Jameson, A., Schmidt, W. and Turkel, E. (1981). Numerical solution of the Euler equations by finite volume methods using Runge Kutta time stepping schemes. In *14th AIAA Fluid and Plasma Dynamics Conference*. Palo Alto, California, USA, June 23–25. Paper AIAA-1981-1259.

Kármán, T. V. (2013). On the mechanism of the drag a moving body experiences in a fluid. *Progress in Aerospace Sciences*, volume 59, pp. 13–19.

Kok, J. C. (2000). Resolving the Dependence on Freestream Values for the k-omega Turbulence Model. *AIAA Journal*, volume 38, number 7, pp. 1292–1295.

Koopmann, G. H. and Neise, W. (1982). The use of resonators to silence centrifugal blowers. *Journal of Sound and Vibration*, volume 82, number 1, pp. 17–27.

Kota, V. and Wright, M. C. M. (2006). Wake generator control of inlet flow to cancel flow distortion noise. *Journal of Sound and Vibration*, volume 295, number 1-2, pp. 94–113.

Kousen, K. A. and Verdon, J. M. (1994). Active control of wake/blade-row interaction noise. *AIAA Journal*, volume 32, number 10, pp. 1953–1960.

Lafitte, A. and Pérot, F. (2009). Inverstigation of the Noise Generated by Cylinder Flows Using a Direct Lattice-Boltzmann Approach. In *15th AIAA/CEAS Aeroacoustics Conference*. Miami, Florida, USA, May 11–13. Paper AIAA-2009-3268.

Lauchle, G. C., MacGillivray, J. R. and Swanson, D. C. (1997). Active control of axial-flow fan noise. *Journal of the Acoustical Society of America*, volume 101, number 1, pp. 341–349.

Lee, J., Cho, K. and Lee, S. (2000). Application of Acoustic Analogy to Automotive Engine-Cooling Fan Noise Prediction. *AIAA Journal*, volume 38, number 6, pp. 1095–1098.

Lew, P.-T., Lyrintzis, A., Crouse, B., Balasubramanian, G., Freed, D. and Mongeau, L. (2007). Noise prediction of a subsonic turbulent round jet using the lattice-Boltzmann method. In *13th AIAA/CEAS Aeroacoustics Conference*. Roma, Italy, May 21–23. Paper AIAA-2007-3636.

Lighthill, M. J. (1952). On Sound Generated Aerodynamically. I. General Theory. *Royal Society of London Proceedings Series A*, volume 211, pp. 564–587.

Liou, M.-S. (1996). A Sequel to AUSM: AUSM+. *Journal of Computational Physics*, volume 129, number 2, pp. 364–382.

Liu, Q., Qi, D. and Tang, H. (2007). Computation of aerodynamic noise of centrifugal fan using large eddy simulation approach, acoustic analogy, and vortex sound theory. *Proceedings of the Institution of Mechanical Engineers, Part C: Journal of Mechanical Engineering Science*, volume 221, number 11, pp. 1321–1332.

LMFA (2010). Turb'Flow (computer software). Lyon, France, `http://lmfa.ec-lyon.fr/`.

Longhouse, R. (1977). Vortex shedding noise of low tip speed, axial flow fans. *Journal of Sound and Vibration*, volume 53, number 1, pp. 25–46.

Longhouse, R. (1978). Control of tip-vortex noise of axial flow fans by rotating shrouds. *Journal of Sound and Vibration*, volume 58, number 2, pp. 201–214.

Lowson, M. V. (1970). Theoretical Analysis of Compressor Noise. *Journal of the Acoustical Society of America*, volume 47, pp. 370–385.

Lyrintzis, A. (2002). Surface Integral Methods in Computational Aeroacoustics – From the (CFD) Near-Field to the (Acoustic) Far-Field. In *CEAS Workshop "From CFD to CAA"*. Athens, Greece, November.

Magne, S., Moreau, S. and Berry, A. (2015). Subharmonic tonal noise from backflow vortices radiated by a low-speed ring fan in uniform inlet flow. *Journal of the Acoustical Society of America*, volume 137, pp. 228–237.

Magne, S., Sanjosé, M., Moreau, S. and Berry, A. (2014). *INNOV Project: Tonal Noise Control with Flow Obstruction* (Technical report).

Magne, S., Sanjosé, M., Moreau, S., Berry, A. and Gérard, A. (2013). Tonal Noise Control of Centrifugal Fan Using Flow Obstructions - Experimental and Numerical Approaches. In *19th AIAA/CEAS Aeroacoustics Conference*. Berlin, Germany, May 27–29. Paper AIAA-2013-2043.

Maier, R., Zillmann, J., Roure, A., Winninger, M., Enghardt, L., Tapken, U., Neise, W., Antoine, H. and Bouty, E. (2001). Active control of fan tone noise from aircraft engines. In *7th AIAA/CEAS Aeroacoustics Conference*. Maastricht, Netherlands, May 28–30. Paper A01-30863.

Maldonado, A. L. P., Miserda, R. F. B. and Pimenta, B. G. (2012). Computational Tonal Noise Prediction for the Advanced Noise Control Fan. In *18th AIAA/CEAS Aeroacoustics Conference*. Colorado Springs, Colorado, USA, June 4–6. Paper AIAA-2012-2128.

Marchesse, Y. (2008). *Modélisation de la turbulence - Application à la CFD*. Lecture notes, ECAM Lyon, France.

Marsden, O. (2005). *Calcul direct du rayonnement acoustique de profils par une approche curviligne d'ordre élevé*. Ph.D. thesis, École Centrale de Lyon.

Mellin, R. C. and Sovran, G. (1970). Controlling the tonal characteristics of the aerodynamic noise generated by fan rotors. *Journal of Basic Engineering*, volume 92, number 1, pp. 143–154.

Moreau, S. and Bakir, F. (2003). Detailed Study of an Efficient Small Diameter Automotive Cooling Fan System. In *ASME Fluids Engineering Division Summer Meeting*. Honolulu, Hawaii, USA, July 6–10. Paper FEDSM2003-45117.

Moreau, S. and Bakir, F. (2004). Aeroacoustic Characteristics of Efficient Automotive Engine Cooling Fan Systems. In *ASME Heat Transfer/Fluid Engineering Summer Conference*. Charlotte, North Carolina, USA, July 11–15. Paper HT-FED2004-56824.

Moreau, S. and Bennett, E. (1997). Improved Fan Design using CFD. In *SAE International Congress & Exposition*. Detroit, Michigan, USA, March. Paper SAE 970934.

Moreau, S. and Casalino, D. (2005). Aeroacoustic Design of Automotive Engine Cooling Fan Systems. In *11th AIAA/CEAS Aeroacoustics Conference*. Monterey, California, USA, May 23–25. Paper AIAA-2005-2906.

Moreau, S., Henner, M., Casalino, D., Gullbrand, J., Iaccarino, G. and Wang, M. (2006a). Toward the Prediction of Low-Speed Fan Noise. In *Center for Turbulence Research, Proceedings of the Summer Program*. pp. 519–531.

Moreau, S., Henner, M., Levasseur, A. and Demory, B. (2006b). Fan Comprising an Outer Rib Axially Positioned with Regard to the Peripheral Annular Skirt. International Patent WO 2006/063830 A2.

Moreau, S., Levasseur, A. and Demory, B. (2006c). Ventilating System Comprising Means for Limiting Backflow. International Patent WO 2006/063825 A1.

Moreau, S. and Roger, M. (2007). Competing Broadband Noise Mechanisms in Low-Speed Axial Fans. *AIAA Journal*, volume 45, number 1, pp. 48–57.

Moreau, S., Sanjosé, M. and Lallier-Daniel, D. (2015). Aeroacoustic analysis of a low-subsonic axial fan. In *ASME Turbo Expo*. Montreal, Canada, June 15–19. Paper GT2015-43737.

Moreau, S., Sanjosé, M., Magne, S. and Henner, M. (2011). Unsteady Turbulent Simulations of Low-Speed Axial Fans. In *46th Symposium of Applied Aerodynamics (3AF)*. Orléans, France, March 28–30.

Moreau, S., Sanjosé, M., Magne, S. and Henner, M. (2012). Aeroacoustic Predictions of a Low-Subsonic Axial Fan. In *13th International Symposium on Transport Phenomena and Dynamics of Rotating Machinery*. Honolulu, Hawaii, USA, February 27 – March 2.

Morfey, C. L. (1971). Tone Radiation from an Isolated Subsonic Rotor. *Journal of the Acoustical Society of America*, volume 49, number 5B, pp. 1690–1692.

Neise, W. (1992). Review of Fan Noise Generation Mechanisms and Control Methods. In *Fan Noise*. pp. 45–56.

Neise, W. and Koopmann, G. H. (1980). Reduction of centrifugal fan noise by use of resonators. *Journal of Sound and Vibration*, volume 73, number 2, pp. 297–308.

Nelson, P. A. (2000). Active Techniques and Their Potential for Application in Aeroacoustics. In *6th AIAA/CEAS Aeroacoustic Conference*. Lahaima, Hawaii, USA, June 12–14. Keynote Lecture AIAA-2000-2100.

Neuhaus, L. and Neise, W. (2002). Active control of the aerodynamic and acoustic performance. In *8th AIAA/CEAS Aeroacoustics Conference*. Breckenridge, Colorado, USA, June 17-19. Paper AIAA-2002-2499.

Neuhaus, L., Schulz, J., Neise, W. and Möser, M. (2003). Active control of the aerodynamic performance and tonal noise of axial turbomachines. *Proceedings of the Institution of Mechanical Engineers, Part A: Journal of Power and Energy*, volume 217, number 4, pp. 375–383.

O'Brien, R., Watkins, J., Piper, G. E. and Baumann, D. (1999). Robust global control of fan noise in an acoustic duct using magnetic bearings. In *38th IEEE Conference on Decision and Control*. Phoenix, Arizona, USA, December 7–10. pp. 2605–2610.

Oddo, R., Gérard, A., Pearson, M., Amyotte, A., Masson, P., Sgard, F. and Berry, A. (2013). Industrial fan noise control using flow obstructions. *Journal of the Acoustical Society of America*, volume 133, number 5, p. 3264.

Park, S.-Y. (2009). Fan and shroud assembly. US Patent 7,481,615 B2.

Pasco, Y., Guedeney, T., Leung-Tack, A., Berry, A. and Moreau, S. (2014a). Active Noise Control Simulation of Tonal Turbofan Noise in Aero Engines. In *20th AIAA/CEAS Aeroacoustics Conference*. Atlanta, Georgia, USA, June 16–20. Paper AIAA-2014-3187.

Pasco, Y., Guedeney, T., Leung-Tack, A., Berry, A., Moreau, S. and Masson, P. (2014b). Active Noise Control of Tonal Turbofan Noise in Aero Engines. In *15th International Symposium on Transport Phenomena and Dynamics of Rotating Machinery*. Honolulu, Hawaii, USA, February 24–28.

Pérot, F. (2004). *Calcul du rayonnement acoustique d'écoulements turbulents basé sur des analogies acoustiques couplées aux simulations aérodynamiques instationnaires*. Ph.D. thesis, École Centrale de Lyon.

Pérot, F., Kim, M.-S., Freed, D., Lee, D. and Ih, K. D. (2010a). Direct aeroacoustics prediction of ducts and vents noise. In *16th AIAA/CEAS Aeroacoustics Conference*. Stockholm, Sweden, June 7–9. Paper AIAA-2010-3724.

Pérot, F., Kim, M.-S., Legoff, V., Carniel, X., Goth, Y. and Chassaignon, C. (2012). Numerical Optimization of the Tonal Noise of a Backward Centrifugal Fan Using Flow Obstruction. In *Fan Noise*. Senlis, France, April 18–20.

Pérot, F., Kim, M.-S., Moreau, S., Henner, M. and Neal, D. (2010b). Direct Aeroacoustics Prediction of a Low Speed Axial Fan. In *16th AIAA/CEAS Aeroacoustics Conference*. Stockholm, Sweden, June 7–9. Paper AIAA-2010-3887.

Piper, G. E. (2005). Active Control of Axial-flow Fan Noise Using Magnetic Bearings. *Journal of Vibration and Control*, volume 11, number 9, pp. 1221–1232.

Pointwise (2010). Gridgen (computer software). Fort Worth, Texas, USA, `http://www.pointwise.com/gridgen/`.

Polacsek, C. and Desbois-Lavergne, F. (2003). Fan interaction noise reduction using a wake generator: experiments and computational aeroacoustics. *Journal of Sound and Vibration*, volume 265, number 4, pp. 725–743.

Rao, N. M., Feng, J., Burdisso, R. A. and Ng, W. F. (2001). Experimental Demonstration of Active Flow Control to Reduce Unsteady Stator-Rotor Interaction. *AIAA Journal*, volume 39, number 3, pp. 458–464.

Roger, M., Moreau, S. and Guédel, A. (2006). Broadband fan noise prediction using single-airfoil theory. *Noise Control Engineering Journal*, volume 54, number 1, pp. 5–14.

Sanjosé, M., Moreau, S., Kim, M.-S. and Pérot, F. (2011). Direct self-noise simulation of the installed Controlled Diffusion airfoil. In *17th AIAA/CEAS Aeroacoustics Conference*. Portland, Oregon, USA.

Sears, W. (1941). Some aspects of non-stationary airfoil theory and its practical applications. *Journal of the Aeronautical Sciences*, volume 8, number 3, pp. 104–108.

Soulat, L. (2010). *Définition, analyse et optimisation aérodynamique d'un nouveau concept de traitement de carter au moyen d'outils numériques - Application aux turbomachines basse vitesse*. Ph.D. thesis, École Centrale de Lyon.

Soulat, L., Ferrand, P., Moreau, S., Aubert, S. and Buisson, M. (2013a). Efficient optimisation procedure for design problems in fluid mechanics. *Computers & Fluids*, volume 82, pp. 73–86.

Soulat, L., Kernemp, I., Moreau, S. and Fernando, R. (2013b). Assessment and comparison of tonal noise models for Counter-Rotating Open Rotors. In *19th AIAA/CEAS Aeroacoustics Conference*. Reston, Virginia, USA, May 27–29. Paper AIAA-2013-2201.

Stairs, R. W. and Greeley, D. S. (2002). High-Efficiency, Inflow-Adapted, Axial-Flow Fan. International Patent WO 2002/038962.

Strouhal, V. (1878). Ueber eine besondere Art der Tonerregung. *Annalen der Physik*, volume 241, number 10, pp. 216–251.

Sturm, M. and Carolus, T. H. (2012). Tonal Fan Noise of an Isolated Axial Fan Rotor Due To Inhomogeneous Coherent Structures at the Intake. *Noise Control Engineering Journal*, volume 60, number 6, pp. 699–706.

Sumer, B. M. and Fredsoe, J. (2006). Flow around a cylinder in steady current. In *Hydrodynamics Around Cylindrical Structures*, chapter 1. World Scientific Pub Co Inc., Singapore.

Tannoury, E. (2013). *Contribution à la prévision du bruit tonal des machines tournantes subsoniques : couplage des simulations numériques et des modèles analytiques avec les analogies acoustiques*. Ph.D. thesis, École Nationale Supérieure d'Arts et Métiers.

Walker, B. E., Hersh, A. S., Heidelberg, L., Sutliff, D. L. and Spencer, M. E. (1999). Active resonators for control of multiple spinning modes in an axial flow fan inlet. In *5th AIAA/CEAS Aeroacoustics Conference*. Bellevue, Washington, USA, May 10–12. Paper AIAA-99-1853.

Wang, J. and Huang, L. (2006). Active control of drag noise from a small axial flow fan. *Journal of the Acoustical Society of America*, volume 120, number 1, pp. 192–203.

Wang, J., Huang, L. and Cheng, L. (2005). A study of active tonal noise control for a small axial flow fan. *Journal of the Acoustical Society of America*, volume 117, number 2, pp. 734–743.

Watkins, J., Piper, G. E., O'Brien, R. and Baumann, D. (1999). On the use of magnetic bearings for global control of fan noise. In *American Control Conference*. San Diego, California, USA, June 2–4. pp. 581–585.

Williamson, C. H. K. (1996). Vortex Dynamics in the Cylinder Wake. *Annual Review of Fluid Mechanicsual*, volume 28, pp. 477–539.

Winkler, J. (2011). *Investigation of Trailing-edge Blowing on Airfoils for Turbomachinery Broadband Noise Reduction*. Ph.D. thesis, Universität Siegen.

Wright, T. (1938). *Fluid Machinery*. CRC Press, Boca Raton, Florida, USA.

Zhang, J., Liu, H., Bi, F., Ni, G., Zhang, G., Lin, J. and Yu, H. (2012). Psychoacoustic study on contribution of fan noise to engine noise. *Chinese Journal of Mechanical Engineering*, volume 25, number 4, pp. 809–815.

Zillmann, J. and Tapken, U. (2009). Tonal Noise Radiation from UHBR Fan - Active Control of Radiation Characteristic. In *15th AIAA/CEAS Aeroacoustics Conference*. Miami, Florida, USA, May 11–13. Paper AIAA-2009-3226.